VIBRATIONAL AND MAGNETIC PROPERTIES OF MECHANICALLY ATTRITED Ni_3Fe NANOCRYSTALS

Thesis by

Heather N. Frase

In Partial Fulfillment of the Requirements

for the Degree of

Doctor of Philosophy

California Institute of Technology

Pasadena, California

1998

(Submitted April 9, 1998)

Acknowledgments

The work contained in this thesis involved the help and resources of many individuals.

Foremost, I'd like to thank my advisor, Professor Brent Fultz, for revitalizing my joy of scientific research. I'd also like to thank him for his help with and guidance of my scientific research.

Many of the experiments in this thesis were performed at facilities outside of the California Institute of Technology. I would like to thank the following people for their collaboration and assistance with their equipment. Inelastic neutron scattering and small angle neutron scattering experiments were both done at Oak Ridge National Laboratory with the help of Dr. Lee Robertson and Dr. Steve Spooner, respectively. The M-H magnetization curves were gathered by Dr. Robert Shull at the National Institute of Standards and Technology. The cavity perturbation measurements were done at the Jet Propulsion Laboratory, with the assistance of Dr. Tzu-Yuan Yiin and Dr. Marty Barmatz.

I would like to thank the undergraduate assistant who worked with me, Kyle Alvine, who performed the resistivity measurements and prepared many of the mechanically attrited samples.

I am grateful to Dr. Channing Ahn, who did some of the transmission electron microscopy (TEM) and to Carol Garland who also did some TEM and who trained me to do TEM.

Prof. Lawrence Anthony kindly provided the lattice dynamics code that was used for calculating the phonon DOS and the dynamical structure factors.

This work was supported by the U. S. Department of Energy under contract DE–FG03–86ER45270.

Abstract

The vibrational and magnetic properties of mechanically attrited nanocrystalline Ni_3Fe powders were studied. The as-milled Ni_3Fe powders were annealed to create nanocrystalline samples with different grain sizes, RMS strains, and grain boundary atomic structures. The average grain size and RMS strain of the samples were measured using x-ray diffractometry and transmission electron microscopy. From inelastic neutron scattering experiments, the phonon density of states (DOS) of various as-milled and annealed Ni_3Fe nanocrystalline powders were determined. At low energies (<15 meV), nanocrystalline samples compared to bulk Ni_3Fe showed an enhancement in the phonon DOS that was proportional to the density of grain boundaries in the powders. A broadening of features in the phonon DOS was also observed for the smallest nanocrystals. The room temperature phonon DOS of nanocrystals with an average grain size of 6 nm and a large grain boundary volume fraction of 20%, was different from the phonon DOS of the same powder after it had been exposed to 10 K. It is believed that upon exposure to 10 K the grain boundary local atomic structure changed affecting the vibrational properties of the sample.

The magnetic properties of nanocrystalline Ni_3Fe were studied using Mössbauer spectroscopy, M-H magnetization curves, complex permeability measurements using microwave cavity perturbation technique, and small angle neutron scattering. M-H magnetization curves and cavity perturbation measurements showed that the coercivity and magnetic saturation are related to nanocrystal grain size and RMS strain while the complex permeability is intricately related to grain size and frequency. Both Mössbauer spectroscopy and small angle neutron scattering showed that the grain boundary magnetic moment density of as-milled Ni_3Fe nancrystalline powder was smaller than that of powder annealed at low temperature. This indicates that local atomic structure in the grain boundary affects the magnetic moment density.

Table of Contents

List of Figures

List of Tables

Chapter 1

Introduction

1.1 Nanocrystalline Materials

In the past decade there has been widespread interest in "nanostructured materials," defined here as materials having internal structures with spatial scales on the order of 20 nm or less. Research is active in nanostructured polymers, metals, and semiconductors. Examples include control of structures in diblock copolymers[1,2], magnetic properties of nanocrystalline ferromagnets[3,4], and optical properties of GaAs quantum dots[5]. Some of the interest arises from the challenge of controlling material structures on a small spatial scale, and characterizing their microstructures with new methods of microscopy, diffraction, and spectroscopy.

A more durable interest in nanostructured materials originates with their unconventional properties. Broadly speaking, there are two classes of microstructure-properties relationships unique to nanocrystalline materials, "confinement effects" and "interface effects." An example of a confinement effect is the shift in frequency of optical absorption that occurs in semiconductors when the crystallite size is comparable to the size of the electron-hole excitation[6]. An alleged example of an interface effect has been reported in nanocrystalline TiO_2. At low temperatures, this ceramic material has a surprisingly high ductility, which is attributed to atom movements in its copious grain boundaries[7].

There are many ways to synthesize nanostructured materials, including methods of wet chemistry, sol-gel reactions, physical vapor deposition, self-assembly in polymer blends, and highly controlled methods, such as molecular beam epitaxy. In the present work, the

nanocrystals studied were prepared by mechanical attrition. In mechanical attrition processing metal powders are sealed in a hardened steel vial with several steel balls, and shaken violently for several hours by a mechanical device similar to a paint shaker. The mechanism by which nanocrystals are generated by mechanical attrition is not fully understood, but it involves the generation of crystalline defects, and the coalescence of defects into structures that provide misorientation between different crystallites. In nanocrystalline materials prepared by high-energy ball milling, the shapes of the crystallites are irregular, and have a broad size distribution. The advantages of mechanical attrition versus other methods are that processing is simple and inexpensive, and large amounts of powder can be produced in a reasonable time.

The powder resulting from mechanical attrition typically contains large micron sized particles composed of a three-dimensional mosaic of irregularly shaped nanocrystals. The grain boundaries between the nanocrystals are relatively disordered in that they contain a variety of interatomic spacings. This unique combination of a large density of disordered interfaces and crystals with long-range translational order is what gives rise to the "interface effects" associated with nanocrystals. Early studies of consolidated gas-condensed nanocrystals claimed that the grain boundaries were highly disordered and "gas-like" in structure[8]. Later, more precise diffraction experiments disproved this theory[9,10]. The properties of nanocrystals' grain boundaries are not fully understood, however, and probably vary depending upon the method of nanocrystal synthesis.

1.2 Motivation for the Present Research

Nanocrystalline materials are generally expected to be unstable thermodynamically, owing to the energy cost of their numerous internal interfaces. This thermodynamic

instability can be mitigated by various kinetic or thermodynamic phenomena[11-20]. One suggestion was that a high entropy of the nanocrystalline microstructure could help stabilize it at finite temperatures[11,13,14]. A large vibrational entropy of nanocrystalline microstructure was suggested by measurements of heat capacity[11], although contamination by interstitial He atoms may have impaired these measurements[21]. Measurements of Debye-Waller factors and Lamb-Mössbauer factors showed large mean-squared atomic displacements in nanocrystalline materials, suggesting that these materials may have large vibration entropies[22-26].

Neutron inelastic scattering spectra have recently been measured on nanocrystalline materials. In a study of nanocrystalline Ta (10-nm crystallite size) prepared by mechanical attrition[27], the authors reported a smoothing of features in the density of states of the nanocrystalline material, but no overall softening of the vibrational spectrum. On the other hand, in recent inelastic neutron scattering studies of nanocrystalline Ni_3Al (7-nm crystallite size)[28], in nanophase Ni prepared by gas condensation (10-nm crystallite size)[29], and in nanophase Fe prepared by high-energy ball milling (12-nm crystallite size)[30], a large enhancement of the vibrational DOS at low energies was reported. Although the report on the nanophase Ni study suggested that quasielastic scattering by hydrogen in the material could be important at these low energies, no interstitial hydrogen was detected in the studies on nanophase Ni_3Al or Fe[30]. It was suggested that the enhancement of the vibrational DOS at low energies involved movements of the nanocrystallites with respect to each other[30]. The effects of nanocrystals on the phonon DOS are not well understood, and this motivated the present, more extensive, inelastic neutron scattering study on nanocrystalline Ni_3Fe. The alloy Ni_3Fe was chosen because it is possible to prepare it in nanocrystalline form in sufficient quantity for inelastic neutron scattering measurements. The thermal neutron scattering cross sections of Ni and Fe are large, and the lattice dynamics are known for single crystals of fcc Ni_3Fe. Furthermore, preliminary

measurements on this material showed large differences in the phonon DOS of nanocrystalline Ni_3Fe and a control sample having larger crystals[31].

Ni_3Fe is also an advantageous alloy to study because it is ferromagnetic. Magnetic properties of nanostructured metallic alloys are topics of much ongoing fundamental and applied research. Research in nanostructured magnetic materials with especially low coercive fields has been stimulated by the commercial product "Finemet," which comprises bcc Fe-Si nanocrystallites within an amorphous matrix[3,4]. Its extremely soft magnetic properties have been explained by the "random anisotropy model"[32], which basically states that when the crystal's grain size is smaller than the width of a magnetic domain wall, there will be little tendency for the crystalline orientations to affect the energy of magnetic orientation in the material. Although this argument is partially valid, internal stresses and the amorphous interfaces between the Fe-Si crystallites also affect the material response to magnetic fields.

Internal stresses also affect the magnetic permeability and coercive field of nanocrystalline ferromagnets[33]. In previous work, a number of nanocrystalline materials with soft magnetic properties were made by mechanical attrition; however, high internal stresses caused the as-milled materials to have modest coercive fields. Annealing the as-milled powders at low temperatures provided the needed stress relief, and a reduction of coercive field. Thus, the magnetic properties of mechanically attrited nanocrystalline materials are a complicated combination of effects from many factors, such as crystal size and internal stress.

By studying the magnetic properties of mechanically attrited Ni_3Fe nanocrystals, I hoped to obtain a better understanding of how these factors affect the magnetic properties of the nanocrystalline powder. Furthermore, because the augmentation at low energy of the phonon density of states is probably an "interface effect," studies of the magnetic properties of the grain boundary were made in hopes of finding a relationship between grain boundary characteristics and the vibrational properties of the nanocrystals.

Chapter 2

Synthesis and Physcial Characterization of Ni_3Fe Nanocrystals

Ni_3Fe nanocrystals, with various average grain sizes, were made by mechanical attrition. The mechanically attrited, as-milled powders were annealed at different temperatures to produce samples with different average grain sizes and different internal strain. X-ray diffraction patterns were used to evaluate the average size and internal strain of the various samples. X-ray diffraction patterns were also used to evaluate the amount of Fe bcc impurity crystallites present in the Ni_3Fe samples. TEM micrographs showed that the nanocrystals were densely packed in larger particles.

2.1 Nanocrystal Processing

The nanocrystalline Ni_3Fe powders were prepared by mechanical attrition. This is a brute-force method in which nanocrystals are formed by forcefully shaking, for several hours, the powders in a steel vial with steel balls. The mechanism of nanocrystal formation by this mechanical attrition method is not fully understood, but it involves the generation of crystalline defects, and the coalescence of defects into structures that provide misorientation between different crystallites. The end result is a powder with 10-mm diameter particles, containing a three-dimensional mosaic of irregularly shaped nanocrystals that are joined together by disordered grain boundaries (Fig. 2.1). Nanocrystals made by mechanical attrition typically have residual strain and a broad distribution of grain sizes.

Ni_3Fe nanocrystals were made by placing the stoichiometrically correct amounts of nickel and iron powders into steel vials with three 0.5-inch and three 0.25-inch steel balls

in a SPEX 8000 mixer mill. The ball-to-powder weight ratios used were 2:1, 5:1, or 20:1. Along with the powder, ethanol was placed in the vial. During mixing, the vials are shaken in a figure-eight pattern, causing the steel balls to energetically impact the powder, alloying the powder, and creating nanocrystals.

For producing Ni_3Fe nanocrystals, the addition of ethanol was found to result in a smaller average grain size and a decrease in an impurity bcc iron phase, believed to be from broken-off pieces of steel ball. These effects most likely result from the ethanol acting as a lubricant. For the 2:1 powders, 7.5 ml of ethanol and a processing run time of 12 hr were used. The 5:1 and the 20:1 powders used respectively 5 ml ethanol with a run time of 6 hr and 2 ml ethanol with a run time of 18 hr. There was no obvious correlation between the ball-to-powder weight ratio and the amount of ethanol that yielded the best results. The appropriate amount of ethanol for each ball-to-powder weight ratio was found through trial and error.

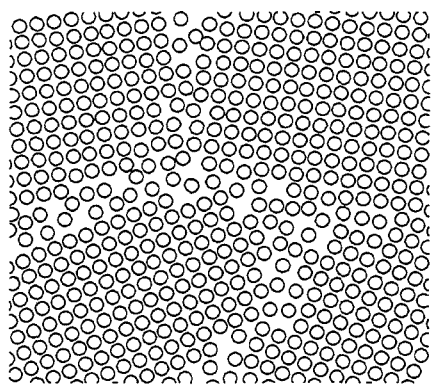

Figure 2.1. Nanocrystals made by mechanical attrition are in clusters and are joined together by disordered grain boundaries.

Contamination of the powders during processing was prevented by sealing the vials in an inert argon atmosphere and by using special vials with knife edges and a copper gaskets. The steel vials consisted of four parts: the lid, the cap, the copper gasket, and the vial body (Fig. 2.2). The lid and vial body were machined with knife edges so that when the lid of the vial was tightly screwed on, the copper gasket was cut by the knife edges and a seal impervious to gas molecules was formed.

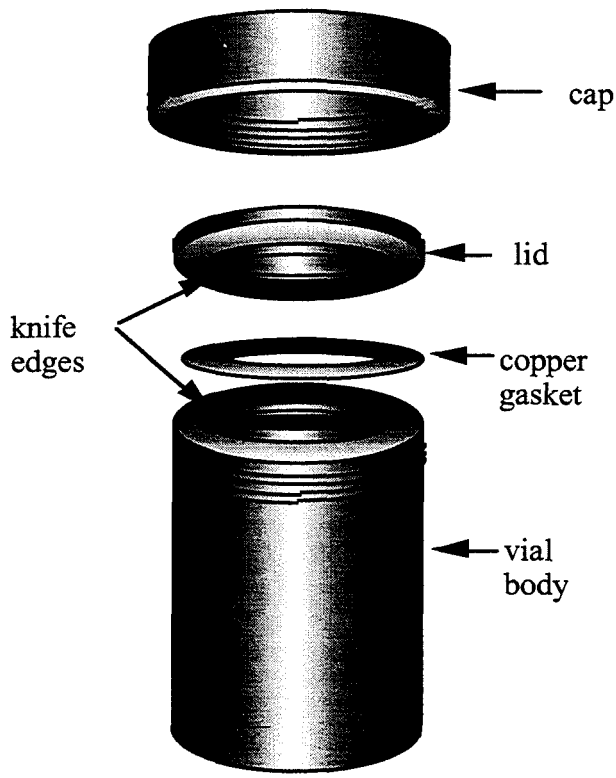

Figure 2.2. Vial components: cap, lid, copper gasket, and vial body.

Sample	Processing
20:1 as-milled	20:1 ball to powder weight ratio milled 18 hr with 2 ml ethanol
5:1 as-milled	5:1 ball to powder weight ratio milled 6 hr with 5 ml ethanol
5:1 265°C annealed	5:1 as-milled powder annealed at 265°C for 1.5 hr
5:1 425°C annealed	5:1 as-milled powder annealed at 425°C for 1.5 hr
5:1 600°C annealed	5:1 as-milled powder annealed at 600°C for 1.5 hr
2:1 as-milled	2:1 ball to powder weight ratio milled 12 hr with 7.5 ml ethanol
2:1 265°C annealed	2:1 as-milled powder annealed at 265°C for 1.5 hr
2:1 425°C annealed	2:1 as-milled powder annealed at 425°C for 1.5 hr
2:1 600°C annealed	2:1 as-milled powder annealed at 600°C for 1.5 hr

Table 2.1. Samples and how they were processed.

Chemical analysis was performed on 5:1 Ni_3Fe powder. A few grams of powder were heated to 400°C and analyzed for evolved hydrogen, oxygen, and nitrogen, using a Hewlett-Packard 5890 gas chromatograph. Gas chromatography detected no evolution of hydrogen, within the detection limits of 0.004 wt %. I also measured 0.003 wt % nitrogen, 0.001 wt% carbon and 0.003 wt % oxygen. Atomic absorption spectrometry by an independent laboratory, was used to analyze the concentration of Fe and Ni in the final powders. The Fe concentration was typically enriched by about 1%.

To create nanocrystals with a range of sizes and strains, 2:1 and 5:1 as-milled nanocrystalline powders were annealed at various temperatures. Before annealing, the sample was placed in either a Pyrex or quartz ampoule and under vacuum. As shown in Section 2.3 by annealing at low temperatures (about 200°C), strain is relieved while grain growth is minimal. At higher temperatures (>600°C), grain growth occurs rapidly. The amount of grain growth and strain relief was determined by analysis of x-ray powder diffraction patterns. The samples used in experiments described later in the thesis and how they were processed are listed in Table 2.1.

2.2 X-ray Diffraction

X-ray diffractometry was performed with an Inel CPS-120 diffractometer using Co Kα radiation. Fig. 2.3 presents x-ray diffraction patterns from the as-milled powder and from the same powder after annealing. Grain sizes and distributions of internal strains were obtained by the method of Williamson and Hall[34] after correcting the peak shapes for the characteristic broadening of the x-ray diffractometer.

The observed diffracted peak profile, O(k), is a convolution of the instrument function and the sample function,

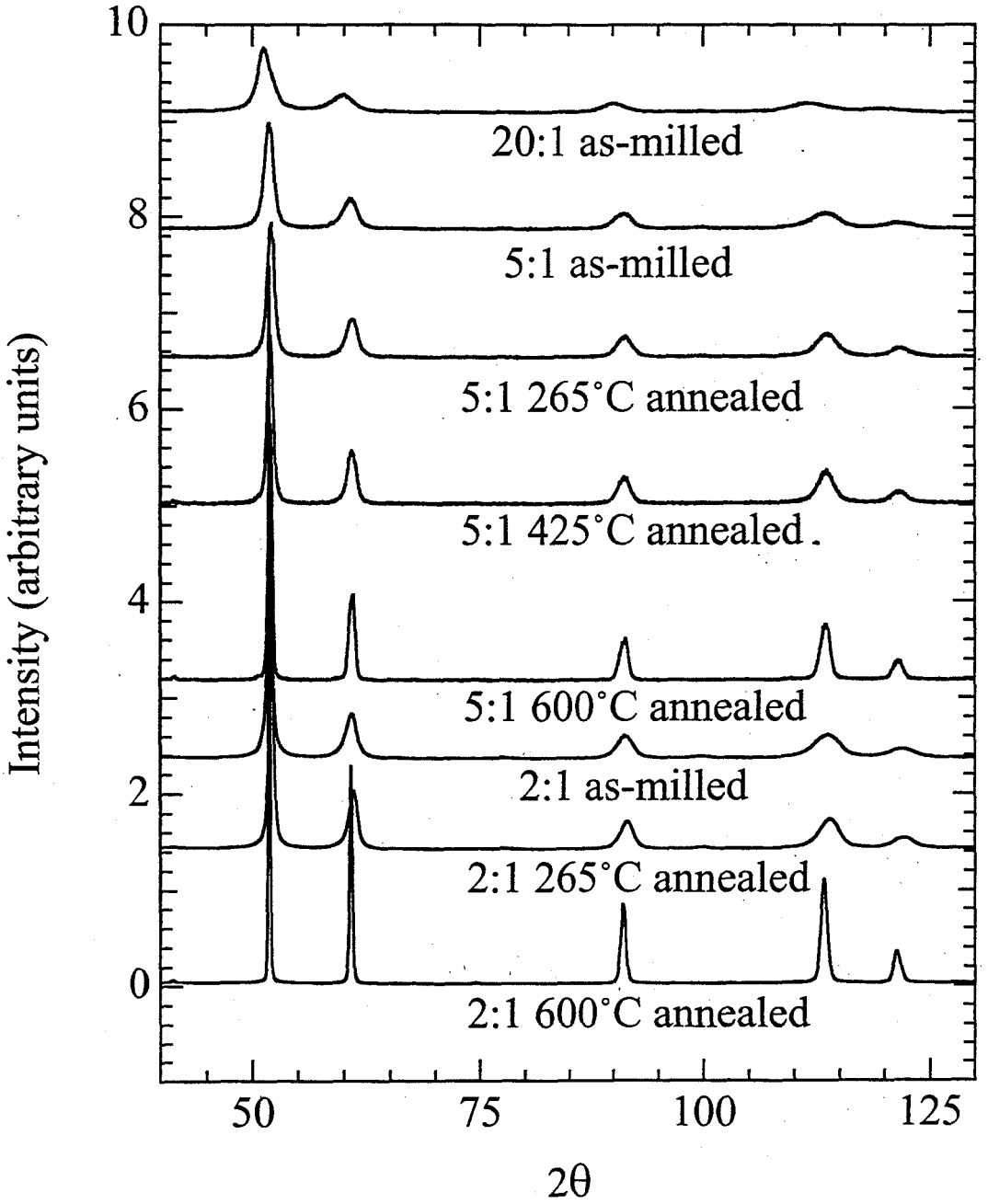

Figure 2.3. X-ray diffraction patterns of various as-milled and annealed Ni_3Fe samples.

$$O(k) = I(k)*S(k) \qquad (2.1)$$

where $k = \frac{2\sin(\theta)}{\lambda}$. The observed, instrument, and sample functions can be represented as Voigt functions, which are convolutions of a Gaussian and Lorentzian function:

$$G_O(k)*L_O(k) = G_I(k)*L_I(k)* G_S(k)*L_S(k)$$

The Gaussian and Lorentzian components are obtained separately from a Voigt function fit. Since convolutions are associative:

$$G_O(k)*L_O(k) = [G_I(k)* G_S(k)]*[L_I(k)* L_S(k)]$$

so:

$$G_O(k) = G_I(k)* G_S(k) \quad » \quad \sigma_o = \sqrt{\sigma_I^2 + \sigma_S^2}$$

$$L_O(k) = L_I(k)* *L_S(k) \quad » \quad \gamma_O = \gamma_I + \gamma_S$$

where σ is the standard deviation of the Gaussian function and γ is the characteristic half-width of the Lorentzian:

$$G(k) = \left(\frac{\sigma}{\sqrt{\pi}}\right)e^{-\left(k/\sigma\right)^2}$$

$$L(k) = \frac{\gamma}{\pi} \frac{1}{\gamma^2 + k^2}$$

So, by fitting both the observed peak profile and the instrument function to Voigt functions, the Lorentzian and Gaussian breadth components of the sample function can be determined. After the instrument contribution to the diffraction peak width has been subtracted, strain and crystal size are determined by the relation:[34]

$$\delta k = \frac{0.443}{L} + 1.18k\sqrt{\langle \varepsilon^2 \rangle} \qquad (2.2)$$

where δk is the HWHM of a predominately Lorentzian-shaped diffraction peak, L is the length of the crystal, k is the position of the peak in k space, and ε is the strain.

A polycrystalline Si powder and the 600°C annealed Ni_3Fe nanocrystalline samples were used as standards for determining the instrument function. The crystals of the Si and Ni_3Fe samples were oriented randomly and were large enough to suppress size broadening. The standard's diffraction peaks were fitted to Voigt functions. Using the derived widths of the Gaussian, σ_I, and Lorentzian, γ_I, components of the Voigt function, the instrument function was calculated as a function of angle. The observed diffraction peaks of the nanocrystalline sample diffraction peaks were also fitted to a Voigt with Gaussian, σ_O, and Lorentzian, γ_O widths. The sample function was then plotted as a Voigt function with a Gaussian component $\sigma_o = \sqrt{\sigma_I^2 + \sigma_S^2}$ and a Lorentzian component $\gamma_S = \gamma_O - \gamma_I$. The breadth of this peak, δk, was then measured and plotted as a function of peak position in k space. Because different crystallographic directions can have different average crystal sizes and different amounts of strain, there was scatter in the plots and the points did not fall neatly

on a line. For this reason, the data was linearly fitted to the (111) family for analysis of the strain and crystal size.

Fig. 2.4 shows a plot of g_S as a function of k for Ni_3Fe powders annealed at various temperatures. Note that if a linear fit of the points were applied to Eq. 2.2, the average crystal size would be

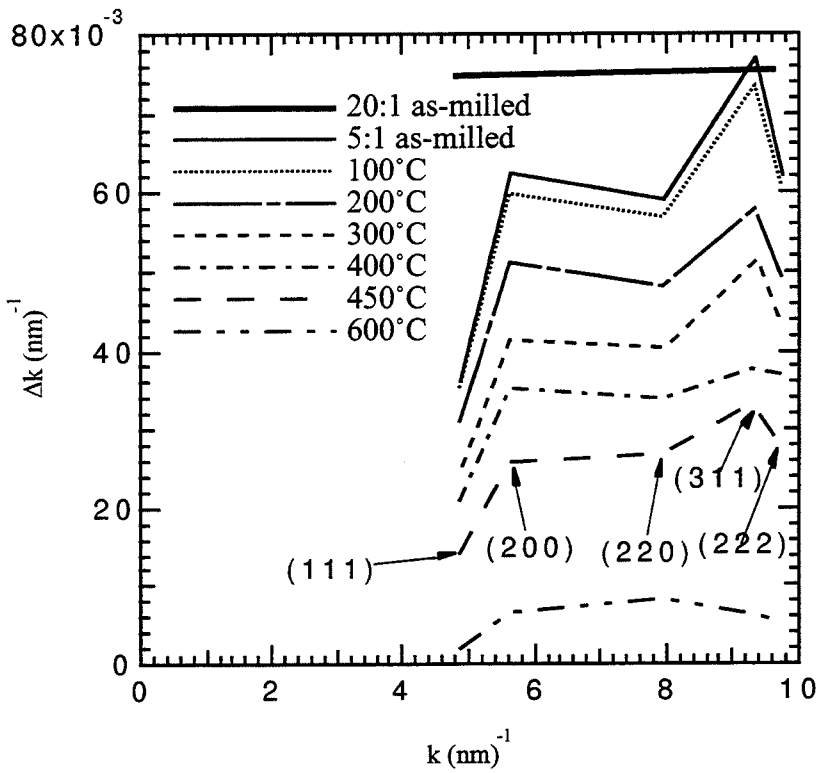

Fig. 2.4. Peak breadths in k-space versus diffraction vector for x-ray diffraction peaks from nanocrystalline Ni_3Fe samples. Data are from as-milled samples and 5:1 powders annealed at various temperatures for 1.5 hours. The slope and offset of the curves show how low temerature annealing results in small grain growth and strain relief while annealing at high temerature further relieves strain and creates large grained samples. Treands seen in this graph were used to choose the annealing temperatures of the samples studied

$$L = \frac{0.443}{(\delta k \text{ intercept})}$$

Unfortunately, there are some cases of negative intercepts, implying that some of the samples have negative crystal sizes. This is clearly not correct. Instead, the average crystal size was derived from the breadth of the 111 peak, the lowest order peak in the Ni_3Fe diffraction pattern

$$L = \frac{0.443}{\delta k(111 \text{ peak})} \tag{2.3}$$

This procedure cannot be justified a priori, but we found good agreement was between L obtained with Eq. 2.3 and the grain sizes from TEM dark field images. The RMS strain is still derived from a linear fit of the points and application of Eq. 2.2

$$\sqrt{\langle \varepsilon \rangle^2} = \frac{\text{slope of line between data points for (111) and (222) peaks}}{1.18}$$

When the as-milled and 100°C annealed samples are compared in Fig. 2.4, there is little difference in the positions of the points, showing that there is no relaxation of internal stress. Starting at 200°C, there is a large change in the relative positions of the points and the scatter of the points is less, indicating a reduction in mean-squared strain. As the annealing temperature is raised further, the slope of the points becomes less steep and the δk of the (111) peak decreases, indicating a further reduction in strain and faster rate of grain growth. Results of size and strain analysis are summarized in Table 2.1. This process of minor change in the nanocrystals followed by strain relief, then increased grain growth with increasing annealing temperatures, has been seen before in work done by J.

Eckert *et al*[35,36]. In his work, the process was monitored by differential scanning calorimetry.

Because of the observed process of strain relief and grain growth, nanocrystals were annealed at < 300°C to reduce strain while causing little grain growth. Annealing at 425°C was done to relieve strain and cause a small amount of grain growth. Annealing at 600°C produced a large-grained polycrystalline material, which was used as a bulk control sample.

sample	crystal size (nm)	RMS strain (%)
20:1 as-milled	6.0	0.01
5:1 as-milled	12	0.45
5:1 265°C annealed	16	0.31
5:1 425°C annealed	27	0.26
5:1 600°C annealed	~100	0.06
2:1 as-milled	15	0.78
2:1 265°C annealed	20	0.45
2:1 600°C annealed	~100	~0

Table 2.2. Average crystal sizes and RMS strains of Ni_3Fe powders studied.

2.3 BCC Impurity Phase

We believe that the bcc impurities are Fe-rich, and unavoidably comes from pieces of the steel balls breaking off during the attrition process. The impurity bcc phase was

detected in some x-ray diffraction patterns. X-ray diffraction patterns also show that the Fe impurities dissolve after annealing. I believe that the Fe impurity comes from the steel balls. Strong circumstantial evidence for this is that the balls are visibly damaged after the mechanical attrition process, and because the amount of impurity was reduced by using new balls with each processing of powder. The amount of ethanol used also affects the amount of impurity. As stated earlier, it is believed the ethanol might act as a lubricant and reduce the abrasive effects of the powder on the steel balls and vials.

From x-ray diffraction patterns, the areas of the Fe bcc (310) peak and the Ni_3Fe (220) peak were measured. The relationship between the peak areas is

$$\frac{A_{310}^{Fe}}{A_{220}^{Ni_3Fe}} = \frac{(\text{realative intensity of 310 Fe peak})(\text{scattering intensity from Fe})x}{(\text{realative intensity of 220 } Ni_3Fe \text{ peak})(\text{scattering intensity from } Ni_3Fe)(1 - x)}$$

where x is the fraction on bcc Fe impurity. The results are presented in Table 2.3.

Sample	Volume Fraction
20:1 as-milled	0.04
5:1, as-milled	0.05
5:1, 265°C annealed 1.5 hr	0.02
5:1, 425°C annealed 1.5 hr	0
5:1, 600°C annealed 1.5 hr	0
2:1, as-milled	0.05
2:1, 265°C annealed 1.5 hr	0.04
2:1, 600°C annealed 1.5 hr	0

Table 2.3. Volume fraction of bcc Fe impurity phase

2.4 Transmission Electron Microscopy

Both as-milled and annealed materials were studied by transmission electron microscopy (TEM) with a Philips Em 420 microscope operated at 120 keV. Samples were prepared either by embedding some of the powder in epoxy and microtoming thin sections from the epoxy block or by sprinkling some of the powders on holey carbon grids. Sizes of the nanocrystals were determined by dark field imaging, which reveals a two-dimensional projection of the outer boundaries of the crystallites. Chemical analysis with an x-ray fluorescence spectrometer attached to the microscope showed little variation in the chemical composition within the powder particles. There was good agreement between the spectral intensities from these samples and the intensities from samples of Ni - 25 at. % Fe prepared as an ingot by arc melting.

Dark field TEM images showed that the micron and submicron powder particles were dense and without internal porosity. The nanocrystals can be described as forming a three-dimensional mosaic tiling of the larger powder particles. Some dark field TEM images are presented in Figs. 2.5 and 2.6 These dark field images show a distribution in the crystallite (grain) sizes in the as-milled and annealed samples. Some extremely small crystallites are evident in the material as-milled with a ball-to-powder weight ratio of 20:1. Typical grain sizes of the powders milled with the 5:1 ratio were 6 to 10 nm, whereas the samples annealed at 600°C had grain sizes of 50 nm and larger. This estimate of a 50-nm grain size from TEM should be more accurate than is the x-ray diffraction because the x-ray linewidths from the samples annealed at 600°C were comparable to the instrumental broadening. It is also important to note that the TEM dark field images show the two-dimensional projection of diffracting crystallites, whereas lineshapes in x-ray diffractometry are a volume average over all diffracting columns of crystallites.

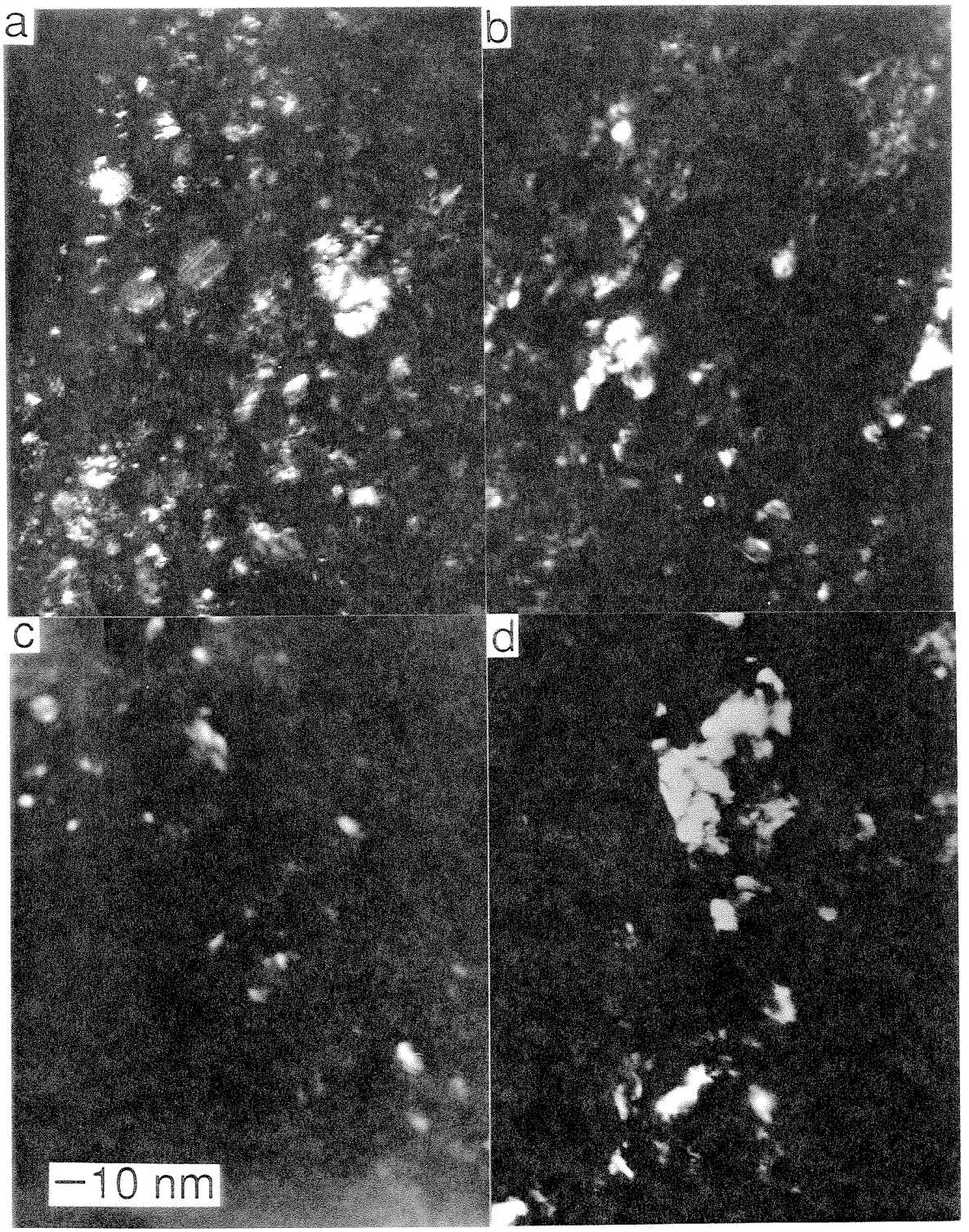

Figure 2.5. Dark field TEM images of Ni_3Fe powders obtained with the (111) fcc diffraction. a) 20:1 as-milled, b) 5:1 as-milled, c) 5:1 265°C annealed, d) 5:1 600°C annealed.

Chapter 3

Neutron Inelastic Scattering

Inelastic neutron scattering spectra were measured to obtain the phonon density of states (DOS) of nanocrystalline fcc Ni_3Fe. The materials were prepared by mechanical alloying, and were also subjected to heat treatments to alter their crystallite sizes and internal strains. In comparison to material with large crystallites, the nanocrystalline material shows two distinct differences in its phonon DOS. First, the nanocrystalline DOS was more than twice as large at energies below 15 meV. This increase was approximately proportional to the density of grain boundaries in the material. Second, features in the nanocrystalline DOS are broadened substantially. This broadening did not depend in a simple way on the crystallite size of the sample, suggesting that it has a different physical origin than does the enhancement in phonon DOS at energies below 15 meV. A damped harmonic oscillator model for the phonons provides a quality factor, Q_u, as low as 7 for phonons in the nanocrystalline material. The difference in vibrational entropy of the bulk and nanocrystalline Ni3Fe was small, owing to competing changes in the nanocrystalline phonon DOS at low and high energies.

3.1 Introduction

Ni_3Fe samples were prepared as disordered fcc solid solutions by high-energy ball milling, which was performed under two conditions to synthesize nanocrystallites of

different sizes. Some of the powders were annealed to relieve internal stresses, or to cause growth of their crystallites. Inelastic neutron scattering measurements were performed at 10 K and 300 K to test for anharmonic effects in the phonon DOS.

To a first approximation, we found that the distortions of the phonon DOS were larger for materials with smaller crystallites. In particular, the enhancement of phonon DOS at low energies increased with the inverse of the crystallite size. This corresponds to a distortion of the phonon DOS that increases in proportion to the density of grain boundaries in the material. However, the broadening in energy of features of the phonon DOS could be altered by thermal treatments that had little effect on the crystallite size. We suggest that the broadening of the phonon DOS is a phenomenon with a different physical origin than the enhancement of the phonon DOS at low energies.

The surface modes of adjacent crystallites will inevitably interact with each other because propagation of vibrational energy between the crystallites is expected to occur through grain boundaries and interiors. The simplest picture would be for an inter-crystalline transmission of rigid body displacements and rotations of the crystallites. There are, however, relatively few such rigid body modes when the crystallites contain 10^4 atoms. We do expect, however, that the grain boundaries will serve to propagate surface mode vibrations between the crystallites. If the grain boundaries served as springs with weak spring constants, the intra-crystalline vibrations would differ in phase between neighboring crystallites. Thus, grain boundaries play a vital role in the vibrational properties of mechanically attrited nanocrystals.

3.2 Experiment

The neutron inelastic scattering spectra were taken using the HB3 triple axis spectrometer at the High Flux Isotope Reactor at the Oak Ridge National Laboratory. The spectrometer was operated in constant-Q mode with the fixed final energy, E_f, of 14.8 meV. The energy-loss spectra were made by scanning the incident energy from 14.8 to 64.8 meV. The neutron flux from the monochromator was monitored with a fission detector, which was used to control the counting time for each data point. The incident beam on the pyrolytic graphite monochromator crystal had a collimation of 120', and 40' Soller slits were used between the monochromator and the sample. Pyrolytic graphite filters placed after the sample were used to attenuate the $\lambda/2$ and $\lambda/3$ contamination. The filtered beam passed through 40' slits before the pyrolytic graphite analyzer crystal. Following the analyzer, 80' Soller slits were used before the ^{3}He detector (Fig. 3.1). With this arrangement, the energy resolution varied between 0.9 and 2 meV, depending on the energy transfer and the slope of the phonon dispersion surface. The elastic peak was found to have a full-width at half-maximum of 1.2 meV. Spectra from each specimen were obtained at two values of Q, 3.54 and 4.60 $Å^{-1}$ and at two different temperatures, 300 K and 10 K. The first value of Q, 3.54 $Å^{-1}$, was chosen because it includes the (200) reciprocal lattice vector, and, therefore, provides good sensitivity to low-energy acoustic phonons. The second value of Q, 4.60 $Å^{-1}$, was chosen because it was nearly the highest value of Q accessible with our configuration of the HB3 spectrometer.

Samples of the as-milled and the annealed powders, each about 25 g, were placed in thin-walled aluminum cans and mounted on the goniometer of the HB3. Grain sizes and distributions of internal strains of the powders were obtained by the method of Williamson and Hall[34] after correcting the x-ray peak shapes for the characteristic broadening of the x-ray diffractometer. Mean crystallite sizes were 6 nm for 20:1 as-milled samples, and 10 nm

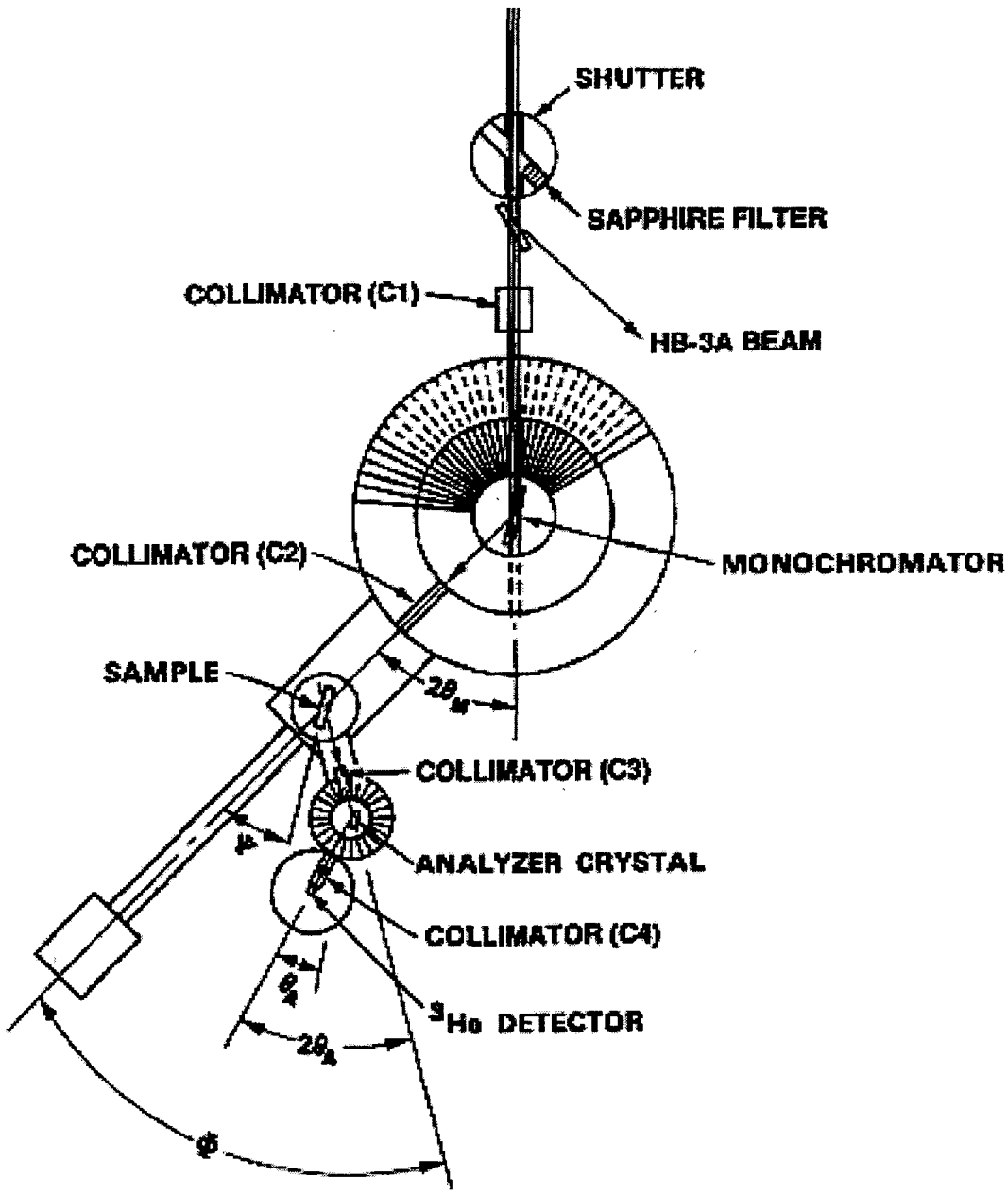

Figure 3.1. Diagram of HB3 spectrometer at Oakridge National Laboratory.

for 5:1 as-milled sample. After annealing the 5:1 as-milled (crystallite) sizes were 12 nm after 265∞C for 1.5 h, 15 nm after 425∞C for 1.5 h, and at least 25 nm after 600∞C for 1.5 h. From the slopes of the Williamson-Hall plots, the mean-squared strains were 0.4% in the 5:1 as-milled material, and 0.1% in the annealed powders. The 20:1 as-milled material had a mean-squared strain of less than 0.1%.

Although the as-milled and annealed samples were run under identical conditions, the packing densities of the samples were different. Three methods were used to normalize the intensities of the inelastic scattering spectra. We found that the intensity in the zero-loss peak was 1.33 times greater for the nanocrystalline powder than that for the annealed powder, the mass ratio was 1.25, and an approximate vibrational DOS obtained by correcting for background and one-phonon scattering provided a ratio of 1.24. To make a conservative estimate of the differences in the nanocrystalline and annealed powders, we used the normalization factor of 1.33.

3.3 Inelastic Neutron Scattering

Typical inelastic neutron scattering data are presented in Fig. 3.2. The analysis of the inelastic neutron scattering data was helped considerably by results from previous coherent inelastic neutron scattering studies on single crystals of Ni_3Fe by Hallman and Brockhouse[37]. The lattice dynamics of fcc Ni_3Fe is similar to that of fcc Ni, even when the Ni_3Fe has $L1_2$ chemical order. Using the published force constants[37], the dynamical matrix $\mathbf{D}(\mathbf{k})$[38] was diagonalized for approximately 10^6 values of $\mathbf{k}$ distributed uniformly over the first fcc Brillouin zone. Histogram binning of the resulting eigenfrequencies provided the phonon DOS, presented in Fig. 3.4.

The dynamical structure factor intensity for incoherent scattering by phonons of energy, ε, $|G_{inc}(\varepsilon,\mathbf{Q})|^2$, was obtained from the Born-von Kármán model as the following sum[39]:

$$|G_{inc}(\varepsilon,\mathbf{Q})|^2 = \sum_{\mathbf{r}_k} \frac{\sigma_{inc,\mathbf{r}_k}}{M_{\mathbf{r}_k}} \sum_{\gamma} \sum_{\mathbf{q}} |\mathbf{Q}\cdot\mathbf{u}^{\gamma}_{\mathbf{r}_k}(\mathbf{q})|^2 \, \delta(\varepsilon - \varepsilon_{\gamma}(\mathbf{q})) \qquad (3.1)$$

The dynamical structure factor intensity for incoherent scattering, $|G_{inc}(\varepsilon,\mathbf{Q})|^2$, involves the projection of the momentum transfer $\mathbf{Q}$ on the polarization vector $\mathbf{u}^{\gamma}_{\mathbf{r}_k}(\mathbf{q})$ for the atom of mass $M_{\mathbf{r}_k}$ at the position $\mathbf{r}_k$ in the unit cell of the phonon with wavevector $\mathbf{q}$ in the branch γ. Hallman and Brockhouse interpreted their data by assuming the lattice dynamics of an fcc alloy, so the atomic mass for all atoms was the average of that for 75% Ni and 25% Fe, i.e., 58.0 g/mol. For each atom, branch, and $\mathbf{q}$, the crystallographic average of Eq. 3.1 over the various directions of $\mathbf{Q}$ is $\sigma_{inc,\mathbf{r}_k} Q^2 |\mathbf{u}^{\gamma}_{\mathbf{r}_k}(\mathbf{q})|^2 / 3M_{\mathbf{r}_k}$. This contribution to $|G_{inc}(\varepsilon,\mathbf{Q})|^2$ was binned during the phonon DOS calculation.

The dynamical structure factor intensity for coherent scattering, $|G_{coh}(\varepsilon,\mathbf{Q})|^2$, was calculated as[39]:

$$|G_{coh}(\varepsilon,\mathbf{Q})|^2 = \sum_{\mathbf{r}_k} \frac{1}{M_{\mathbf{r}_k}} \sum_{\gamma} \sum_{\tau} \sum_{\mathbf{q}} |b_{\mathbf{r}_k} \mathbf{Q}\cdot\mathbf{u}^{\gamma}_{\mathbf{r}_k}(\mathbf{q}) \, e^{i\mathbf{Q}\cdot\mathbf{r}_k}|^2 \, \delta(\varepsilon-\varepsilon_{\gamma}(\mathbf{q})) \, \delta(\mathbf{Q}-\mathbf{q}-\tau) \quad (3.2)$$

where τ is a reciprocal lattice vector and b_{r_k} is the coherent scattering length. The crystallographic average of the coherent inelastic scattering required an evaluation of the dynamical structure factor intensity at explicit values of **Q** with respect to the crystallographic axes. For a given value of **Q**, the directions of **Q** were chosen with an isotropic probability distribution by using a Monte Carlo sampling procedure[28].

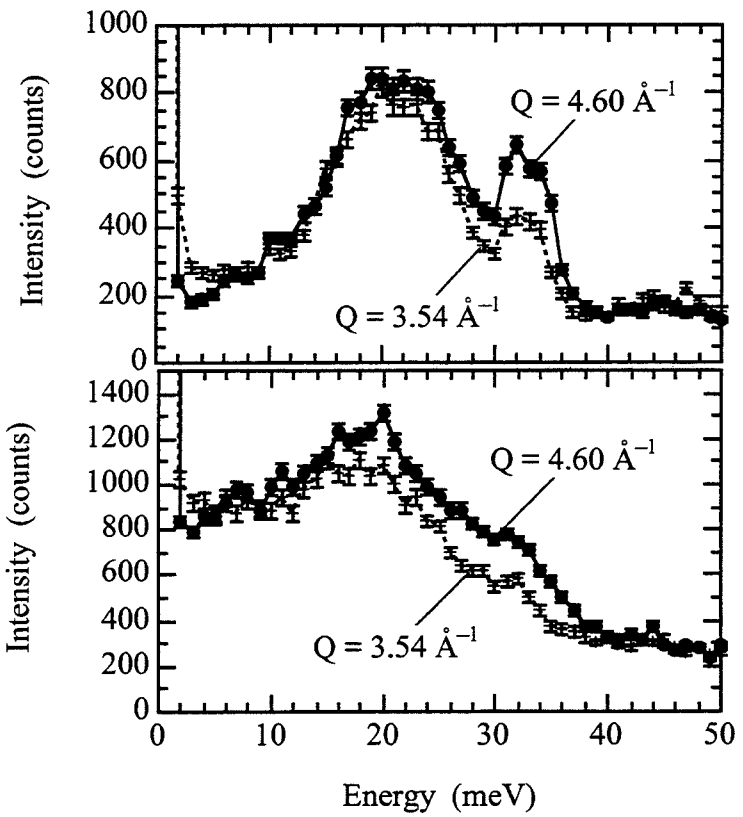

Figure 3.2. Neutron energy loss spectra obtained with Q = 3.54 and 4.60 Å^{-1}.

Top: powder 5:1 600°C annealed (average crystallite size of 60 nm).

Bottom: powder 20:1 as-milled (average crystallite size of 6 nm).

The conventional multiphonon expansion[34,40] was used to calculate the contributions to the inelastic scattering at 300 K. The calculation included the thermal occupancy factor, the Debye-Waller factor (assumed the same for Ni and Fe atoms), and the four dynamical structure factor intensities for the incoherent and coherent scattering at 3.54 and 4.6 $Å^{-1}$. The results showed that, at the relatively low values of Q and temperature of the present experiments, the inelastic scattering is strongly dominated by one-phonon processes. Results from these calculations are presented in Fig. 3.3. Fig. 3.3 shows that the incoherent inelastic scattering is skewed to higher energies owing to the thermal occupancy factor, and is stronger for Q = 4.6 $Å^{-1}$ than it is for 3.54 $Å^{-1}$. The coherent inelastic scattering, $|G_{coh}(E,\mathbf{Q})|^2$, is also shown in Fig. 3.3. Although the coherent inelastic scattering at higher E is stronger for Q = 4.6 $Å^{-1}$ than it is for 3.54 $Å^{-1}$, the intensity at lower E is much larger for 3.54 $Å^{-1}$. The Q at 3.54 $Å^{-1}$ includes the (200) reciprocal lattice vector of Ni_3Fe, and the factor $\delta(\mathbf{Q}-\mathbf{q}-\tau)$ in Eq. 3.2 allows a large contribution from small values of $\mathbf{q}$ only when $\mathbf{Q}$ is near the reciprocal lattice vector, τ. The small values of $\mathbf{q}$ emphasize the phonons of lower energy, whose thermal occupancy factor is large.

Results for the total intensity of inelastic scattering, coherent plus incoherent, were summed by weighting the coherent contribution by 0.772 and the incoherent contribution by 0.228 to account for the average coherent and incoherent scattering of Ni_3Fe. Finally, the calculated inelastic scattering intensities for the two values of Q were added together and convolved with a Gaussian function of FHWM of 2.5 meV to account approximately for the experimental energy resolution. The result is shown as the dashed curve in Fig. 3.4. The

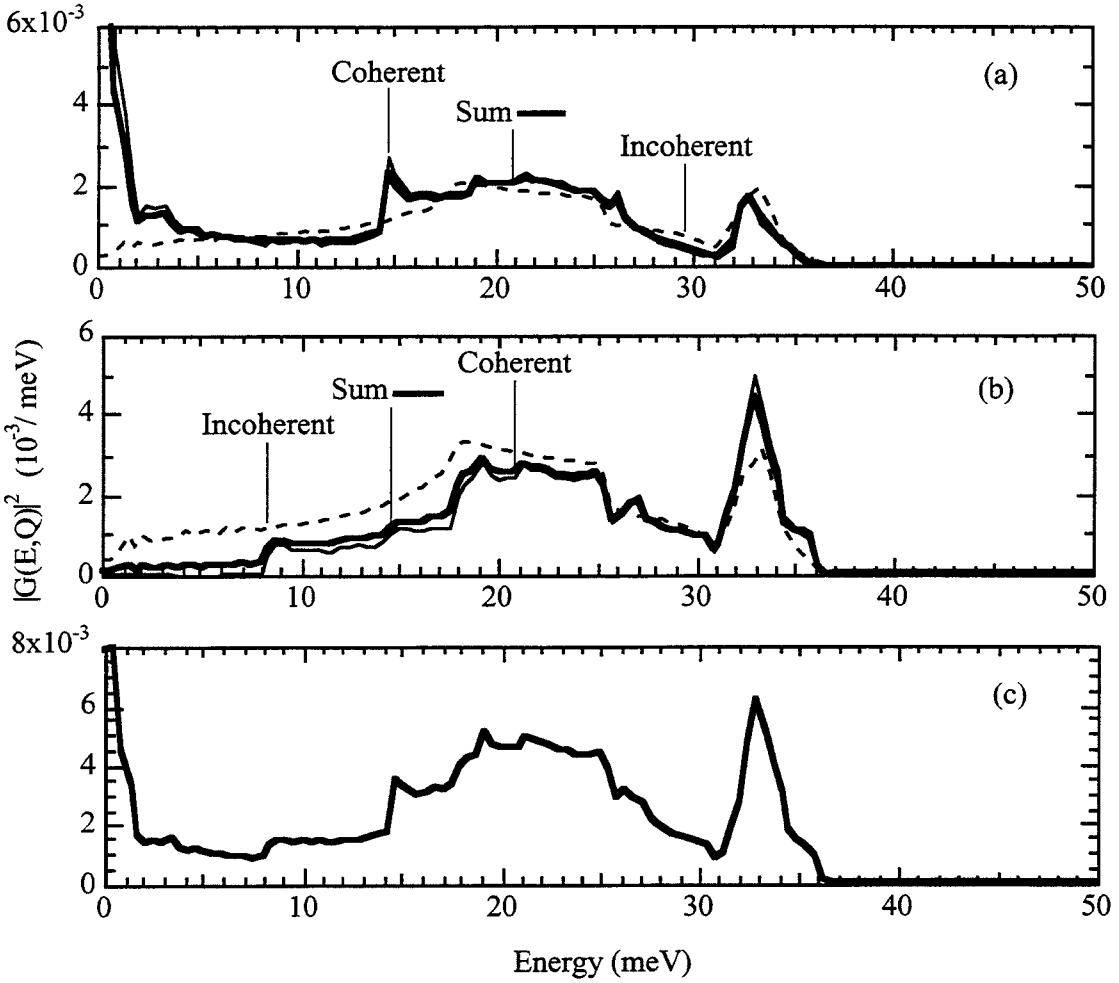

Figure 3.3. Calculated contributions to the inelastic scattering from fcc Ni_3Fe at 300 K, using the force constant data on Ni_3Fe provided by Hallman *et al.* [37].

a. Coherent inelastic scattering, incoherent inelastic scattering, and their sum, for Q=3.54 $Å^{-1}$.

b. Coherent inelastic scattering, incoherent inelastic scattering, and their sum, for Q=4.60 $Å^{-1}$.

c. Sum of coherent and incoherent inelastic scattering for both Q=3.54 and 4.60 $Å^{-1}$.

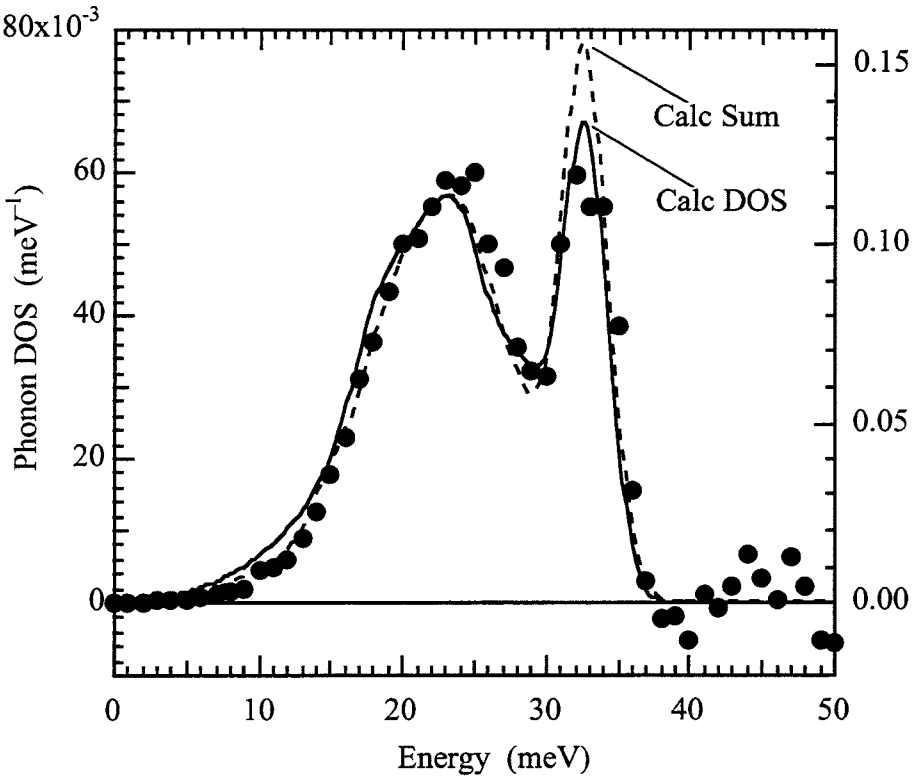

Figure 3.4. Points: Experimental phonon DOS obtained for powder annealed at 600°C. Solid curve: Calculated phonon DOS using the Born-von Kármán model with force constants of Hallman *et al.* [37] Dashed curve: Calculated sum of dynamical structure factor intensities for Q = 3.54 and 4.60 $Å^{-1}$. Calculated curves were convoluted with a Gaussian resolution function of 2.5 meV full-width-at-half-maximum.

solid curve is the actual phonon DOS of fcc Ni_3Fe, calculated with the Born-von Kármán model using the force constants of Hallman and Brockhouse, again convoluted with a Gaussian function of FHWM of 2.5 meV.

To obtain the approximate phonon DOS from the experimental spectra, the spectra measured with both values of Q = 3.54 and 4.60 $Å^{-1}$ were summed, and a constant background was then subtracted. The conventional multiphonon expansion[40-42] was used to calculate the contributions to the inelastic scattering at 300 K. The results showed that the inelastic scattering is strongly dominated by one-phonon processes. Assuming that the inelastic scattering, $I(\varepsilon)$, is all one-phonon scattering, the phonon DOS, $g(\varepsilon)$, can be obtained from the inelastic spectrum as:

$$g(\varepsilon) = \varepsilon \, [1 - \exp(-\varepsilon/kT)] \, I(\varepsilon) \qquad (3.3)$$

The experimental phonon DOS curve obtained for the large-grained annealed sample is presented in Fig. 3.4 for comparison with the calculated DOS and the calculated sum of the dynamical structure factor intensities (which should provide a more accurate estimate of the experimentally derived spectrum).

3.4 Results and Discussion

3.4.1 General Features of the Phonon DOS

The experimental phonon DOS curves for most of the samples are presented in Fig. 3.5. We anticipated that the nanocrystalline materials would show an anharmonic softening of their phonon DOS curves, but we found no significant differences between the phonon

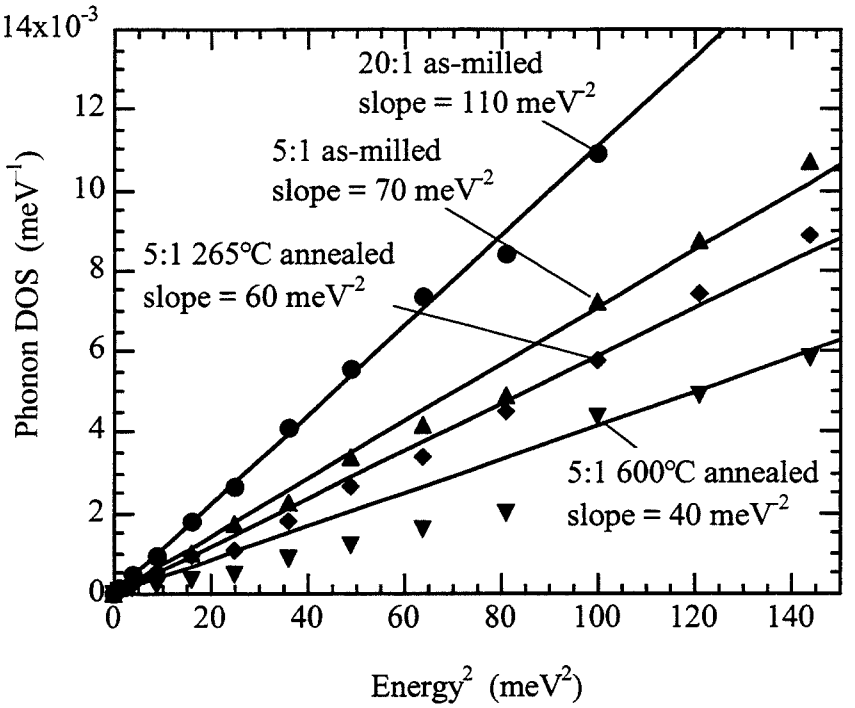

Figure 3.5. Low-energy part of the phonon DOS curves of Fig. 3.6, graphed versus the square of energy.

DOS curves measured at 10 K and at 300 K. (An irreversible change in the broadening of the phonon DOS curves of as-milled alloys after cryogenic exposure is described in Section 3.4.3, however.) In comparison to the 5:1 600°C annealed sample, which had large crystals, the phonon DOS curves from the nanocrystalline material show two distinct differences. There is an increased intensity of the phonon DOS at energies below 15 meV. This excess intensity diminishes after the nanocrystalline materials are annealed at higher temperatures. The second difference is that the features of the phonon DOS are broadened in the nanocrystalline materials. Both of these effects are also evident in raw data such as the data shown in Fig. 3.2. Although these two effects had been reported previously,[28-

[31,43] the more systematic results of the present study allow for more detailed interpretations.

3.4.2 Features at Low Energies

Fig. 3.5 shows the low energy part of the phonon DOS curves, $g(\varepsilon)$, presented in Fig. 3.6, with the data plotted against the square of the phonon energy. A quadratic dependence of the form

$$g(\varepsilon) = \alpha\, \varepsilon^2 \qquad (3.4)$$

is expected when the vibrational excitations in three-dimensions have a constant group velocity, $h^{-1}\, \partial\varepsilon/\partial q$. The function of Eq. 3.4 was fit to the data of Fig. 3.5 for the energy ranges 0 - 12, 0 - 13, and 0 - 14 meV, and the results averaged to obtain a value for α. This average α was plotted against the root-mean-squared strains in the crystallites and against the grain size of the crystallites. The correlation with the RMS strain was poor (Fig. 3.7), but the correlation against grain size was more monotonic (Fig. 3.8). Provided that the grain size distribution has the same functional form, but merely changes spatial scale with grain growth, the surface area of grain boundaries will depend on grain size, d, as d^{-1}. In other words, the density of grain boundaries per unit volume may be expected to be proportional to the inverse of the grain size. This motivated us to plot in Fig. 3.8 the coefficient α of Eq. 3.4 against the inverse of the grain size. The linearity of this plot suggests that the enhancement of the phonon DOS at low energies is a phenomenon related

to the surfaces of the crystallites, such as surface modes. Tamura, et al.[44,45], calculated the torsional and spheroidal vibrational modes of small spherical particles with relaxed surface zones. Model molecular dynamics calculations by this group[46] showed an enhanced phonon density of states at low energies, with general appearance similar to the DOS for the nanocrystalline material shown in Fig. 3.6. These surface modes will be altered when the particle is embedded in a matrix, but with an elastic discontinuity at the

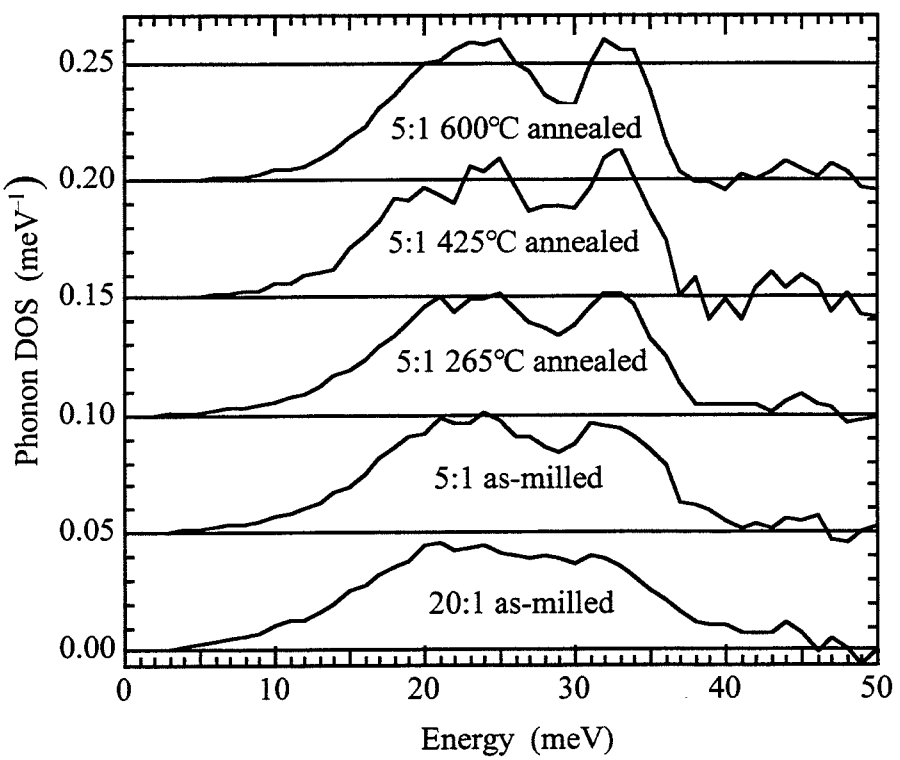

Figure 3.6. Phonon DOS curves extracted from experimental data from Ni_3Fe powders milled with ball-to-powder weight ratios of 20:1 and 5:1, and after annealing the 5:1 powder at the indicated temperatures. Crystallite sizes were (top to bottom) 50, 15, 12, 10, and 6 nm.

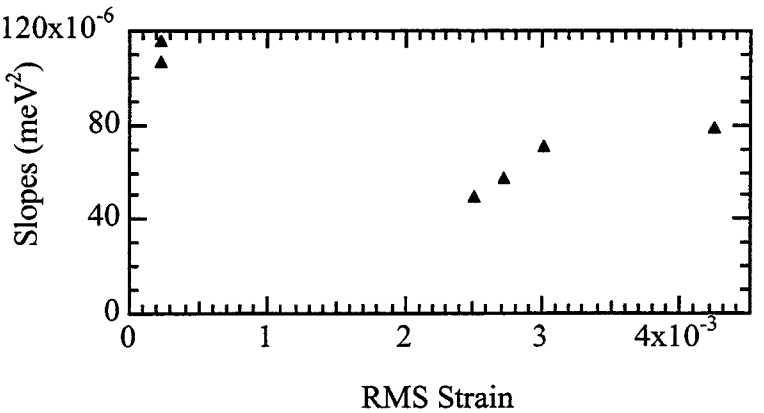

Figure 3.7. Slopes of the lines shown in Fig. 3.5 (α of Eq. 3.4) versus RMS strain of the powders.

particle interfaces, the concept of surface modes remains viable. The plot of Fig. 3.8 includes results from all measurements on as-milled and annealed materials. Although the linearity is suggestive of a quantitative relationship, our measurements may not justify such a relationship in detail. In particular, the frequency spectrum of surface modes should depend on the nature of the contacts between crystallites, and these contacts probably change during annealing. It is also likely that the effective elastic constants of grain boundaries are different in the annealed materials. Such effects are not possible to estimate reliably.

The straight line relationship in Fig. 3.5 suggests that the 20:1 nanocrystalline material may have a velocity of sound that is a factor of 3 smaller than that in the annealed material. The straight-line relationship may be misleading, however, and could originate from two different vibrational phenomena that add their densities of states in a way that appears quadratic. We attempted to perform ultrasonic pulse-echo measurements of sound velocities in compacted powders of 5:1 as-milled and 5:1 750°C annealed Ni_3Fe, but

ultrasonic absorption in the samples was too large. Ultrasonic transmission was probably impeded by the porosity in our samples. The densities of the compacted powders were 6.6 g/cm^3 for the annealed powder and 5.9 g/cm^3 for as-milled powder; owing to porosity, both of these densities are considerably lower than the expected density of 8.8 g/cm^3. It may be interesting to look for evidence of dispersion curves in inelastic neutron scattering experiments at small angles.

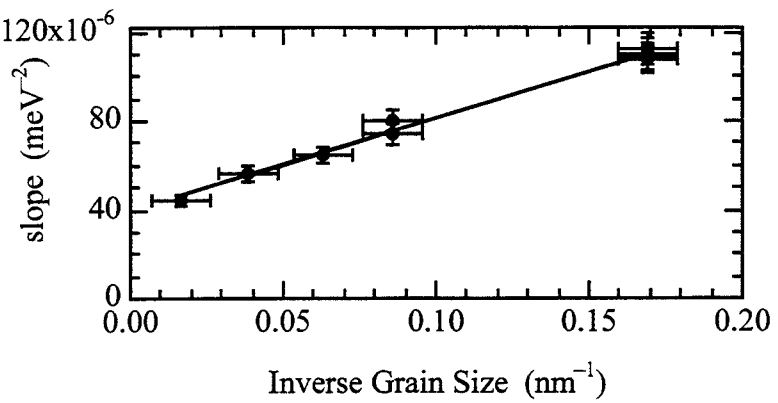

Figure 3.8. Slopes of the lines shown in Fig. 3.5 (α of 3. 4) versus the inverse of the crystallite size.

We had previously suggested that some enhancement of the vibrational DOS at low energies could originate from inter-crystallite vibrations of the nanocrystalline microstructure[30]. The idea was that there may be a lattice dynamics associated with the vibrations of the crystallites themselves, coupled by weak springs comprising the grain boundary atoms. The inelastic scattering data from the present experiment on fcc Ni_3Fe

showed much larger effects than did the previous data with bcc Fe, however, and some quantitative predictions are now possible. From the curves in Fig. 3.5, we estimate that the enhancement in the vibrational DOS below 20 meV in the 5:1 as-milled nanocrystalline material accounts for nearly 5% of all vibrational modes. One test for the plausibility of a microstructural dynamics is to check whether the enhancement of the density of states of Fig. 3.5 is consistent with the number of degrees of freedom of the microstructure as deduced from x-ray diffraction patterns and TEM micrographs (Fig. 2.5). In particular, if the crystallites are too large, there will be too few microstructural degrees of freedom to provide a microstructural density of states that can compete with the density of states from the atomic lattice of fcc Ni_3Fe. For the 5:1 as-milled material, the x-ray diffraction lineshapes indicate a mean crystallite size of 11 nm. This seems consistent with the dark field transmission electron micrographs, which show many crystallites with long dimensions in the 6- to 10-nm range. The smallest characteristic size of abundant crystallites that we could find is 5 nm. The packing of these crystallites is not clear from the TEM micrographs. For an approximate estimate, we assume fcc packing of the crystallites, so the "lattice parameter" of the nanocrystalline microstructure is a factor of 20 times larger than that of the atomic lattice of fcc Ni_3Fe.

The number of degrees of freedom in the nanocrystalline microstructure is, therefore, reduced by a factor of $20^3 = 8{,}000$ compared to the fcc atomic lattice. We can add torsional modes of vibration to the nanocrystalline microstructure to reduce this number somewhat, and we could associate the microstructural modes with the smallest crystallites in the microstructure. Nevertheless, it seems that only part of the observed enhancement of the vibrational DOS at low energies can be explained by the mesoscopic vibrational dynamics of the nanocrystalline Ni_3Fe microstructure. As another check, we note that the characteristic frequency for vibration of the microstructure should be 1/20 that of the fcc Ni_3Fe, assuming comparable velocities of sound in the nanocrystalline and annealed

materials. (This fraction will be even smaller if the velocity of sound of the nanocrystalline powder is lower than that of the annealed powder.) Fig. 3.6 provides an approximate characteristic energy for the annealed powder of 35 meV, so the comparable energy for the nanocrystalline microstructure is 1.75 meV. From Fig. 3.6, this energy seems too low by a factor of 4 or so.

Modeling the vibrational dynamics of the nanocrystalline microstructure as a set of featureless, rigid, crystallite masses connected by weak grain boundary springs seems too simple; neither the characteristic frequencies nor the number of modes seems able to account for the large effects observed experimentally. The irregular, asymmetric shapes of the crystallites may provide additional degrees of freedom for vibrations, especially if it is possible for the crystallites to distort in shape. We expect that it is inappropriate to consider the crystallites as rigid, so the low frequency vibrational modes will also involve some distortions within the crystallites. The detailed coupling between the motions of the microstructure and the internal motions of the crystallites and grain boundaries is not a problem that lends itself to a simple estimate.

A different viewpoint has been provided for understanding the vibrational spectrum of amorphous materials[47-50]. Local regions having low-frequency vibrations may interact by absorbing and rescattering vibrational waves from the surrounding matrix[50]. Perhaps some of the heterogeneities in our nanocrystalline materials could act as low frequency resonators. A model of scattering of matrix phonons by local regions with low resonant frequencies seems unlikely to provide the linear slopes of Fig. 3.5, as this model tends to show a "Boson peak" when $g(\varepsilon)\ \varepsilon^{-2}$ is plotted against ε.

3.4.3 Features at Higher Energies

Fig. 3.9 compares the experimental phonon DOS for our nanocrystalline material with the smallest crystallite size to the DOS for the annealed material with the largest crystallite size. In addition to the enhanced intensity at low energies (discussed in the previous section), there is a broadening in energy of the nanocrystalline phonon DOS. In particular, a tail extends to high energies. As a possible interpretation of this broadening, we calculated the phonon DOS for the nanocrystalline material with the assumption that each phonon was broadened in energy as a damped harmonic oscillator. Damped harmonic oscillator functions for phonons at 10 and 35 meV with oscillator quality factors[51] $Q_u = 7$ are shown in the middle of Fig. 3.9. To obtain the solid curve at the bottom of Fig. 3.9, each intensity at the energy ε' of the experimental DOS curve of the annealed material was convoluted with the characteristic spectrum of a damped harmonic oscillator:

$$D_{\varepsilon'}(\varepsilon) = \frac{1}{\pi Q_u \varepsilon'} \frac{1}{\left(\frac{\varepsilon'}{\varepsilon} - \frac{\varepsilon}{\varepsilon'}\right)^2 + \frac{1}{Q_u^2}} \tag{3.5}$$

The only free parameter in fitting the phonon DOS from the nanocrystalline material was Q_u, which was assumed to be the same for all phonons. The solid curve at the bottom of Fig. 3.9 was obtained with a value of $Q_u = 7$. Many features of the phonon DOS of the nanocrystalline material are represented well by this assumption of a damped harmonic oscillator. The shape of the high energy tail above the longitudinal peak is modeled particularly well, as is the suppressed dip between the transverse and longitudinal bands of states. The enhanced low energy part of the phonon DOS of the nanocrystalline material

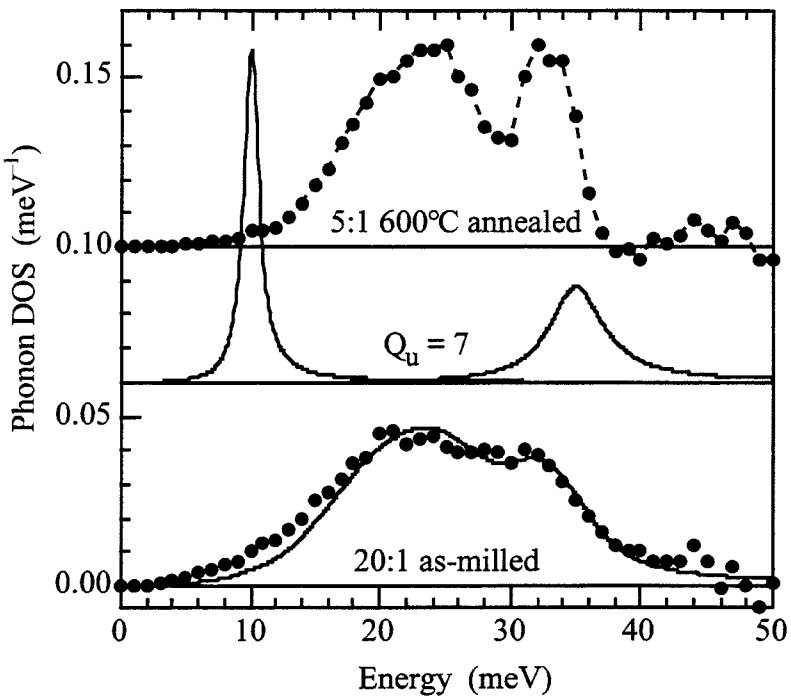

Figure 3.9. The characteristic shape of the damped harmonic oscillator function is shown in the center of the figure for resonances at 10 and 35 meV having the quality factor $Q_u = 7$. Solid curve at bottom is the convolution of the damped harmonic oscillator function for $Q_u = 7$ with the experimental DOS from the 5:1 600°C annealed sample (points at top). Points at bottom are experimental DOS curve from 6-nm 20:1 as-milled powder.

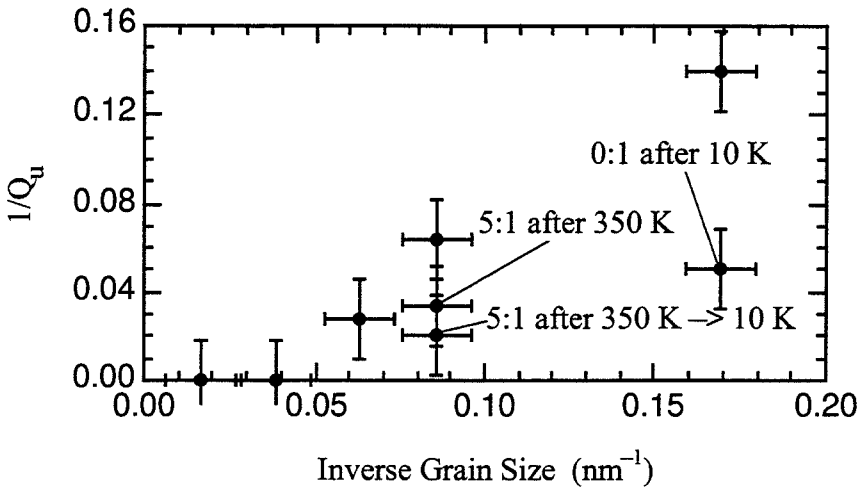

Figure 3.10. Inverse of the quality factor, Q_u, versus the inverse of crystallite size. Labels indicate additional treatments given to the samples.

(discussed in the previous section) evidently does not originate from phonon damping of this type.

The amount of damping, parameterized as Q_u^{-1}, is presented in Fig. 3.10 versus the inverse crystallite size. The systematics are not so consistent as for the enhanced phonon DOS at low energies (Fig. 3.8). This difference indicates that the damping has a different origin. In particular, the damping can be changed significantly by thermal treatments of the sample that have no effect on the grain size, such as low-temperature annealings and exposure to cryogenic temperatures. An unexpected effect of cryogenic exposure is shown in Fig. 3.11 with experimental DOS curves of the 20:1 as-milled powder (6-nm crystallites). It should be noted that the longitudinal peak in the phonon DOS of the as-milled nanocrystalline material is sharpened significantly after the sample was exposed to cryogenic temperature. Some sharpening of the transverse band of states may also occur. On the other hand, the enhanced phonon DOS at low energies is little changed. This

sharpening of the phonon DOS was irreversible. It was observed when the material was first cooled to 10 K, and remained after warming to 300 K. The phonon DOS curves obtained from the spectra measured at 10 K and after warming to 300 K were the same within experimental error. A similar sharpening of the longitudinal peak of the phonon DOS was observed after the 5:1 as-milled sample was annealed at 350 K for 8 hr, and this sharpening became more pronounced after this 5:1 material was exposed to a temperature of 10 K.

To study further this effect of cryogenic exposure on the phonon damping, we compared x-ray diffraction patterns of as-milled powders before and after immersion in liquid nitrogen at 77 K and liquid helium at 4 K for 45 mi. The diffraction patterns were identical within experimental error, indicating that changes in crystallite size or residual stress in the material are probably not responsible for the change in the phonon damping after cryogenic exposure. On the other hand, low-temperature annealings or cryogenic exposures could cause changes in local atomic structures of grain boundaries by causing the reconfiguration of those atoms in energetically unfavorable local environments. Such changes would not be evident in our x-ray diffraction patterns, but these changes would be expected to affect the anharmonic character of the vibrations of grain boundary atoms. A large anharmonicity in as-milled materials would intermix phonons of different energies, and this would be evident as damping. If cryogenic exposure or low-temperature annealing were to reduce the local atomic distortions in grain boundaries and thereby reduce the anharmonic nature of the interatomic potential, the phonon damping would be diminished. We note that a recent study of vibrations in nanocrystalline ^{57}Fe that has a large amount of free surface also showed evidence for large phonon damping[43].

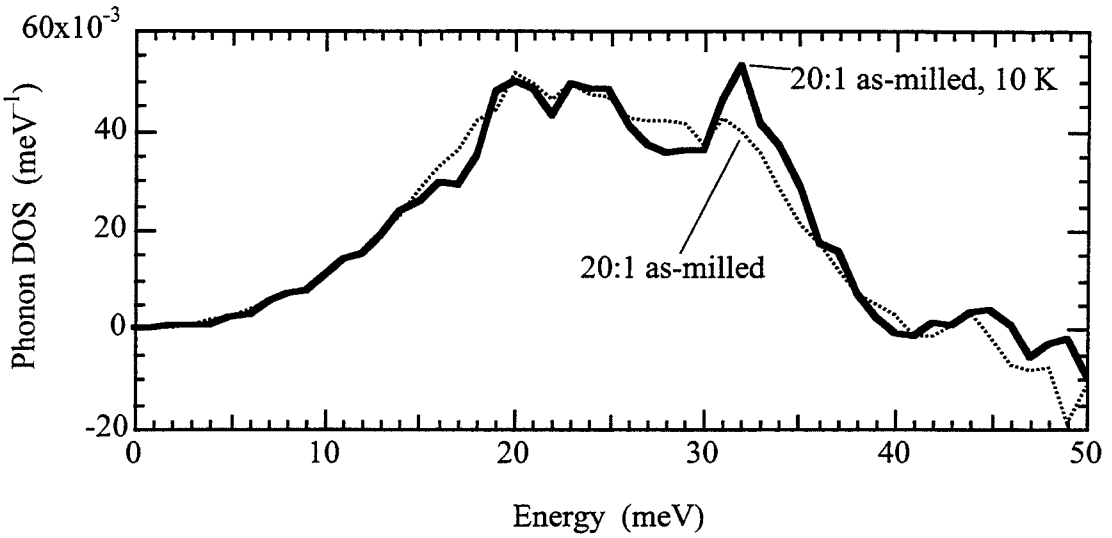

Figure 3.11. Effect of cryogenic exposure on the experimental phonon DOS curve at 300 K of the 6-nm 20:1 as-milled samples.

An alternative explanation for vibrational modes at high energies was suggested by D. Wolf, et al[52]. Their molecular dynamics simulations showed that nanocrystalline materials had low-energy modes associated with grain boundaries, approximately consistent with our results of Fig. 3.6. The molecular dynamics simulations also showed modes at energies above those of the crystallites. These high-energy modes were attributed to local atomic environments in grain boundaries with reduced interatomic separations. This explanation seems consistent with our observations, assuming again that cryogenic exposure or low temperature annealing were to reduce the local atomic distortions within grain boundaries.

3.4.4 Vibrational Entropy

Vibrational entropy has been proposed as a reason for the thermal stability of nanocrystalline materials at moderate temperatures[11,13,14]. We define $\Delta S_{vib} \equiv S_{vib}^{nan} - S_{vib}^{blk}$ as the difference in vibrational entropy of nanocrystalline and annealed Ni_3Fe. At high temperatures, this difference in vibrational entropy depends in a straightforward way on the difference in the vibrational DOS of the two phases, $g^{nan}(\varepsilon) - g^{blk}(\varepsilon)$[28,30]:

$$\Delta S_{vib} = -3k_B \int_0^\infty (g^{nan}(\varepsilon) - g^{blk}(\varepsilon)) \quad \ln(\varepsilon)\, d\varepsilon \qquad (3.6)$$

where the difference avoids problems with the dimensions of the argument of the logarithm. Using the DOS curves of Fig. 3.6, for high temperature we find that the vibrational entropy of the 20:1 as-milled alloys is larger by about 0.10 k_B/atom than it is for the 5:1 600°C annealed sample. On the other hand, the vibrational entropy of the 5:1 material is essentially the same as that of the 5:1 600°C annealed sample. Subsequent annealings at 265 and 425°C caused little change in the vibrational entropy of the 5:1 powder. Studies of other nanocrystalline materials reported vibrational entropies up to 0.2 k_B/atom larger than their bulk counterparts[28,30,31]. These other nanocrystalline materials also had significant enhancements of their phonon DOS at low energies. In the present nanocrystalline alloys, surprisingly, the large lifetime broadening of the DOS to high energies largely cancels the effects from the enhancement of the phonon DOS at low energies. On the other hand, by annealing at low temperature or by cryogenic exposure, it was possible to soften the high-energy part of the phonon DOS in the as-milled materials without affecting the phonon DOS at low energy. The softening of the high-energy part of the DOS after the 10 K quench or after annealing at 350 K caused the vibrational entropy of

the 5:1 alloy to increase by about 0.11 k_B/atom. The 10 K quench caused the vibrational entropy of the 20:1 alloy to increase by about 0.05 k_B/atom. Vibrational entropy should have only a modest effect on the thermodynamic stability of our nanocrystalline Ni_3Fe. For comparison, at 400 K a difference in vibrational entropy of 0.1 k_B/atom contributes approximately 300 J/mol to the free energy difference, which is several times smaller than the grain boundary enthalpy.

3.5 Conclusions

Inelastic neutron scattering spectra were measured from nanocrystalline Ni_3Fe prepared by mechanical alloying, and from these materials after thermal treatments. The spectra measured at constant Q were converted into approximate phonon DOS curves. Compared to the same alloy having large crystallites, the nanocrystalline materials had (1) an enhancement of their phonon DOS at low energies, and (2) a broadening of their phonon DOS, most notably at high energies. The enhancement of the phonon DOS at low energies was especially large in samples with the smallest average crystallite size, but this enhancement decreased with crystallite size, d, as d^{-1}. There was no distinct structure in this low-energy part of the phonon DOS, and the intensity increased with phonon energy, ε, approximately as ε^2. The broadening of the phonon DOS did not show a simple dependence on crystallite size. This broadening could be modeled successfully as a damping of the vibrational modes. Large reductions in this broadening were obtained with mild thermal treatments of the sample – annealing at 350 K or exposure to 10 K. We suggest that the broadening of the phonon DOS originates with anharmonic interatomic potentials in unrelaxed grain boundaries. We did not observe other anharmonic effects,

however, such as a softening of the phonon DOS between 10 K and 300 K. Finally, we note that the effects on the vibrational entropy from these two features of the phonon DOS of the nanocrystalline material tend to cancel each other.

Chapter 4

Study of the Magnetic Properties of Mechanically Attrited Ni_3Fe Nanocrystals Using Mössbauer Spectrometry

Room temperature Mössbauer spectra were taken of various nanocrystalline and bulk Ni_3Fe samples. Using the Le Caër method, the hyperfine field distribution (HFD) was obtained from the spectra. From the HFD, the grain boundary volume fractions and effective magnetic moments were calculated. The component of the HFD that originates from the grain boundaries indicated that the magnetic moments at the grain boundaries change upon annealing. A Mössbauer spectrum at 77 K was taken of Ni_3Fe nanocrystals with a characteristic grain size of 6 nm. This spectrum, when compared to the room temperature spectrum, showed that the grain boundaries are only slightly paramagnetic.

4.1 Mössbauer Overview

Mössbauer spectroscopy measures transitions between states of nuclei for specific isotopes. For the present measurements, the isotope was ^{57}Fe, which occurs naturally in the Ni_3Fe alloy. In our experimental setup the Mössbauer effect is obtained with a radioactive ^{57}Co source that can be absorbed by ^{57}Fe in the sample. The excited ^{57}Fe nuclei then admits a gamma ray which is reabsorbed by another ^{57}Fe nuclei. The Mössbauer effect itself is the process permitting this resonant absorption by having a negligible recoil energy transferred to internal excitations of the lattice. When the γ-rays are of an energy at which the Mössbauer effect occurs, there is a decrease in the amount of transmitted γ-ray

beam at the detector. These dips in the γ-ray transmission through the sample generate the Mössbauer spectra. By vibrating the Co source and Doppler shifting the emitted γ-rays, it is possible to measure the Mössbauer spectrum over a range of energies.

In the presence of a magnetic field, the nuclear angular momentum states are separated in energy (nuclear Zeeman effect) by

$$\Delta E = \mathbf{I} \cdot \mathbf{B}$$

The nuclear excited and nuclear ground states split into 4 and 2 sub-levels, corresponding to the various orientations of **I** along the direction of **B**. In a magnetic material in which there is no external applied field, **B** originates from the magnetic moments of the atoms surrounding the nucleus. Because the nuclear states of an atom are sensitive to the magnetic moments in the atoms immediate environments, the nuclear emission and absorption energies are slightly changed by the local atomic configuration in the solid. Thus, it is possible to extract from the Mössbauer spectra information about the magnetic moments present in the grain boundaries of the nanocrystalline Ni_3Fe samples.

4.2 Experiment

Mössbauer spectra were obtained with a constant acceleration spectrometer in a transmission configuration. The ^{57}Co in the Rh source is oscillated over a velocity range of ~±8 mm/s, creating a spread in energy, $\Delta E = 3.8 \times 10^{-7}$ eV, around the unshifted, E_γ=14.41 keV, gamma irradiation. At room temperature, Mössbauer spectra were taken of various Ni_3Fe samples: 20:1 as-milled, 2:1 as-milled, and 2:1 annealed at 265°C and

600°C. A Mössbauer spectrum at 72 K was also taken for the 20:1 as-milled sample by placing the sample in a liquid nitrogen cooled cryostat. The 77 K spectrum was taken by placing the samples in a He atmosphere in the sample region of a cryostat that was filled with liquid nitrogen. For the room temperature and 77 K spectra, Fe calibration spectra were taken. From the Fe spectra, the velocity shift of the transmitted γ-rays was calibrated and the source linewidth measured.

The HMF distributions were obtained from the spectra by using a program based on the method of Le Caër and Dubois[53]. This method extracts hyperfine magnetic field distributions from raw experimental data by curve-fitting with many known spectra. Variables inputted into the program were the source linewidth and the ratio between the second and first peaks of the Mössbauer sextet. By comparing the fitted with the raw spectra, it was confirmed that the proper variables had been inputted into the program.

4.3 Effects of Reduced Temperature

The set of room temperature and 77 K Mössbauer spectra were collected for 20:1 as-milled Ni_3Fe to determine if the reduced hyperfine magnetic fields in this material originated from some of the material having Curie temperatures below room temperature. Because bulk Ni_3Fe is ferromagnetic, we can assume that any paramagnetism originates from the grain boundaries. Following this reasoning, the 20:1 as-milled powder was studied because it had the largest grain boundary volume fraction. Paramagnetism in the grain boundaries would result in magnetic moments whose alignments undergo thermal fluctuations. Thus, magnetic moments with paramagnetic characteristics would be in a magnetically isotropic surrounding and would not undergo nuclear energy level splitting. This would result in the growth of a paramagnetic peak at zero velocity with an increase in

temperature[54]. Thus room temperature and 77K Mössbauer spectra of the 20:1 as-milled were compared to see if there was evidence of a paramagnetic peak in the room temperature spectra.

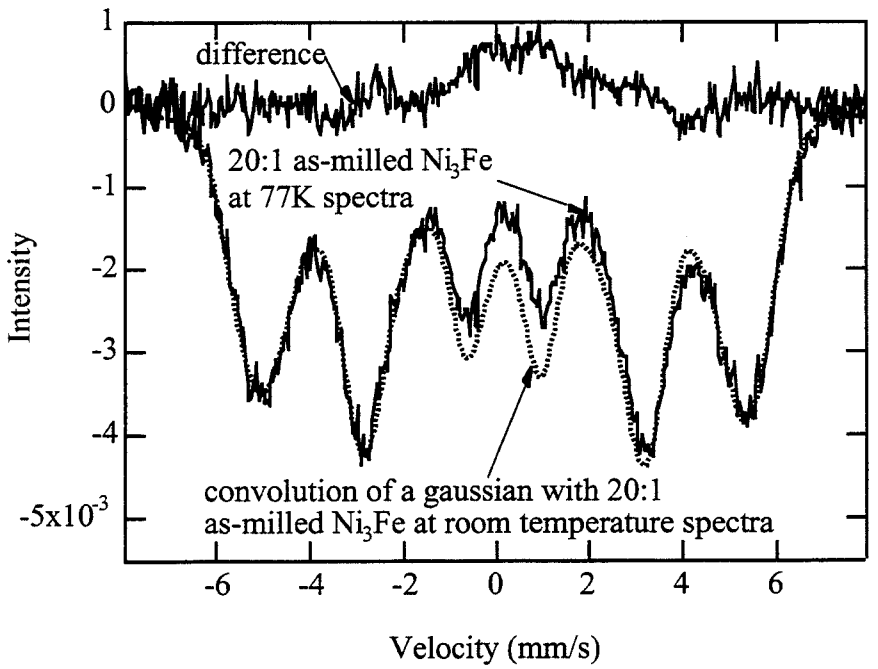

Figure 4.1. Mössbauer spectra of 20:1 as-milled powder acquired at and room temperature. The room temperature spectra was convoluted with a Gaussian. The difference between the two spectra is shown at the top.

The room temperature and 77K Mössbauer spectra are shown in Fig. 4.1. Because the evaporation of the liquid nitrogen in the cryostat causes vibrations, the line width of the 77 K spectra is larger than that of the room temperature spectra. Thus, the room temperature and 77 K spectra are not directly comparable. A Gaussian function was used to model the

effects of vibration. The Gaussian was convoluted with the room temperature spectrum. The half width of the Gaussian was so chosen that the resulting convolution matched well the outer peaks of the 77 K spectrum. Comparing the convoluted room temperature spectrum to the 77 K spectrum, we see that there is a paramagnetic component to the grain boundaries (Fig. 4.1). However, the paramagnetic contribution is only minor, showing that there is no significant paramagnetic component in the mechanically attrited Ni_3Fe samples.

4.4 Hyperfine Magnetic Field Distributions

Hyperfine field distributions derived from the room temperature spectra were used to calculate the grain boundary volume fractions and magnetic moments in various Ni_3Fe powders. Fig. 4.2 shows the Mössbauer spectra of 20:1 as-milled, 2:1 as-milled, and 2:1 annealed at 265°C and 600°C Ni_3Fe powders. Also indicated in Fig. 4.2 are the peaks coming from the Fe impurities present in the samples. These Fe impurities are from unincorporated ball fragments (Chapter 2), which chip off the ball during the milling process. These Fe-rich particles should contribute strongly to the spectrum. The disappearance of the Fe peaks with the increase in annealing temperature is caused by the bcc Fe being dissolved into the fcc Ni_3Fe.

To gain information about the grain boundaries from the HFD of the Ni_3Fe powders, it was first necessary to subtract the 330 kOe Fe peaks and then normalize the data. The resulting HFD's are shown in Fig. 4.3. The prominent peak for both the 2:1 600°C annealed and 5:1 600°C annealed samples is centered around 287 kOe. Because these are the control bulk samples, it is assumed that the 287 kOe peak present in all the HFD result from magnetic moments in the nanocrystals, whereas, the HFD below 242 kOe is associated with the grain boundaries. By calculating the area under the HFD curves

between 0 and 242 kOe, the grain boundary volume fractions were estimated for the various Ni_3Fe powders. These results are presented in Table 4.1. These evaluated volume fractions compare well to those assuming a hard sphere model of the nanocrystal with a grain boundary shell. If the nanocrystals have a radius of R and a grain boundary width of dr (0.5 nm for fcc materials)[55], then the grain boundary volume fraction is $\frac{3dr}{2R}$.

From the HFD curves below 242 kOe, it is also possible to observe changes in the magnetic moments of the grain boundaries. Fig. 4.3 shows that, upon low temperature

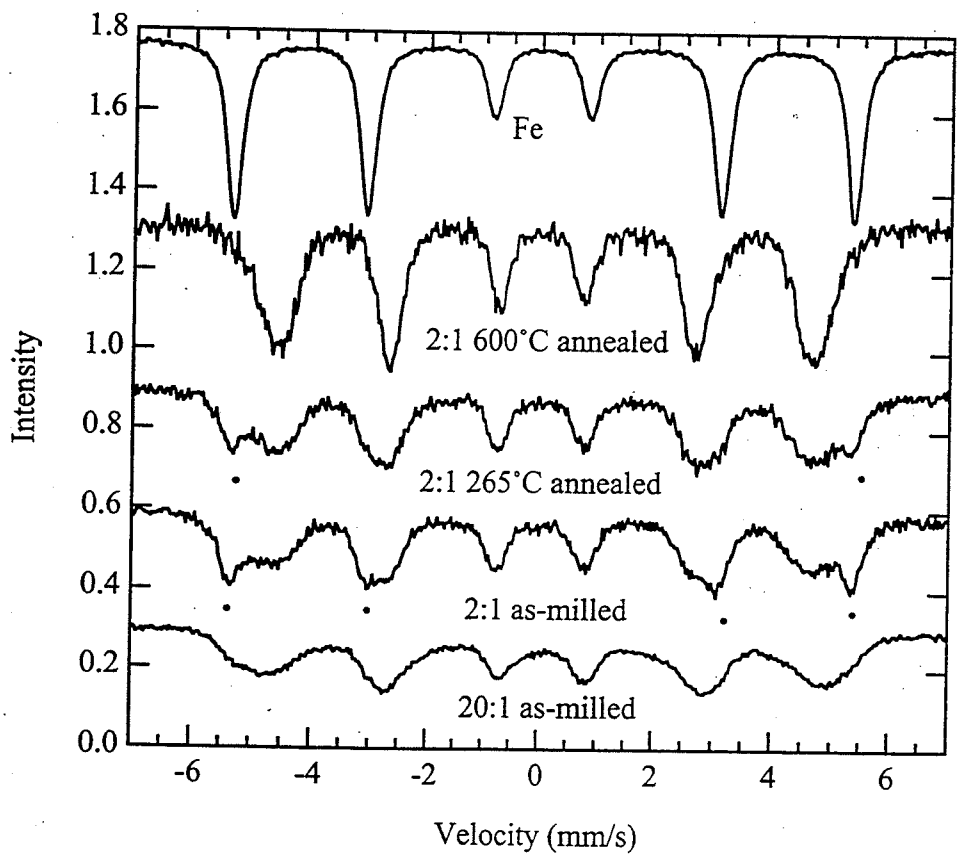

Figure 4.2. Room temperature Mössbauer spectra of Ni_3Fe samples with Fe peaks indicated.

annealing, there is a shift toward higher fields in both the 2:1 and 5:1 Ni_3Fe powders. This indicates an increase in the magnetic moments of the grain boundaries. By evaluating the weighted average of the hyperfine field in the grain boundaries, $\langle H_{gb} \rangle$, it is possible to estimate the grain boundaries' magnetic moment, since we know that the 287 peak corresponds to the magnetic moment of bulk disordered Ni_3Fe, 1.2 μ_B. Thus,

$$\mu_{\text{grain boundary}} = \frac{1.2\langle H_{gb} \rangle}{287} \mu_B \qquad (4.1)$$

The resulting $\mu_{\text{grain boundary}}$ are shown in Table 4.1.

The calculated $\mu_{\text{grain boundary}}$ are likely too large because the hyperfine magnetic field is not linearly related to the magnetic moment. Evidence of this can be seen through an attempt to calibrate the hyperfine magnetic field using known mean hyperfine fields and average magnetic moments as function of atomic % Fe in Ni. For fcc $Ni_{1-x}Fe_x$, where $0 \leq x \leq 0.45$, it has been shown that the mean hyperfine field, at room temperature, follows the linear relation[56]

$$\langle H \rangle = 261 \text{ kOe} + x*112 \text{ kOe}$$

while the magnetic moment is[57]

$$\mu = 0.6\mu_B + x*2.22$$

implying

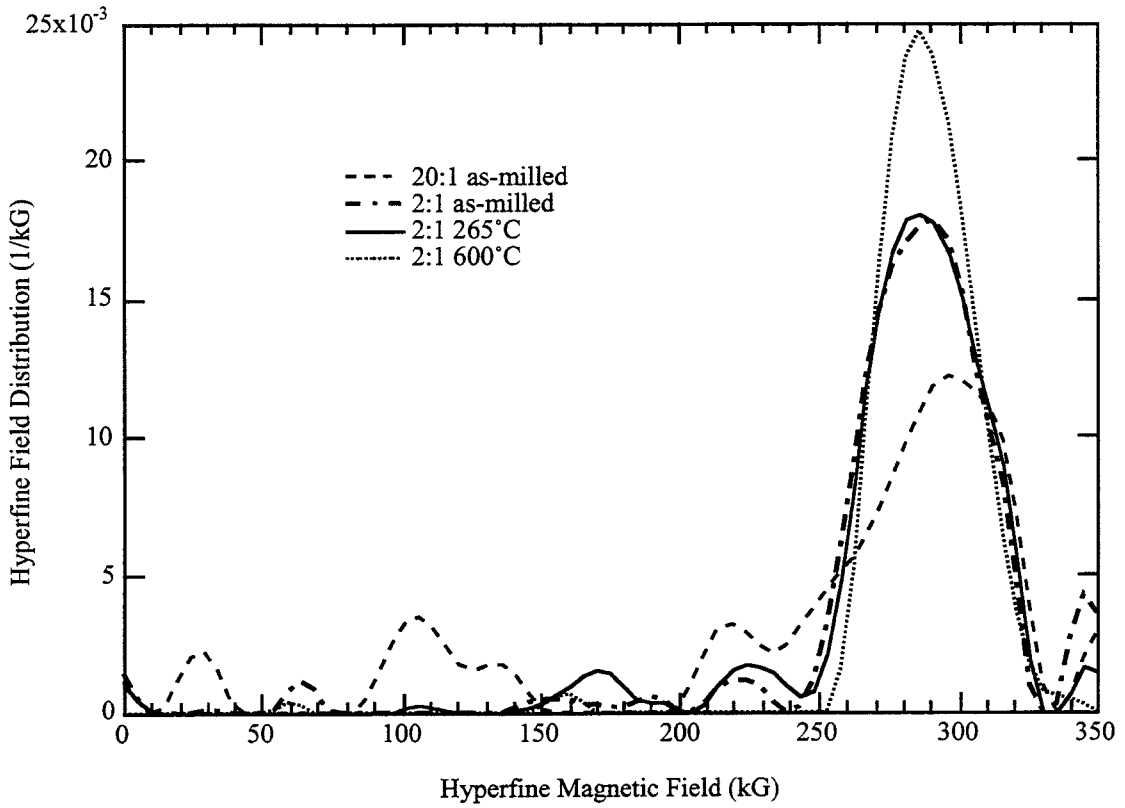

Figure 4.3. HFD with contribution from the Fe impurity removed and distribution renormalized.

$$\mu = 0.06\mu_B + 2.22\mu_B \frac{\langle H \rangle - 261\ \text{kOe}}{112\ \text{kOe}}$$

This relation is only valid for a small range of $\langle H \rangle$ ($261 \leq \langle H \rangle \leq 311$), but it spans a large range in μ ($0.6\mu_B \leq m \leq 1.6\ \mu_B$). Clearly the relation between μ and $\langle H \rangle$ cannot be linear and the values of μ calculated using Eq. 4.1 are too large. This means that there is even a greater difference between the magnetic moments of the grain boundaries and nanocrystals, along with a larger change in the average grain boundary magnetic moments upon annealing.

Sample	Volume Fraction	$V_f = \frac{3dr}{2R}$	Average Magnetic Moment (μ_B) Using Eq. 4.1
20:1 as-milled	0.28	0.25	0.6
2:1 as-milled	0.08	0.1	0.6
2:1, 265°C annealed	0.08	0.08	0.8

Table 4.1. Grain boundary volume fraction (the values of R were taken from Table 2.2) and average magnetic moment derived from Mössbauer spectra.

4.5 Conclusions

Mössbauer spectra were used to study the magnetic moments of and paramagnetism in the grain boundaries of mechanically attrited Ni_3Fe nanocrystals. By comparing spectra of 20:1 as-milled powder taken at room temperature and at 77 K, it was seen that there was some of paramagnetism at room temperature. Spectra of various nanocrystalline powders taken at room temperature showed that the average magnetic moments of the grain boundaries were smaller than those for atoms in the nanocrystals. The average magnetic moments of the ^{57}Fe atoms at the grain boundaries increased upon annealing, indicating that the grain boundary magnetic moments are responsive to disorder and defects present in the grain boundaries. Because the grain boundaries are 10 - 20 vol.% of the Ni_3Fe powder volume, the magnetic characteristics and changes of the grain boundaries should affect the bulk magnetic properties of the powder.

Chapter 5

Magnetization Curves of Ni_3Fe Nanocrystals

Magnetization curves were measured for Ni_3Fe nanocrystals with various grain sizes and internal strains. Measurements were performed on samples prepared of both as loose powder and as compressed pellets. From the M-H magnetization curves, the coercivity, the maximum permeability, and the saturation magnetization were all derived. Differences in these quantities between samples were related to changes in grain size, internal strain, and electrical resistivity, which was measured on samples prepared as pellets.

5.1 Introduction

A common technique for characterizing ferromagnetic materials is to observe how the material behaves in a magnetic field. To do this, the material is moved in a magnetic field and the induced voltage in an adjacent coil is plotted against the magnetizing field, H. From the resulting magnetization curve, magnetic properties of the material can be derived. Fig. 5.1 shows a typical magnetization curve.

Initially, with an unmagnetized sample, the curve will start at the origin of M, magnetization, versus H[33,57,58]. For a bulk magnetic material consisting of domains and domain walls, the initial upwardly concave part of the virgin magnetization curve consists of reversible displacements of domain walls. The next stage of magnetization, which happens over the steepest section of the virgin magnetization curve, involves the irreversible displacement of domain walls. Because this is an irreversible process, if the

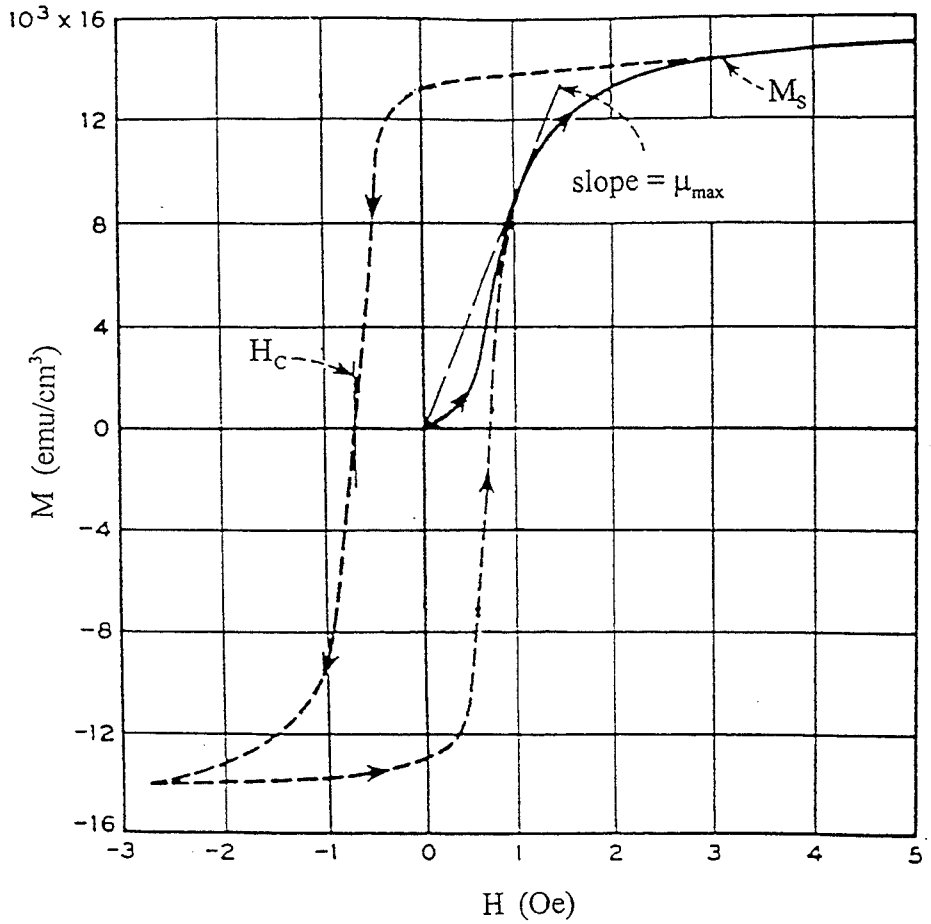

Figure 5.1. Typical magnetization curve showing H_C, M_S, and μ_{max} (after a figure by Bozorth[57]).

magnetizing field is lowered after entering this stage of magnetization, the curve does not retrace itself. Instead, the magnetization decreases at a slower rate with a remanence, M_r, remaining at H = 0. Similarly, as the magnetizing field is reduced further, the magnetization curve crosses the M = 0 axis at $H = H_c$ (H_c is known as the coercive field or coercivity). Thus, the M-H magnetization curve has hysteresis. The third stage of magnetization is a reversible process involving the rotation of atomic spins until saturation magnetization, M_s, is attained. Other magnetic quantities that can be derived from the

magnetization curve are the maximum susceptibility, $\chi_{max} = (M/H)_{max}$, and the maximum permeability, $\mu_{max} = 1 + \chi_{max}$.

The magnetization process described above is not applicable to individual Ni_3Fe nanocrystals studied because they cannot contain domain walls. As the domain walls in the bulk material are on the order of 50 nm, it is not physically possible for the Ni_3Fe nanocrystals, which range from 5 to 20 nm, to contain domain walls. The "random anisotropy model"[32] explains, at least in part, the magnetic properties of nanocrystals. This model predicts that the exchange interaction, A, will dominate the magnetocrystalline anisotropy, K_1, for materials having grain sizes smaller than $L_{ex} = (A/K_1)^{1/2}$, the ferromagnetic exchange length (typically tens of nanometers). In essence, when a polycrystalline grain size is smaller than the width of a magnetic domain wall, there will be little tendency for crystalline orientations to affect the energy of magnetic orientation in the material. One result of this model is that the coercive field, H_c, will be small.

5.2 Electrical Resistivity Measurements

Electrical resistivity measurements were made on pellets pressed from the Ni_3Fe powders. It is impractical to measure the resistance of loose powders. The measured resistivities therefore do not correspond directly to resistivities of samples in powder form. Nevertheless, we do expect the resistivities of nanocrystalline samples with different grain sizes to correspond comparatively whether in powder or pellet form. Pellets 0.25-in. in diameter and weighing 0.2 g were formed in a hardened steel die and compressed to

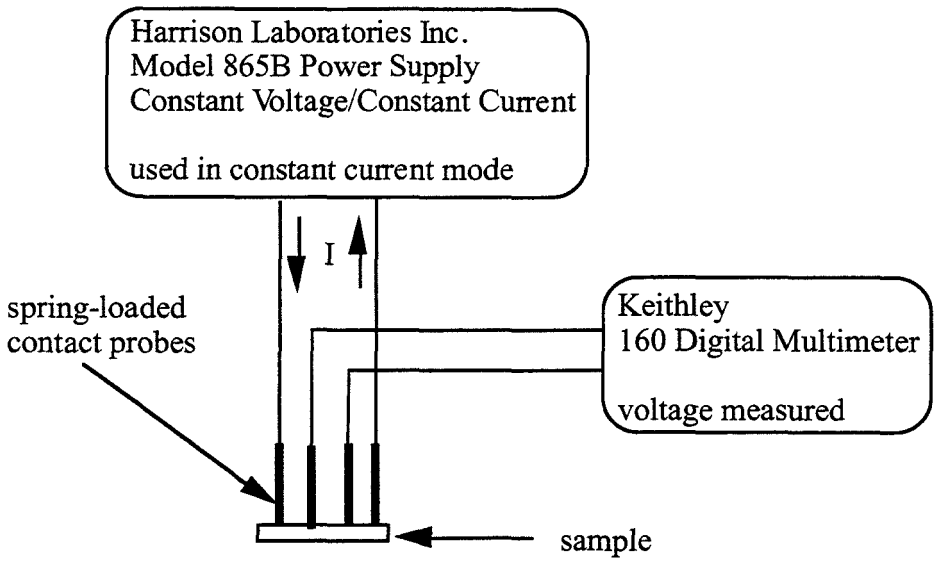

Figure 5.2. Schematic diagram of resistivity instrumentation.

40,000 lb/in^2. The powders were compacted in their as-prepared state and were given no subsequent annealing.

Fig. 5.2 shows the system used to measure the resistivity. Spring-loaded contact probes were used to make electrical contact with the sample. Using the outer two probes, a constant current (~0.4 A) was sent through the sample. The voltage drop across the two inner contacts was then measured. The resistivity, ρ, was calculated using

$$\rho = \frac{VA}{I\ell}$$

where V is the voltage drop across the two inner contacts, A is the cross-sectional area through which the current travels, I is the current, and ℓ is the distance between the inner probes, 1.3 mm. A is determined by the sample contact connection (Fig. 5.3) and equals

the width of the probe, 0.5 mm, times the height of the sample. The results of the resistivity measurements are presented in Table 5.1. Fig. 5.4 shows that there is a linear relationship between resistivity and inverse grain size. This indicates that the resistivity of the nanocrystalline samples is related to the grain boundary volume fractions.

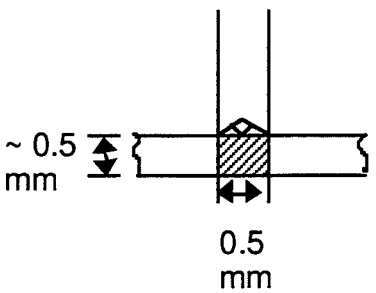

Figure 5.3. Spring-loaded contact probe and sample connection with the area, A, cross hatched.

Sample	Resistivity (Ω cm) x10^{-4}
20:1 as-milled	11.29
5:1 as-milled	6.44
5:1 annealed at 265°C	4.81
5:1 annealed at 425°C	2.14
5:1 annealed at 600°C	1.73

Table 5.1. Resistivity of nanocrystalline Ni_3Fe pellet samples.

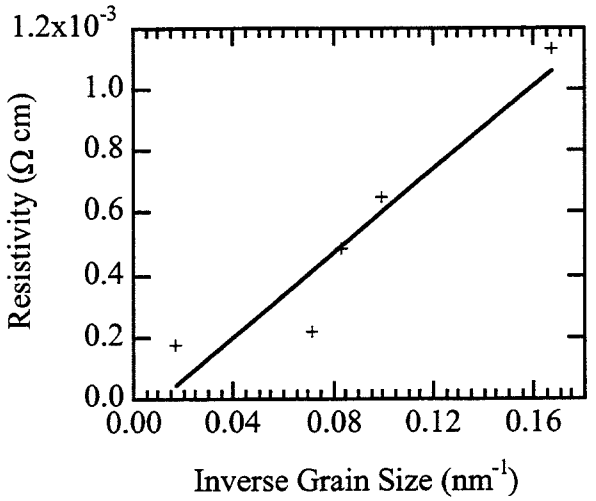

Figure 5.4. Resistance versus inverse grain size along with a linear fit of the data.

5.3 Magnetic Characteristics

The nanocrystalline Ni_3Fe samples studied were 20:1 as-milled, 5:1 as-milled, and 5:1 powder annealed at 265°C, 425°C, and 600°C. Measurements were made on both the loose powders and powders that were pressed into 0.25-in. diameter pellets. The magnetization curves were measured by R. D. Shull at the National Institute of Standards and Technology, using a vibration sample magnetometer. In this technique, the sample is vibrated up and down between two sets of coils on the magnet pole pieces. The moving sample is like a moving magnetic field which then induces an oscillating potential in the coils. The magnitude of this oscillating potential, which is in phase with the oscillating sample, is proportional to the magnetization of the sample. The magnetization hysteresis loop was then measured as the externally applied field was varied in a cycle. Full

hysteresis loops for all the samples were measured at room temperature and analyzed for the coercivity, maximum permeability, and magnetic saturation.

Fig. 5.5 shows the magnetization curve of the 20:1 powder sample. Its basic shape is typical of all the Ni_3Fe samples. It has a saturation magnetization about 900 emu/cm^3 and is essentially saturated at an applied field of 5 kOe. Its hysteresis loop is very thin, implying a low coercivity. The hysteresis loop is so thin that the presence of the hysteresis is not observable until the loop is magnified considerably about H = 0 (Fig. 5.6). From Fig. 5.6, it is evident from the slopes of the hysteresis loops and their intersection with the axes that the processing of the powder into pellets affects the magnetic properties. This could be caused by the introduction of strain during the pellet-making process. From the hysteresis loops, it was possible to derive H_c, μ_{max}, and M_s. The results as a function of grain size are shown in Fig. 5.7. During data analysis, H_c and μ_{max} were also plotted as a function of RMS strain (Fig. 5.8); however, no trends could be discerned from these plots. This is probably because the H_c and μ_{max} are related to a complex combination of effects from strain, grain size, and resistivity effects.

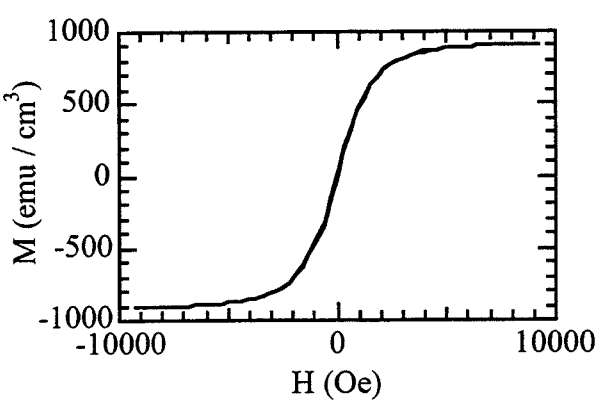

Figure 5.5. Magnetization curve of 20:1 as-milled Ni_3Fe powder.

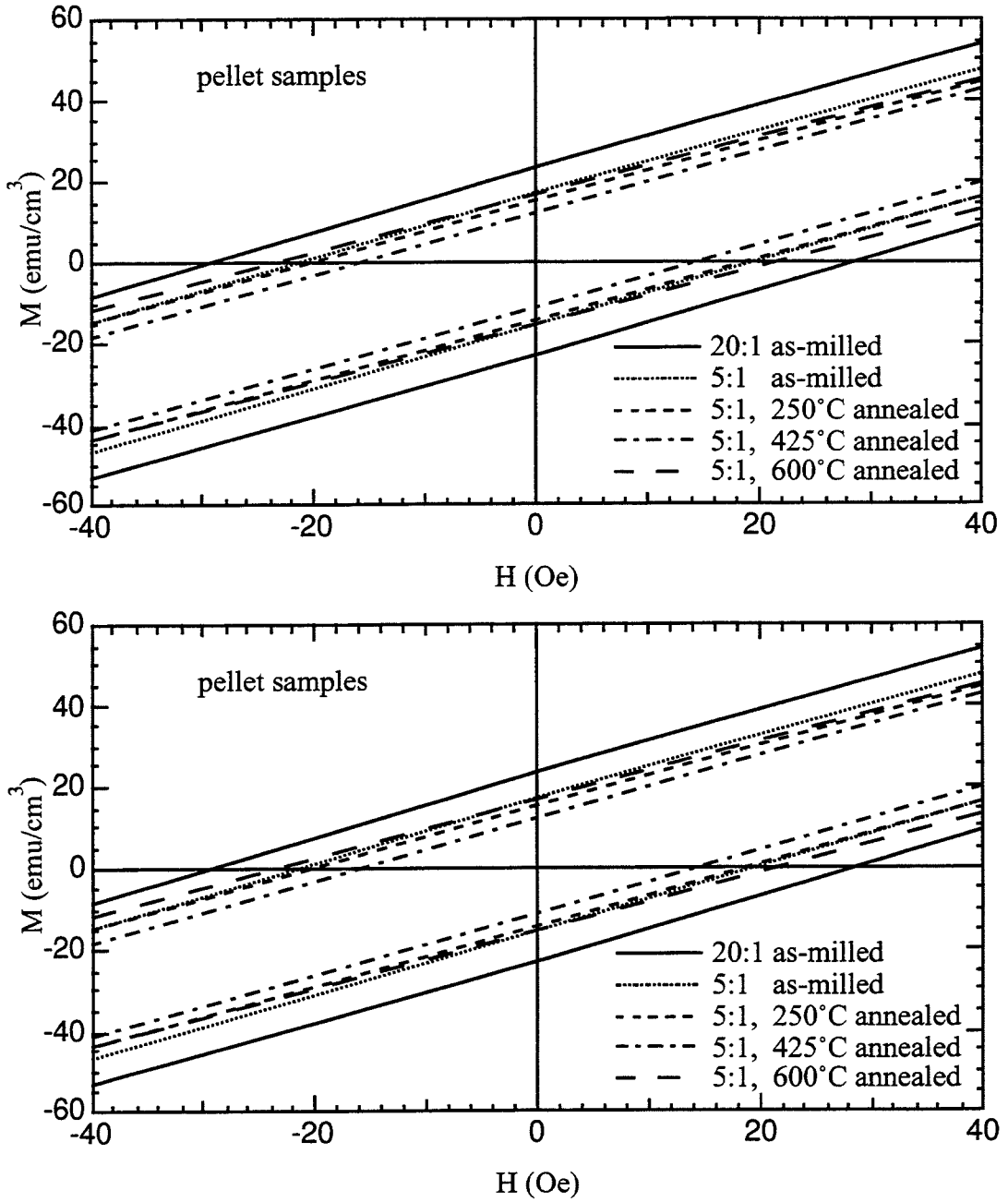

Figure 5.6. Expanded low-field region of hysteresis loops of (a) pellet and (b) powder samples.

Fig. 5.7 shows that the μ_{max} depends inversely on grain size. The figure also shows an enhancement of μ_{max} for the pellet sample. The enhancement appears to be almost a constant offset of 30 emu/cm^{3}Oe. Internal stress is known to affect the magnetic permeability and coercivity of materials[33]. Thus, the enhancement of μ_{max} probably originates from the introduction of internal stresses when the powders were compressed into pellets. This enhancement would be expected to be largest for the large-grained material annealed at 600°C because it is the material most likely to develop dislocations within its crystallites. This is because the smaller grained nanocrystalline powder has crystals too small to contain dislocations. In summary, the graph implies that smaller grain sizes and larger strains lead to an increase in μ_{max}. Fig. 5.8, which has a plot of μ_{max} versus RMS strain, shows no obvious correlation between μ_{max} and strain. The contradiction about the effects of strain on μ_{max} between the two figures can be resolved by recognizing the μ_{max} is probably affected by other characteristics of the nanocrystalline samples.

From Fig. 5.7, it is shown that H_c is also inversely affected by grain size. This trend is most evident in the powder curve, but can also be seen in the pellet curve. The curves do not, however, show the obvious correlation between strain and H_c that was seen in the μ_{max} curves (Figs. 5.7 and 5.8). The first two points in both the powder and pellet curves represent the coercivity for the 20:1 and 5:1 as-milled samples, respectively. The 20:1 powder sample has essentially no internal strain whereas the compressed pellet has an RMS strain of 0.0035, which was determined by analyzing x-ray diffraction patterns. For all the samples, this is the largest RMS strain increase between the powder and pellet form. H_c for the 20:1 as-milled pellet and powder samples are equivalent. Similarly, the H_c for the

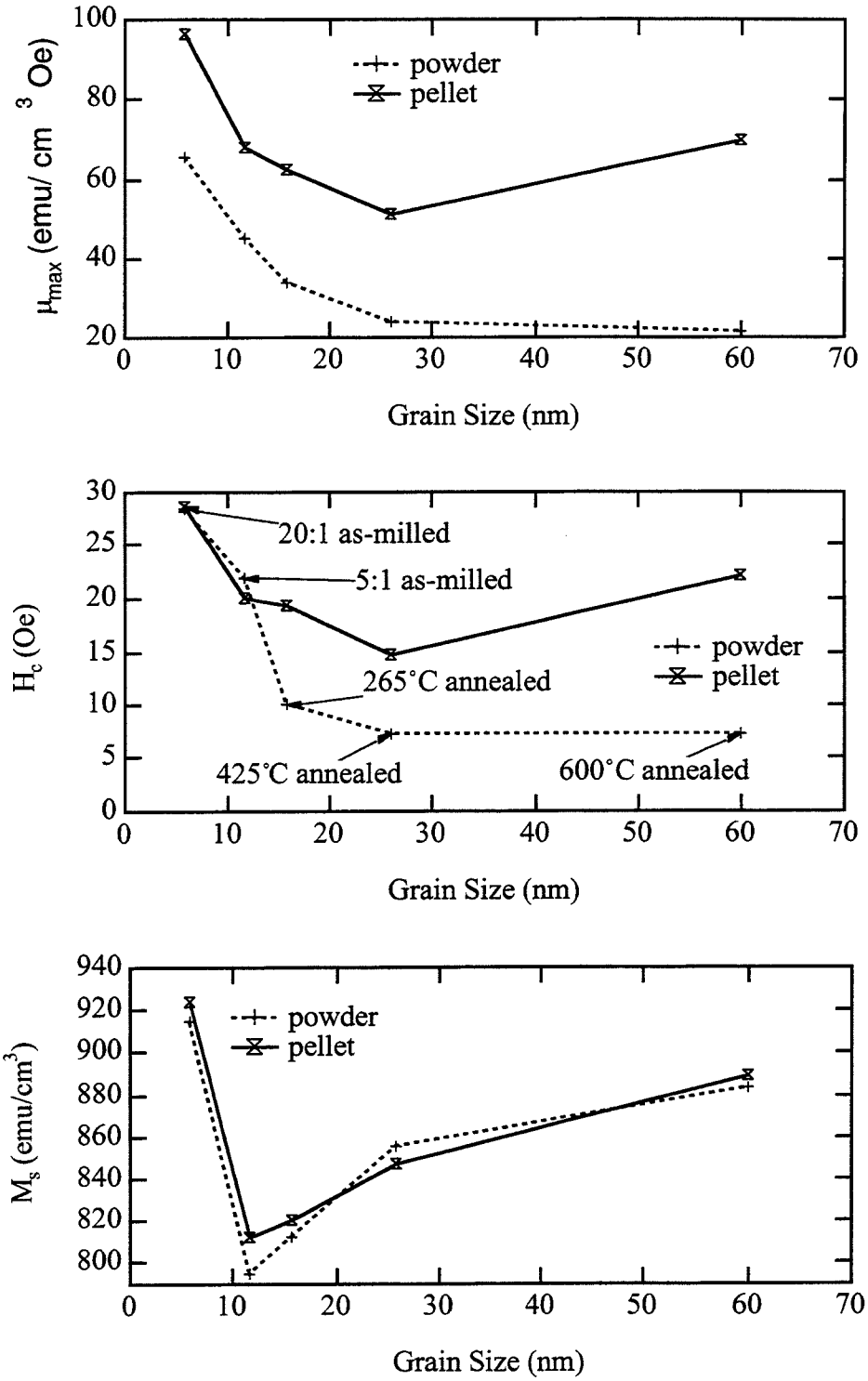

Figure 5.7. μ_m., H_c, and M_s versus grain size for pellet and powder samples.

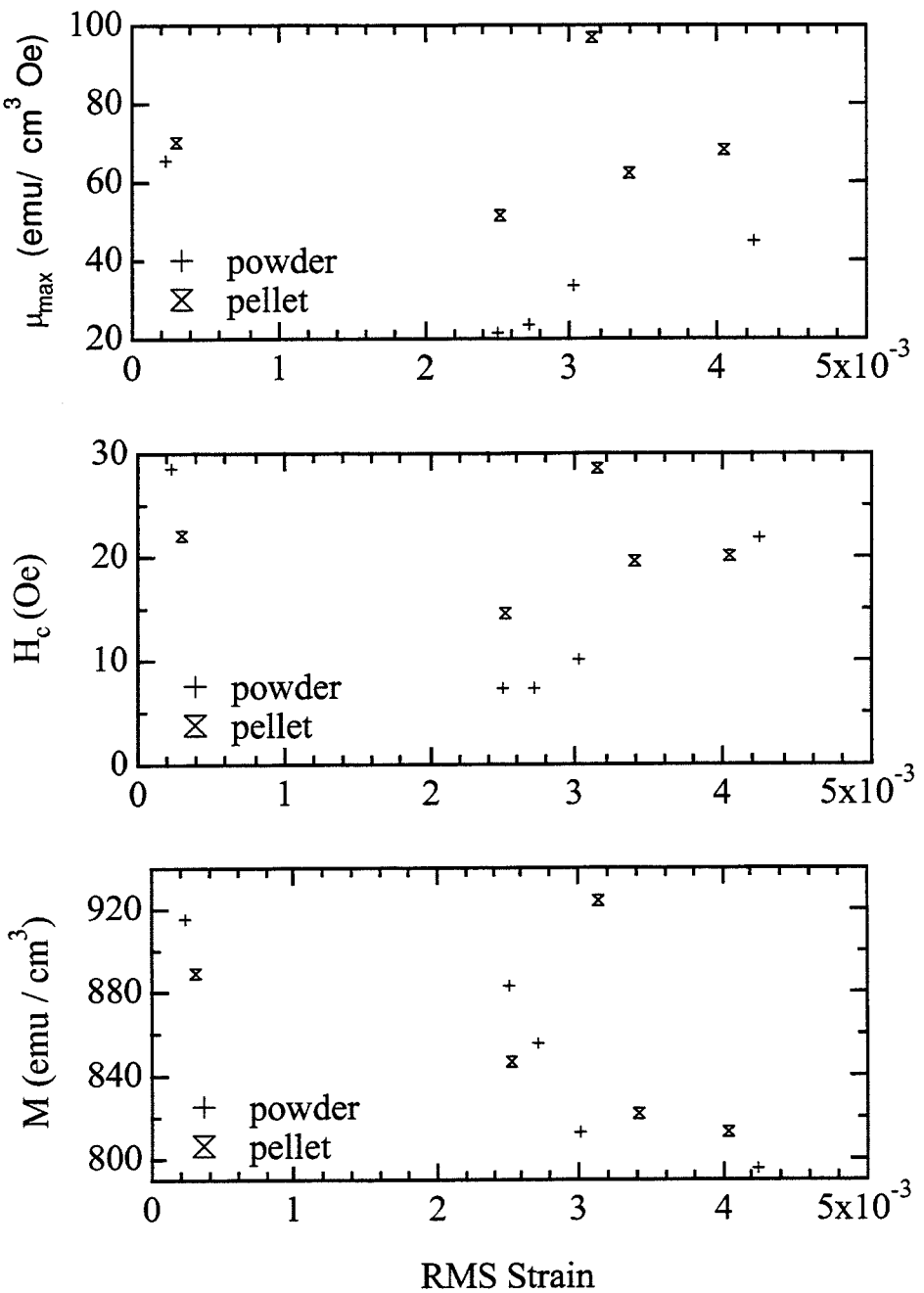

Figure 5.8. μ_m., H_c, and M_s versus RMS strain from pellet and powder samples.

5:1 as-milled samples changes little upon compression into a pellet. At the very least, this implies that internal strain has a negligible effect on the coercivity of small grain, 6- to 12-nm, nanocrystals. Because it is known that strain can affect the coercivity of materials, it is still possible that the coercivity of the larger grained samples is affected by the increased strain.

The M_s versus grain size curves for the powder and pellet samples are essentially the same (Fig. 5.7), implying that the M_s is not affected strongly by strain (Fig. 5.8) incorporated during pellet pressing. There appears to be some correlation between grain size and M_s. For the 5:1 as-milled and annealed samples, M_S increases with grain size. This trend does not, however, include the 20:1 as-milled sample (the left most point in Fig. 5.7), which has both the largest M_S and the smallest grain size. The erratic behavior of M_S indicates the distribution of magnetic moments' magnitudes (M_S is proportional to the average magnetic moment) in the mechanically attrited nanocrystalline powder is complicated.

Mössbauer spectra of the powders (Chapter 4) showed that the grain boundaries of the nanocrystalline samples had magnetic moments that were less than the nanocrystals. The spectra also showed that the grain boundary magnetic moments increased upon annealing at 265°C, indicating that they were affected strongly by the internal structures of the grain boundaries. Because the grain boundary magnetic moments increase upon annealing, it is expected that M_S would increase with grain size for the 5:1 powders that were annealed. Apart from changes in grain boundary magnetic moments, we would also expect M_S to increase with grain size since the grain boundary volume fraction is reducing and the magnetic moments of the grain boundaries are less than those of the nanocrystals.

I believe that 20:1 as-milled powder behaves differently magnetically because it is so different physically from the other samples. X-ray diffraction patterns (Chapter 2) showed that it had a grain size of 6 nm (much smaller than the 10-nm 5:1 as-milled powder) and no measurable strain. Due to thier size difference the 20:1 as-milled nanocrystals have a grain

boundary volume fraction 2 times larger than the 5:1 as-milled sample (the grain boudnary volume fractions can be calculated as discribed in Section 4.4). In summary, the 20:1 as-milled powder has a large grain boundary volume fraction, negligible strain, and a different magnetic moment in its crystals, all of which are likely to effect the magnetic saturation of the sample. It may not be reasonable to expect the trends of the 5:1 as-milled and annealed samples to be revelent to the 20:1 as-milled sample.

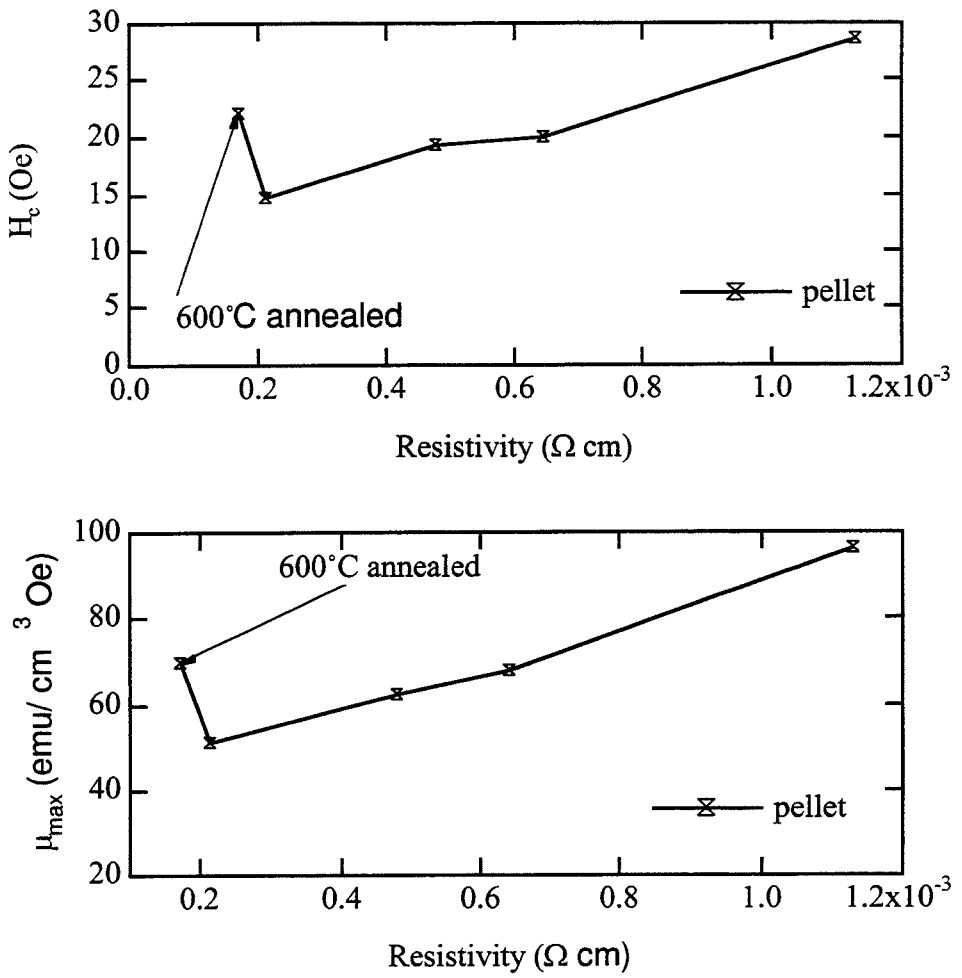

Figure 5.9. a) H_c vs. resistivity, b) μ_{max} vs. resistivity for pellet samples.

Resistivity is another quantity that could correlate to the magnetic properties of nanocrystals. Fig. 5.9 displays both H_c and μ_{max} as a function of resistivity for the pellet samples. (The resistivity of the loose powders was not measured.) For the nanocrystalline pellet samples, the resistivity correlates well to both H_c and μ_{max}. The 600°C annealed sample does not follow this trend. This is evidence that nanocrystals have intrinsically different magnetic behavior than do bulk crystals, perhaps due to the generation of dislocations in these materials during compression into pellets.

5.4 Conclusions

Magnetic properties of Ni_3Fe nanocrystals are affected by grain size, strain, and resisitivity. For both the powder and pellet nanocrystalline samples, H_c and μ_{max} decrease with grain size, whereas they generally increase directly with electrical resistivity. The maximum permeability μ_{max} correlates weakly with RMS strain, but such a correlation is not found for the H_c for the sample studied. The strong correlation between H_c and μ_{max} on the resistivity and strain also implies that the interconnections between nanocrystals, and their ability to interact with each other, significantly affect their macroscopic properties. Barriers to nanocrystal interaction could come from internal strain, disordered grain boundaries, or other crystal defects. The magnetic saturation was shown to be complex and in need of more study before its behavior can be predicted.

Chapter 6

Cavity Perturbation Measurements

The phonon density of states of nanocrystalline Ni_3Fe showed an enhancement at low energies, <10 meV, compared to bulk Ni_3Fe (Chapter 3). This enhancement in vibrational modes may cause the nanocrystalline Ni_3Fe to be more absorptive than is bulk Ni_3Fe to high frequency electromagnetic waves. If the material is more absorptive at GHz frequencies, evidence of this would be seen in its magnetic permeability or electrical permitivity. A rough generalization is that the imaginary component of the permeability or permitivity relates to a material's tendency to absorb electromagnetic waves.

The magnetic permeability at 8.9 GHz of Ni_3Fe nanocrystalline powders was determined using cavity perturbation[59,60]. This technique involves measuring the resonant frequencies and quality factors of a cavity with and without the test sample inside the cavity. To determine the quality factor and resonance frequency, the power coupled to the cavity is swept over a range of frequencies so that an isolated resonance mode is centered in the frequency range. The transmitted power is then fitted to a Lorentzian function, from which the quality factor and resonance frequency are calculated. The quality factors and resonance frequencies are then used with perturbation calculations specific to the cavity, resonance mode, sample position, and sample shape to determine the complex permeability of the sample.

6.1 Application of Perturbation Theory

The proper selection of a resonance mode is crucial for the application of perturbation theory to determine the permeability,. For permeability measurements, it is necessary that the E field at the samples be zero and that both the E and H fields change slowly in the region of the sample. Another constraint is that a nondegenerate mode needs to be excited. This is typically done by selecting a low order mode, because at lower frequencies the modes are better separated (Fig. 6.1). In the present experiment, degeneracy was avoided by the positioning of the excitation and transmission antennae.

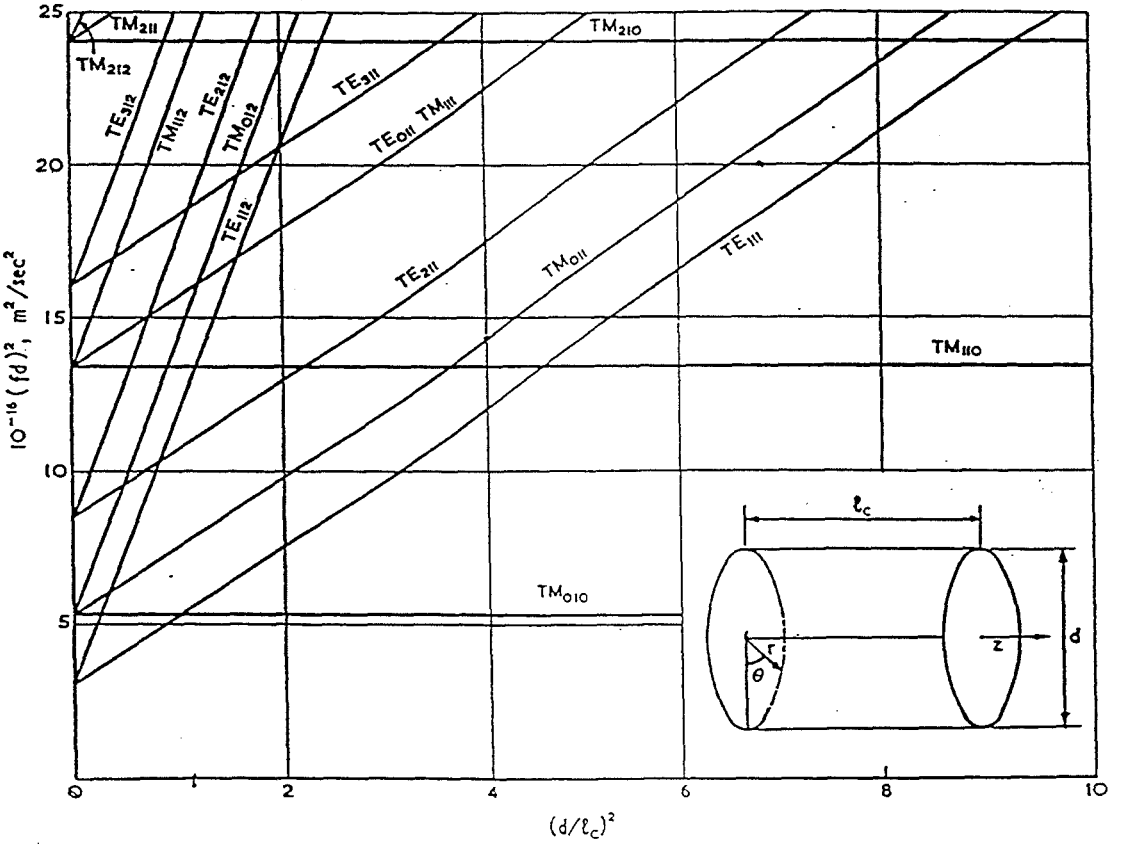

Figure 6.1. Resonant mode chart for a right circular cylindrical cavity.[61]

For the experiment, the sample was placed in the center of a circular cylindrical cavity. The lowest order mode that satisfied the H and E field requirements was TE011. For an empty cylindrical cavity, the field equations for the TE011 mode are

$$
\begin{aligned}
E_{oz} &= E_{o\rho} = 0 \\
E_{o\theta} &= i\sqrt{\frac{\mu_o}{\varepsilon_o}} J_o'(k_1\rho)\sin(k_3 z) \\
H_{o\theta} &= 0 \\
H_{oz} &= \frac{k_1}{k} J_o(k_1\rho)\sin(k_3 z) \\
H_{o\rho} &= \frac{k_1}{k_3} J_o'(k_1\rho)\cos(k_3 z)
\end{aligned}
\qquad (6.1)
$$

where: ρ, θ, and z are the coordinates inside the cavity, μ_o is the permeability of free space, ε_o is the permitivity of free space, J_o is a zero order Bessel function, and k_1, k_3, and k are related to the cavity size and modes. The k values, along with the electric and magnetic fields, are derived by using Maxwell's equations. The formula describing the modes for rectangular and cylindrical cavities can be found in Waldron[62]. For the cylindrical cavity used, $k_1 = 1.63086$, $k_2 = 0.916183$, and $k = 1.87059$.

From Eq. 6.1, it was easily determined that the E field was zero at the center of the cavity. Using Mathematica to graph the H and E fields, it was determined that the H and E fields at the cavity center changed slowly. Thus, the requirements on E and H were satisfied with the TE011 mode.

The TE011 mode is degenerate with the TM111 mode (Fig. 6.1). Excitation of the TM111 mode is avoided by the positioning of the antennae. The antennae consist of wire loops that couple to the magnetic field of the mode. The excitation antenna couples to a mode when an oscillating current at the resonance frequency is sent through the antenna's loop creating a magnetic field perpendicular to the loop. To excite the TE011 mode, the antenna is coupled to the H_z field by positioning the antenna loop so that it is parallel to the bottom of the cavity. This prevents the excitation of the TM111 mode because it has no H_z field. Similarly, the transmission antenna is placed parallel to the cavity bottom so that it is coupled only to the TE011 mode.

The perturbation calculation used the assumption that the sample in the cavity only perturbs the fields inside the cavity by a small amount compared to the field in an empty cavity, or equivalently that the sample changes the resonant frequency of the cavity by a small amount. Specifically for disks, the formula is only valid if the disk is thin relative to its diameter. The derivation of the perturbation formula is shown in detail in Waldron[60,62]. The derivation involves relating the energy density in the empty cavity and the amount that the sample perturbs this energy density to changes in the resonance frequency and quality factor of the cavity upon insertion of the sample:

$$\frac{\Omega_o - \Omega}{\omega_o} = \frac{\int_{V_S} \left[\left(E_1 \cdot D_o - E_o \cdot D_1 \right) - \left(H_1 \cdot B_o - H_o \cdot B_1 \right) \right] dV_S}{\int_{V_o} \left[E_o \cdot D_o - H_o \cdot B_o \right] dV} = \frac{W_S}{W_o} \qquad (6.2)$$

where: E_o, B_o, D_o, and H_o are the electric field, the magnetic induction, the electric displacement and the magnetic field in the empty cavity while E_1, B_1, D_1, and H_1 are the perturbed fields in the sample loaded cavity, and Ω_o and Ω are respectively the complex resonance frEquencies of the unperturbed and perturbed cavity, so that

$$\Omega_o = \omega_o\left(1+\frac{i}{2Q_o}\right)$$

$$\Omega = \omega\left(1+\frac{i}{2Q}\right) \tag{6.3}$$

Respectively, ω_o and ω are the resonance frequency, and Q_o and Q are the quality factor of the unperturbed and perturbed cavity. In the unperturbed state, the electric and magnetic field in the cavity are

$$\begin{aligned} E &= E_o e^{i\omega_o t} \\ H &= H_o e^{i\omega_o t} \end{aligned} \tag{6.4}$$

The perturbed fields caused by the addition of the sample are

$$\begin{aligned} H_S &= \left(H_o + H_1\right) e^{i\omega t} \\ E_S &= \left(E_o + E_1\right) e^{i\omega t} \end{aligned} \tag{6.5}$$

For the TE011 cylindrical cavity mode, the empty cavity electric and magnetic fields are those given in Eq. 6.1.

First we will evaluate W_S, for which the energy density is evaluated over the volume of the sample. Because the sample is positioned at the center of the cavity, all electric and magnetic fields except H_z equal zero, reducing W_S to

$$W_S = -\int_{V_S}\left[H_{z1}\cdot B_{zo} - H_{zo}\cdot B_{z1}\right]dV_S \tag{6.6}$$

Assuming that the sample is magnetically isotropic,

$$B_{z1} = \mu_o[\mu(H_{zo} + H_{zS}) - H_{zo}] \tag{6.7}$$

where $\mu = \mu' - i\mu''$. Combining Eqs. 6.5 and 6.7,

$$B_{z1} = \mu_o[\mu(2H_{zo} + H_{z1}) - H_{zo}] \tag{6.8}$$

From boundary conditions

$$B_{zS} = B_{zo}, \tag{6.9}$$

i.e., B_z is not changed by the sample. Inside the sample

$$B_{zo} = \mu_o H_{zo} \tag{6.10}$$

Combining Eqs. 6.6, 6.8, and 6.10,

$$W_S = \int_{V_S}[H_{zo} \cdot H_{zo}(2\mu_o\mu - \mu_o)]dV_S$$

$$\frac{(\omega_o - \omega) + i\omega_o\left(\frac{1}{2Q} - \frac{1}{2Q_o}\right)}{\omega_o} = \frac{\mu_o(2\mu - 1)\int_{V_S} H_{zo}^2 dV_S}{\int_{V_o}[E_o \cdot D_o - H_o \cdot B_o]dV} \tag{6.11}$$

This equation was then integrated using Mathematica and constants derived from the cavity dimensions. Using Mathematica, μ' and μ'' were solved for in terms of ω_o, ω, Q_o, and Q, and L, the sample height.

$$\mu' = \frac{86.94(0.005751LQ_oQ\omega_o - Q_oQ(\omega - \omega_o) + 0.00628Q_oQ\omega_o \sin(0.91618L))}{Q_oQ\omega_o(L + 1.09148458 \sin(0.91618L))}$$

$$\mu'' = \frac{86.94(-0.5Q_o\omega_o + 0.5Q\omega_o)}{Q_oQ\omega_o(L + 1.09148458 \sin(0.91618L))} \qquad (6.12)$$

6.2 Experiment

A schematic diagram of the instrumentation is shown in Fig. 6.2. The frequency sweep from the sweep generator is amplified and then used to excite the cavity via the excitation antenna. The transmission antenna responds to the cavity's change in power as a function of frequency and the diode connected to it converts the power into a voltage. The signal from the diode is connected to an oscilloscope which is triggered by the signal from the sweep generator. Displayed on the oscilloscope is the Lorentzian shaped voltage curve as a function of frequency. The oscilloscope image is then captured, converted from voltage to power, and fit to a Lorentzian function.

To convert the voltage signal into power, it is necessary to calibrate the diode. A schematic diagram of the apparatus for diode calibration is shown in Fig. 6.3. An amplified constant frequency (ω = 8.9 GHz) is divided in half by a power splitter. One

half of the power is measured by a power meter while the other half goes to the diode and then is measured by a voltmeter. The resulting power versus voltage curve is then fit to a quadratic equation that is used to convert the captured voltage curves into frequency (Fig. 6.4).

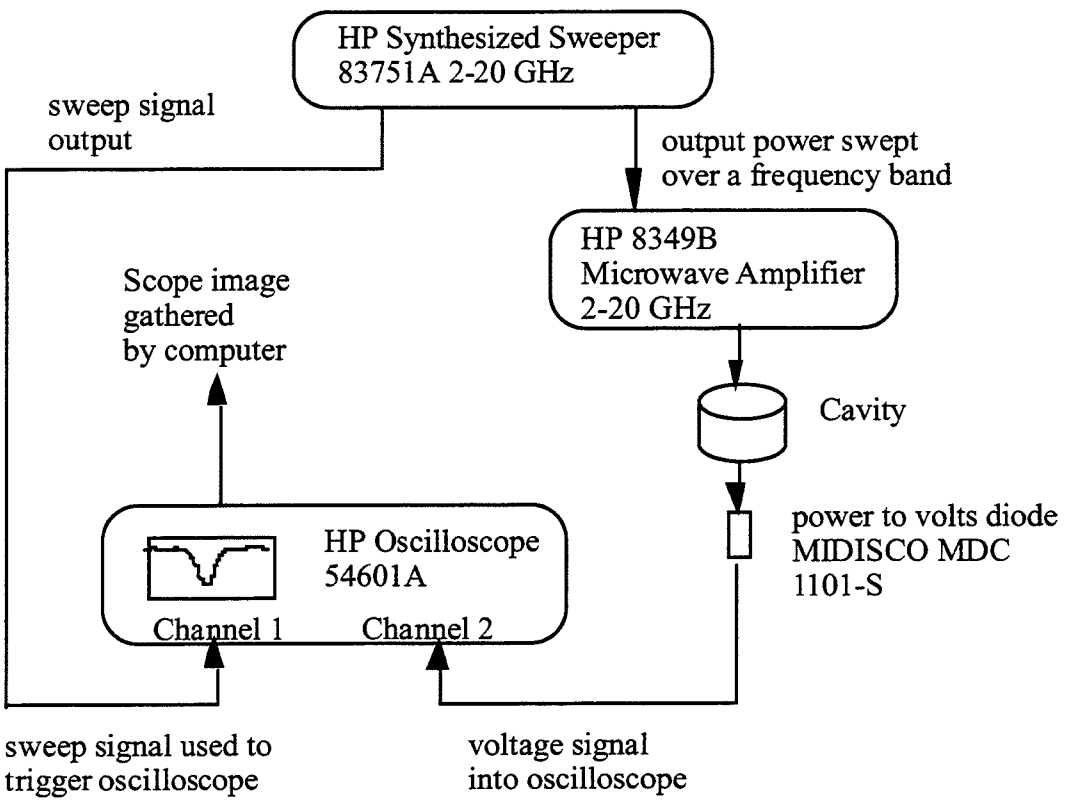

Figure 6.2. Schematic diagram of instrumentation to microwave cavity perturbation measurements.

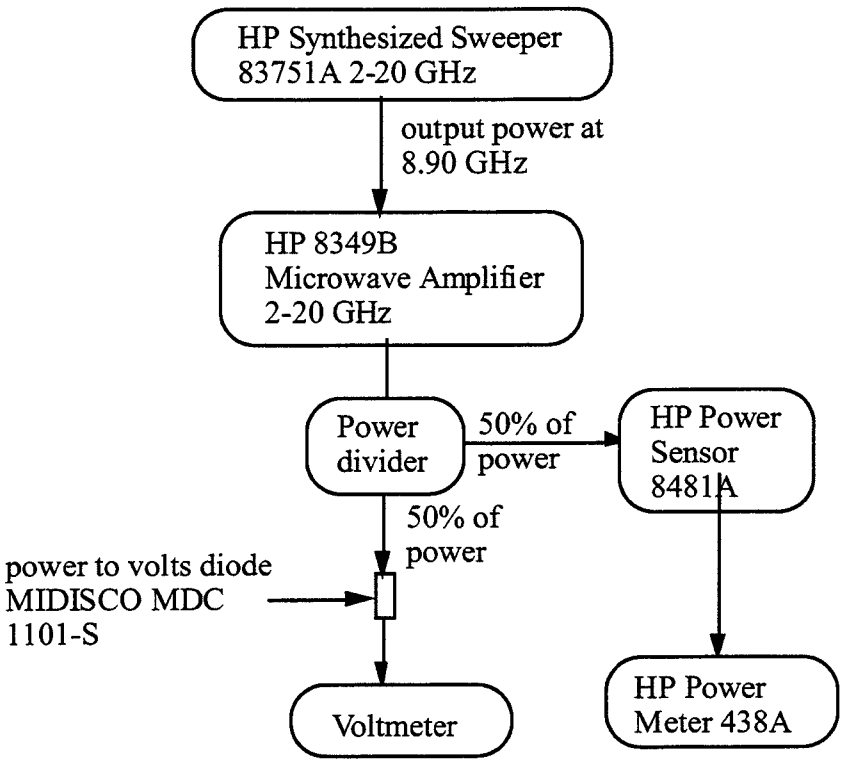

Figure 6.3. Schematic diagram of calibration instrumentation.

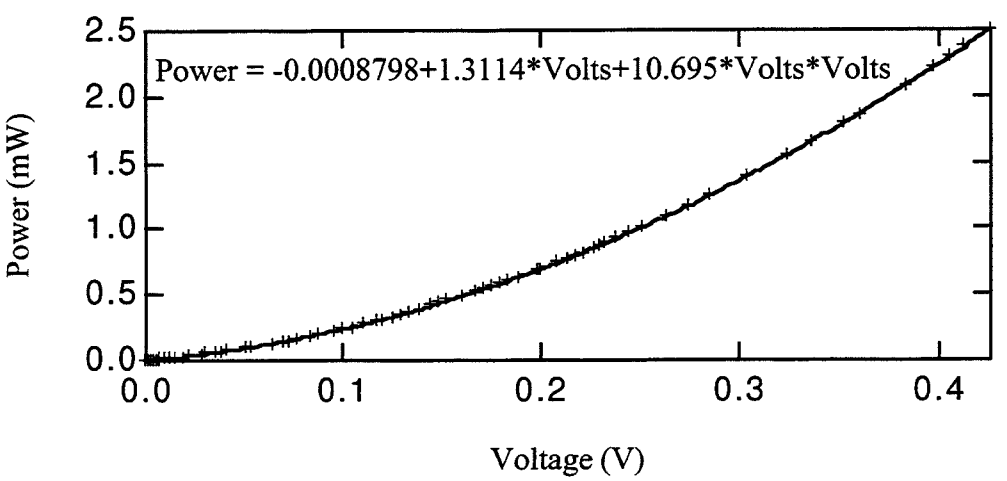

Figure 6.4. Calibration curve.

Both the quality factor, Q, and the resonance frequency, ω_r, are related to the measured Lorentzian shaped power curve as a function of frequency, $P(\omega)$, by

$$P(\omega) = A + B\omega + \frac{C}{\left((\omega - \omega_r)^2 + \left(\frac{\omega_r}{2Q}\right)\right)} \qquad (13)$$

where $A + B\omega$ is the contribution of a linear background and C is the amplitude of the Lorentzian.

The circular cylindrical cavity was made from two pieces of copper. The bottom and cylindrical sides were made from one piece and the top was separated and attached with screws. By constructing the cavity body from one piece instead of two, the losses resulting from the current flow between the cavity walls and bottom plate were minimized because there was no gap in the metallic interface. To increase the contact between the sides and top of the cavity, a tapered wall leading to a 0.060-in narrow flat surface was machined at the top of the body (Fig. 6.5). The cavity was 3.4 cm in length and 4.7 cm in diameter. The excitation frequency, which is related to the cavity dimension, for the TE011 mode was f = 8.9 GHz. The copper cavity was electroplated with 24K gold in order to avoid the degradation of the Q cavity over time from oxidation. Holes exist at the center of the top and bottom of the cavity. Samples are loaded into the cavity through the top hole. In the cavity walls there are six holes; the antennae are placed in two holes, the strings for the sample holder pass through two holes, and the loading of the sample is viewed through the final two holes. Inside the cavity is a sample holder consisting of a pair of quartz strings tautly stretched across the cavity, halfway up from the bottom (Fig. 6.6).

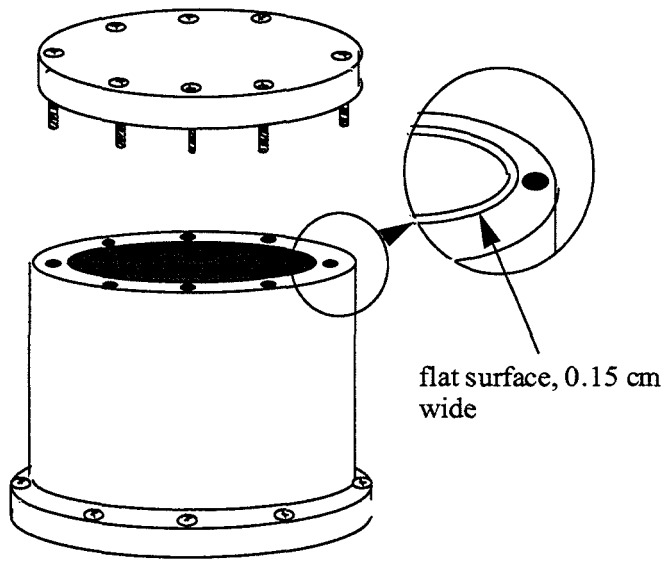

Figure 6.5. Cavity showing detail of narrow flat surface that makes contact with lid.

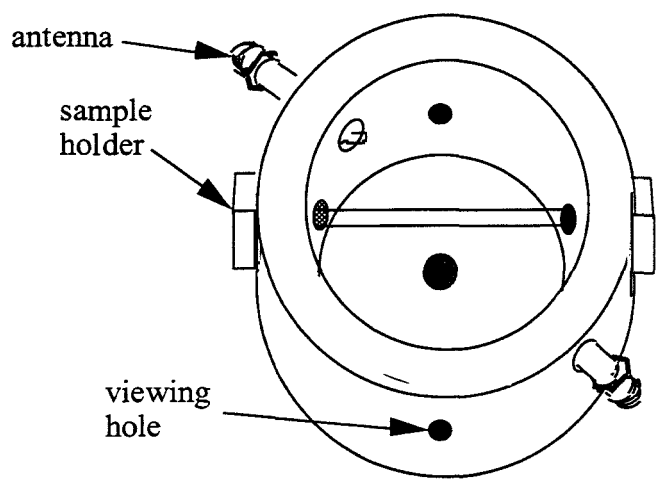

Figure 6.6. Inner view of microwave cavity.

A sample is loaded by placing it at the end of a thin aluminum rod. It is held in place by a vacuum pulled at the other end of the rod. The rod is then used to lower the sample into the chamber until it is just above the sample holder. The vacuum is then removed, the sample drops onto the strings, and the rod is removed from the chamber. Because the samples were made with tape, an electrostatic charge tended to build up on the samples, causing them to remain attached to the rod even after the vacuum was removed. To remedy this, a static gun and a radioactive source deionizing strip were used to make the samples electrostatically neutral.

The samples for the cavity perturbation measurements were thin disks of Ni_3Fe nanocrystalline powder sandwiched between two pieces of tape. Various Ni_3Fe powders were measured: as-milled 20:1, as-milled 5:1, and 5:1 annealed at 265°C and 600°C. The powders were sprinkled over two pieces of 3M 336 polyethylene tape, using sieves with a mesh of 0.038 mm. The sieves were used to remove large particles from the powder and to facilitate an even application of powder on the tape. The 3M 336 polyethylene tape was used because it was lightweight, thus less likely to affect the sample measurements. The two pieces of tape were then pressed together so that the powder was between them. For each Ni_3Fe powder type, a few tape and powder sandwiches were made. Tape sandwiches without any powder were also made.

From the various sandwiches, 0.25-in. diameter disks were made, using a hole punch. Each disk was separately labeled. Using an archaic yet elegant Magni-Grad FHM #42453 microbalance, the masses of the disks (~0.5 mg powder) were measured. If disks originating from one tape sandwich had a weight spread greater than 20%, all of those disks were discarded. The powder weight in each disk was then equated to the disk sample weight minus the average weight of the powderless disks.

Before and after the insertion of a sample, a voltage curve was taken for the empty cavity. The sample was then placed into the chamber (experiencing an applied field of ~20

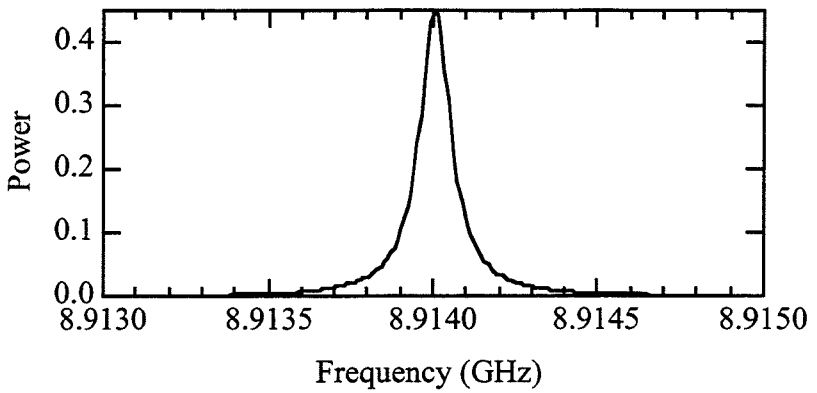

Figure 6.7. Typical voltage curve for an empty cavity.

Oe), and a voltage curve was collected. Fig. 6.7 shows a typical voltage curve for an empty cavity. For each voltage curve the Q and the resonance frequency were evaluated by fitting to a lorezntzian function. The empty cavity values of Q (~16000) and ω_r associated with each sample were taken as the average of the Q and ω_r of the voltage curves taken before and after insertion of the sample. The height of the sample, L, was assumed to be proportional to the sample weight because it was not possible to measure the powder thickness inside the tape sandwiches. Thus, the evaluated permeabilities are not absolute, but the relative permeabilites of the sample, with respect to each other, are valid. The evaluated permeabilities of samples from the same powder were then averaged together.

6.3 Results and Discussion

The real and imaginary permeability components for the various Ni_3Fe powders were plotted versus inverse grain size and RMS strain. Similarly to the DOS measurements, the real permeability seems to be more correlated to the grain size than it is to the RMS strain of the Ni_3Fe samples (Figs. 6.8 and 6.9). This suggests that grain size has a much larger effect on the real permeability than does the strain. This is contradictory to M-H loop measurements taken of the nanocrystalline samples and discussed in Chapter 5. These measurements indicated that strain strongly effects the real permeability.

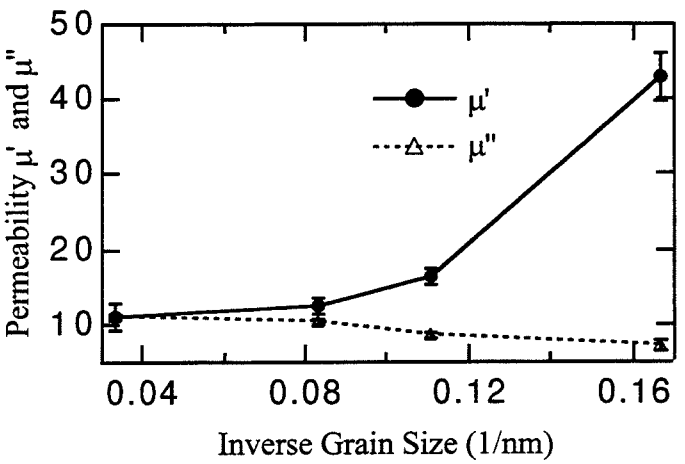

Figure 6.8. Real and imaginary components of permeability at 8.9 GHz versus inverse grain size.

I believe the source of this contradiction comes from the fact that the measurements were taken at one discrete frequency. The real and imaginary components of the frequency dependent permeability are not monotonic, but have a few maxima and minima, seen in frequency spectra like the one shown in Fig. 6.10. It is likely that the position of the maxima and minima would be affected by both the inverse grain size and the strain in the

nanocrystalline sample. Thus, if we measured over a range of frequencies, the permeability of one sample might be overall larger than that of a second sample. It is still possible that at a random frequency the first sample's permeability would be lower than the second's. I believe that the contradiction between the effects of strain and grain size, between the M-H loop measurements and the cavity perturbation measurements, most likely results from the measurements being taken at the discrete frequency of 8.9 GHz.

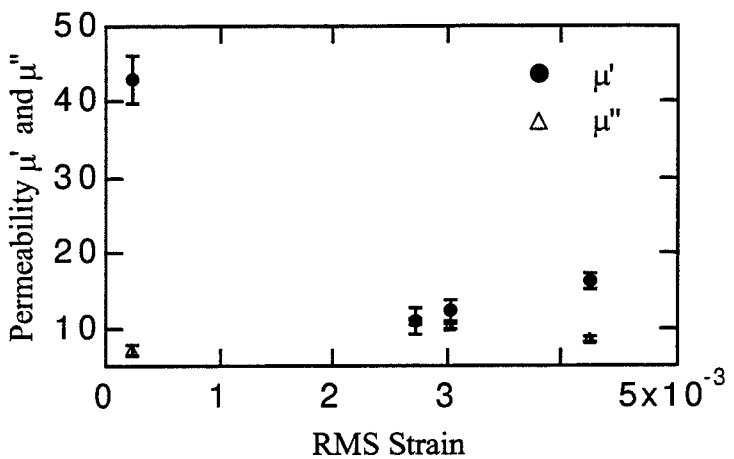

Figure 6.9. Real and imaginary components of the permeability versus RMS strain.

Using the real component of the permeability, μ', and resistivity, ρ (Chapter 4) , it is possible to calculate the skin thickness, s, at 8.9 GHz.

$$s = \frac{1}{2\pi}\sqrt{\frac{\rho}{\mu' f}}$$

where f is the frequency. This results in a skin thickness that is about 50 μm. From SEM images it was measured that the average powder particle size for 5:1 as-milled and 5:1 265°C annealed powders were 10 μm while the average size for the 5:1 600°C annealed samples was 160 μm. Because very little powder was place between the tape sandwiches, we can assume that the powder particles are isolated. Thus the magnetic field in the cavity will completely penetrate the powder particles in the 20:1 as-milled, 5:1 as-milled, and 5:1 265°C annealed samples. The powder particles of the 5:1 600°C annealed samples, which have large sized particles, will not be completely penetrated. This will add an error to the microwave permeability measurements of the 5:1 600°C annealed sample.

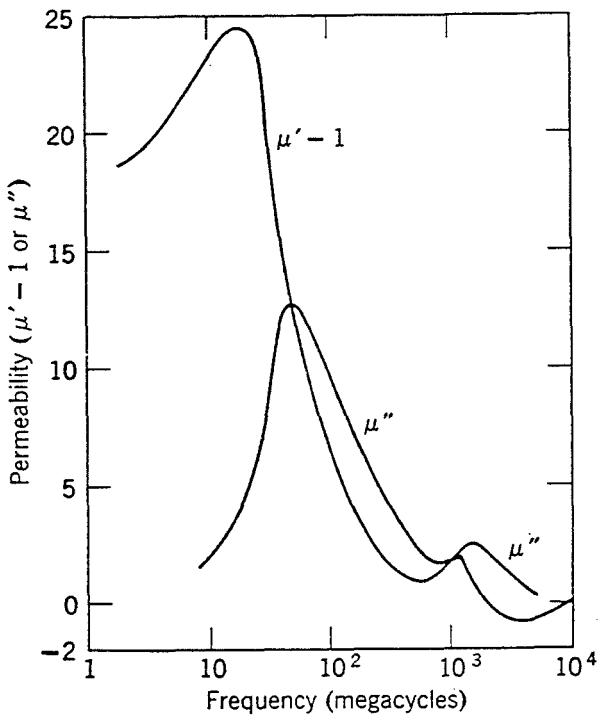

Figure 6.10. An example of a permeability frequency spectrum showing maxima and minima.[63]

Phonon DOS curves measured on the Ni_3Fe samples, discussed in Chapter 2, showed a strong relation between the grain size and the number of vibrational modes at energies <10 meV. Because the number of modes increased with a decrease in grain size, we believed that the smaller grain materials would be more absorptive to electromagnetic waves at microwave frequencies: however, Fig. 6.8 shows that μ_i, which is related to dissipative processes in material's lossyness, is little affected by the grain size. This limited effect of grain size might also be an artifact of making measurements at a discrete frequency.

6.4 Conclusion

The complex magnetic permeability was measured at 8.9 GHz for various nanocrystalline Ni_3Fe powders. The real permeability appeared to be more related to the inverse grain size than it was to the RMS strain. This contradicts results from B-H loop measurements, which showed that the strain affects the permeability. The real component of the permeability showed a large increase with a decrease in grain size, whereas the imaginary component remained relatively constant. This contradiction could result from evaluating the permeability at a single discrete frequency. To gain a more complete understanding of the effects of grain size and strain on the permeability, it would be better to measure the electromagntic response over a range in frequencies for the various nanocrystalline Ni_3Fe samples.

Chapter 7

Small Angle Neutron Scattering of Ni_3Fe Nanocrystals

We made small angle neutron scattering (SANS) measurements on nanocrystalline Ni_3Fe samples prepared by mechanical attrition with a 2:1 ball-to-powder weight ratio. The materials studied were 2:1 as-milled (when the material had a characteristic nanocrystal size of 15 nm), after annealing at 265°C (which relieved residual stress but caused little grain growth), and after annealing at 600°C (which promoted significant grain growth). The SANS measurements were performed with the specimens in applied magnetic fields up to 8 kG in order to separate the nuclear and magnetic scattering. For both the nuclear and magnetic scattering the 2:1 as-milled and the 2:1 265°C annealed powders had more scattering intensity than the 2:1 600°C annealed powder. The intensity increase originates from scattering from the nanocrystals. The 2:1 as-milled and the 2:1 265°C annealed powders had similar nuclear scattering, but the 2:1 as-milled had more magnetic scattering. This indicates that the two powders have similar nanocrystalline size distributions and grain boundary volume fractions, but have different magnetic features. The scattering from the 2:1 as-milled and 2:1 265°C annealed powders were modeled so that the average grain boundary magnetic moments of the powders could be estimated. The 2:1 as-milled powder had more magnetic scattering because it had a smaller average grain boundary magnetic moment. Radial distribution functions for the nuclear and magnetic scattering were calculated. They verified that the nanocrystals and their grain boundaries caused the increased scattering intensity for the 2:1 as-milled and the 2:1 265°C annealed samples compared to the 2:1 600°C annealed samples.

7.1 Experiment

Nanocrystalline Ni_3Fe powders were made by the mechanical attrition of Ni and Fe powders in a SPEX 8000 mixer mill, using hardened steel vials and balls. The powders were milled for 12 hr with 7.5 ml of ethanol and a ball-to-powder weight ratio of 2:1. The resulting powder was made of particles, about 10 μm in size, which were composed of a mosaic of nanocrystals.

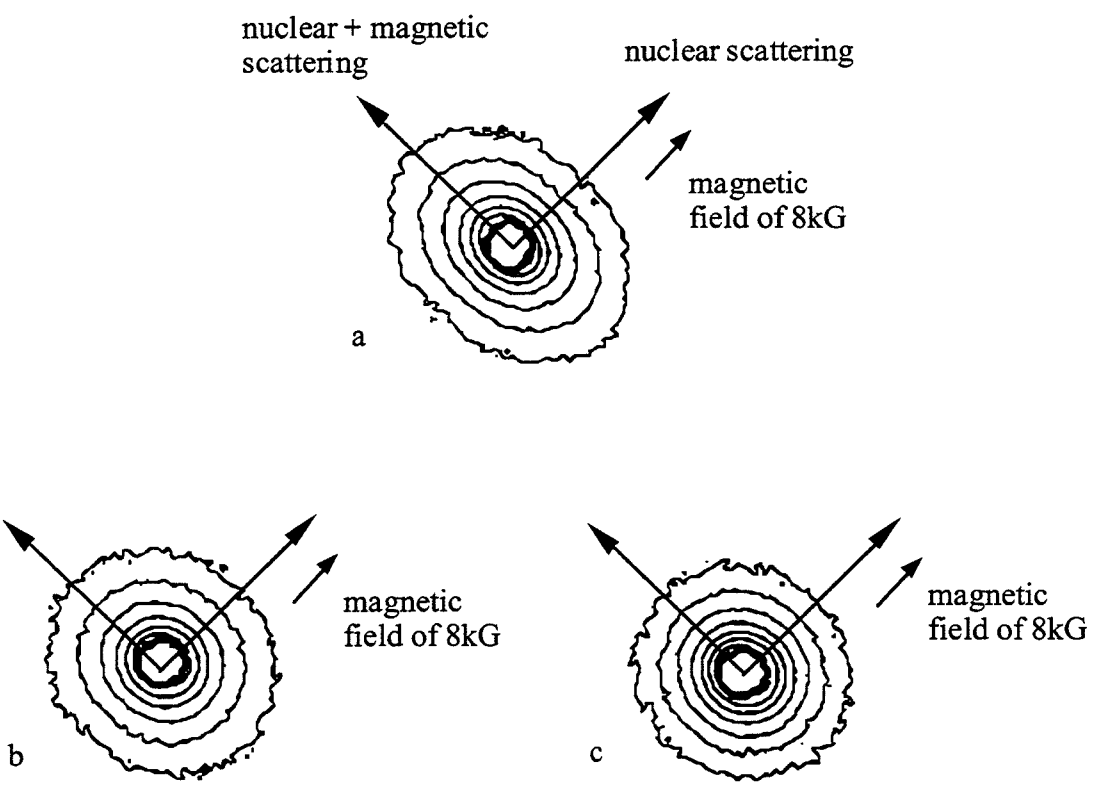

Figure 7.1. Scattering contour with direction indicators for the scattering profiles of a) 2:1 as-milled, b) 2:1 265°C annealed, and c) 2:1 600°C annealed powders.

The SANS measurements were performed using the 30-m Small Angle Neutron Scattering instrument (http://neutrons.ornl.gov/Instruments/HFIRInsts.HTML#30-mSANS) at the Oak Ridge National Laboratory, using a thermal neutron source and a Q range of 0.075 nm^{-1} to 0.6553 nm^{-1}. The powder samples, contained in 1-in. diameter and 0.25-in. thick glass "lollipops," were placed in an aluminum sample holder with a cadmium mask. The sample holder was positioned between the poles of a magnet, and fields from 0 to 8 kG were applied perpendicular to the neutron beam. With each new sample, the magnet was depolarized down to a few gauss. The scattering intensities were acquired with a two-dimensional area detector. The scattering intensities were corrected for background then calibrated using Porosil A standard scatterer, so that the data was converted to an absolute differential cross section per unit volume before analysis.

The 8 kG applied magnetic field allowed separation of the nuclear and magnetic scattering profiles. When a magnetic field is applied, the nuclear scattering is isotropic but the magnetic scattering is maximized perpendicular to the field. This is because in the presence of an applied field the total scattering intensity is

$$I_{total} = I_{nuc} + I_{mag} \sin(\alpha)$$

where α is the angle between the scattering and magnetization vectors[64]. I_{nuc} and I_{mag} are described later in Section 7.4. Thus the magnetic scattering decreases continuously to zero for directions parallel to the applied field. From two-dimensional intensity scattering profiles, sector averages (over a $\pm 5^{\circ}$ range) were taken at various angles. The sector average with the largest integrated intensity was chosen as representing the nuclear plus magnetic scattering profile, whereas the sector perpendicular to this was only the nuclear scattering profile (Fig. 7.1). By subtracting the nuclear scattering profile from the nuclear plus magnetic scattering profile, the magnetic scattering profile was obtained. Thus when

I_{mag} is later modeled in Section 7.4, the $\sin(\alpha)$ is dropped since magnetic scattering profile was extracted when maximized.

Scattering intensities were also acquired for applied fields of 5 to 6000 G. Little change was seen in the magnetic scattering profiles, even over the 5 to 100 G range of applied fields in which the material was not yet saturated. There were probably changes in the magnetic domain structures over this range of applied field, but because of the large size of the domains and the Q range measured, the magnetic profiles were unaffected.

7.2 Physical Features of the Nanocrystalline Ni_3Fe Powders

The nanocrystalline Ni_3Fe powders consist of large ~10 μm sized particles, which are composed of a three-dimensional mosaic of nanocrystals separated by grain boundaries. From the Mössbauer spectra discussed in Chapter 4, it is known that the volume fraction of nanocrystals is approximately 0.9, with the remaining volume occupied by the grain boundaries. From previous work, it is known that the grain boundaries have a width of about 0.5 nm[55]. The density of the grain boundaries is less than that of the nanocrystals. However, how much less dense are the grain boundaries is still a subject of debate, with the density ranging from 60% to 90% of the bulk material[11,65].

TEM dark field micrographs were used to find the size distribution of the nanocrystals. Fig. 7.2 shows TEM micrographs of 2:1 as-milled, 2:1 265°C annealed, and 2:1 600°C annealed nanocrystals. To evaluate the size distributions of the nanocrystalline powders, random lines were drawn through the micrographs of the 2:1 as-milled, 2:1 265°C annealed, and 2:1 600°C annealed samples. When a line crossed a nanocrystal, the intersection length was measured. Comparing the micrographs of the 2:1 as-milled and the 2:1 annealed at 265°C powders, we see that there is negligible change in the nanocrystal

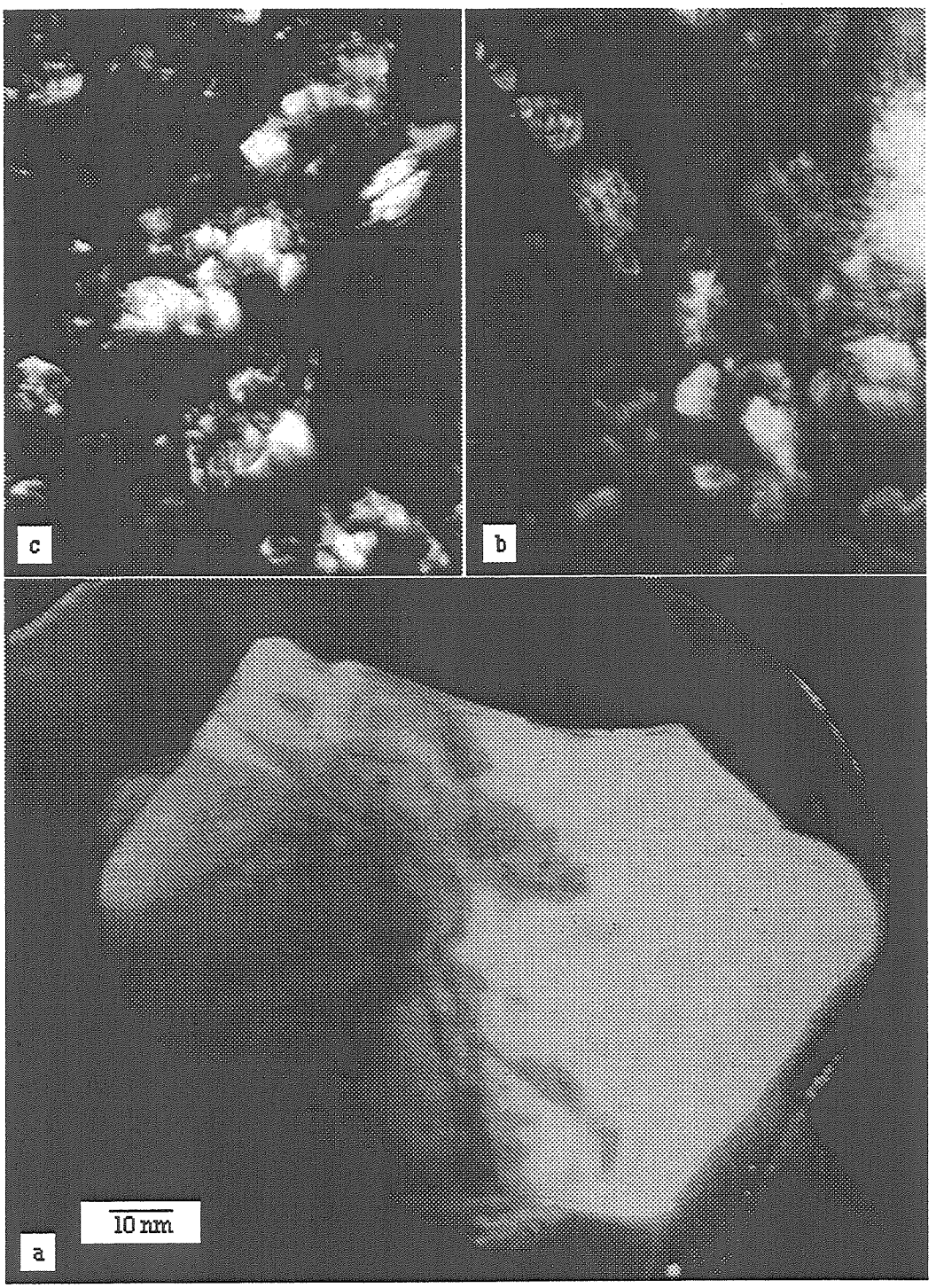

Figure 7.2. TEM of dark field images from (111) fcc diffraction of Ni_3Fe powders (a) 2:1 as-milled, (b) 2:1 265°C annealed, (c) 2:1 600°C annealed.

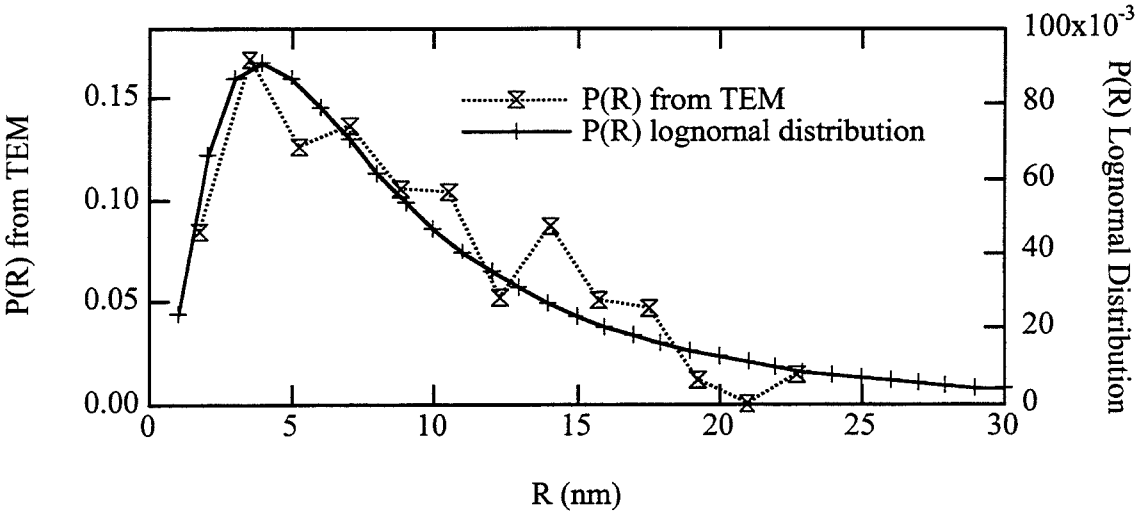

Figure 7.3. Size distribution of nanocrystals in 2:1 as-milled and 265°C annealed Ni_3Fe powder. Shown are both the size distribution evaluated from TEM micrographs and the lognormal fit.

size distribution upon annealing at 265°C. This conclusion is supported by the x-ray diffraction results (Chapter 2), which showed little crystal growth, but a reduction in strain after annealing at such low temperatures. The size distributions of the 2:1 as-milled and 2:1 265°C annealed were assumed to be the same, so the lengths measured from the micrographs were added together in order to improve the statistics. The measured lengths were compiled into a distribution of lengths, $P(\ell)$, which was then converted into a distribution of spheres, P(R), with a radius R (Fig. 7.3 and Fig. 7.4) where

$$P(\ell) = \int_0^\infty \frac{1}{4R\sqrt{R^2 - \ell^2/4}} P(R)dR \qquad (7.1)$$

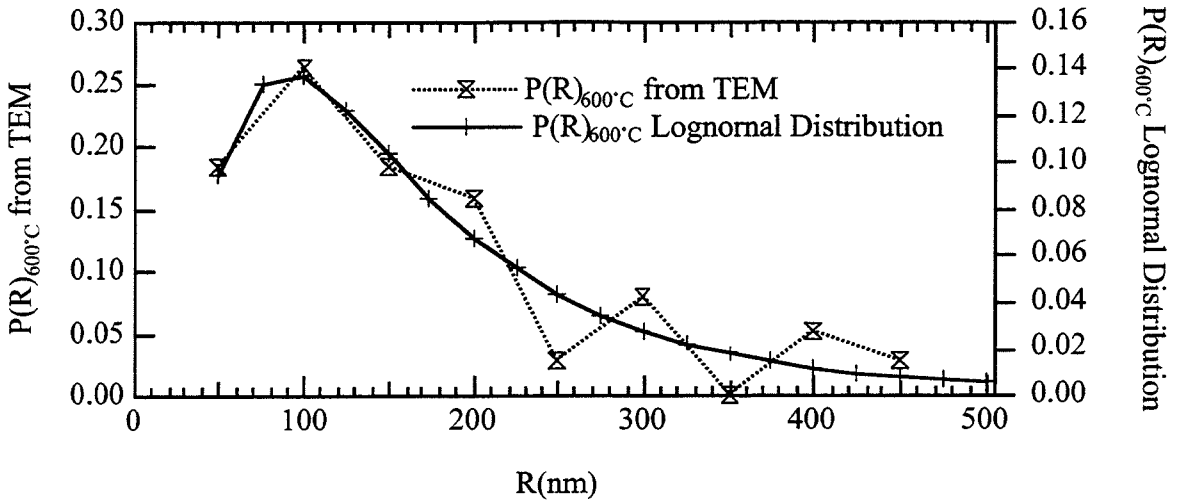

Figure 7.4. Size distribution of nanocrystals in 2:1 600°C annealed Ni_3Fe powder. Shown are both the size distribution evaluated from TEM micrographs and the lognormal fit.

This integral relates $P(\ell)$ to all the possible lengths, ℓ, given a distribution of radii, P(R). To extract P(R), Eq. 7.1 is converted into a discrete sum from 0 to N, the largest measured intersecting length.

$$P(\ell) = \sum_{0}^{N} \frac{1}{4R\sqrt{R^2 - \ell^2/4}} P(R)\Delta R \qquad (7.2)$$

P(R) can be calculated if it is assumed that particles with the maximum diameter can be accurately measured (that their centers are in the TEM image) [66]. Thus, the R and ℓ coincide at the upper end, N, of the size distribution and $P(R=N) = P(\ell=N)$. P(R) can then be calculated from $(N-\Delta R)$ to 0. The resulting P(R)'s were then fit to lognormal distributions that had a cut-off size of 3 nm. In the fitting procedure, the breadth of the lognormal distribution was altered until the average size of the distribution matched that

obtained from P(R) calculated from the TEM micrographs. From the TEM images the combined average size for the 2:1 as-milled and the 2:1 265°C annealed was 17.4 nm. X-ray diffraction results gave the average column length for the 2:1 as-milled as 15 nm and the 2:1 265°C annealed as 20 nm. When these sizes are converted from average column to average radius lengths of the nanocrystals, it is found that they are larger than those derived from TEM. This discrepancy is probably from misinterpreting a large crystal as a group of smaller crystals. X-ray diffraction patterns give averages sizes of 22-nm and 30-nm. TEM micrographs showed the average crystal size of the 2:1 600°C annealed as 300 nm.

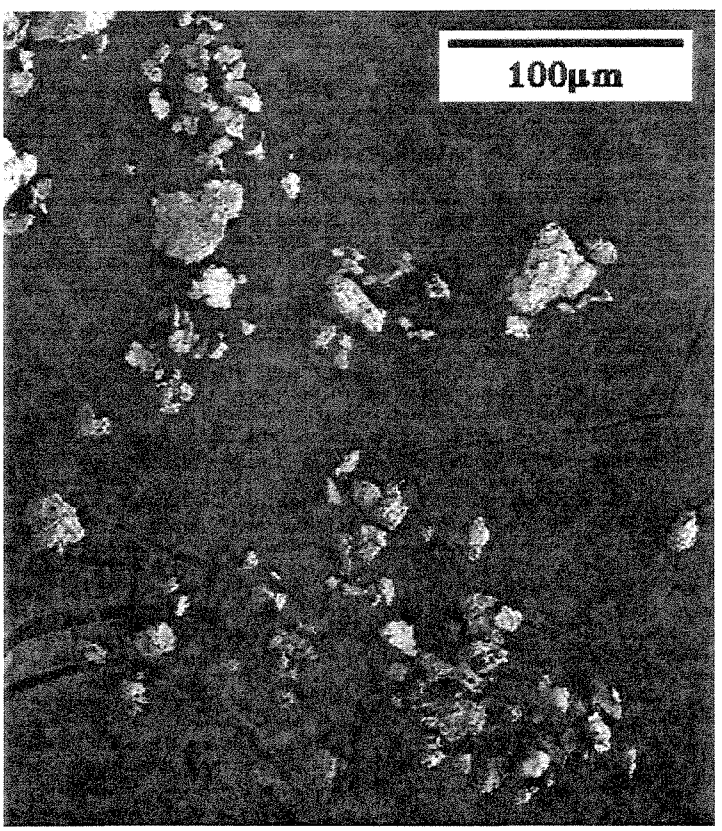

Figure 7.5. SEM image showing the particles of 2:1 as-milled nanocrystalline Ni_3Fe powder on carbon tape.

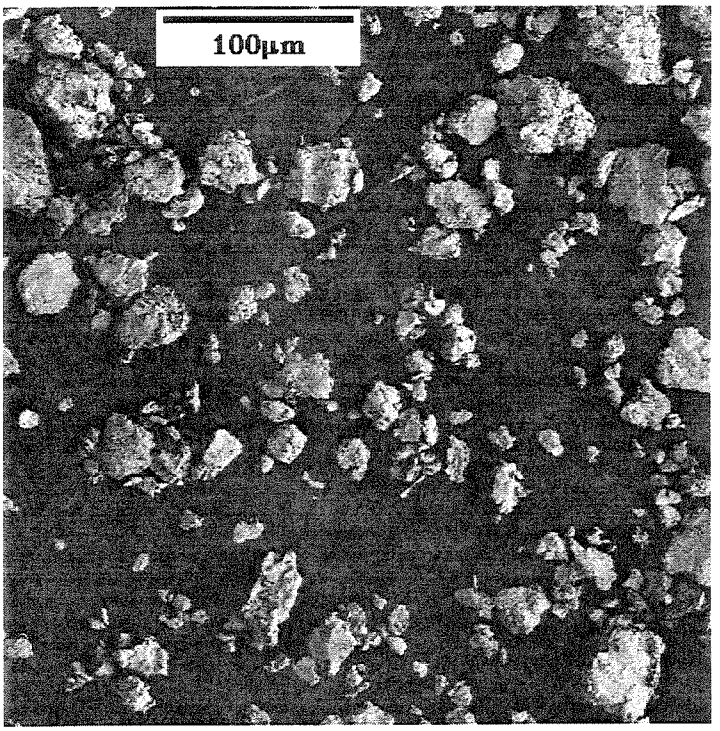

Figure 7.6. SEM image showing the particles of the 2:1 600°C annealed Ni_3Fe powder on carbon tape.

The SEM images of the powders were obtained with a Camscan Series II scanning electron microscope. From the SEM images (Fig. 7.5 and Fig. 7.6), the size distribution of particles, $P_{part}(R)$, was determined by using the program NIH Image to outline individual particles and evaluate their enclosed areas. These measured areas were compiled to determine the particle area distribution, $P_{part}(Area)$. The particles were approximated as spheres, easily enabling the conversion

$$P_{part}(R) = \sqrt{\frac{P_{part}(Area)}{\pi}}$$

This was then fit to a lognormal distribution (Fig. 7.7 and 7.8). The average particle size for the 2:1 as-milled and the 2:1 265°C annealed is 8 μm and for the 2:1 600°C annealed is 10 μm.

From the SEM images, it can be seen that many particles do not have smooth surfaces. Instead, the particles have many cracks, and the particles appear "flaky," as if composed of joined platelets (Fig. 7.9). These features are found in all of the Ni_3Fe powders studied regardless of temperature treatments. However, it is possible that there are features, 0.1 μm or less in size, which are present in the 2:1 as-milled and 265°C annealed samples but not in the 600°C sample.

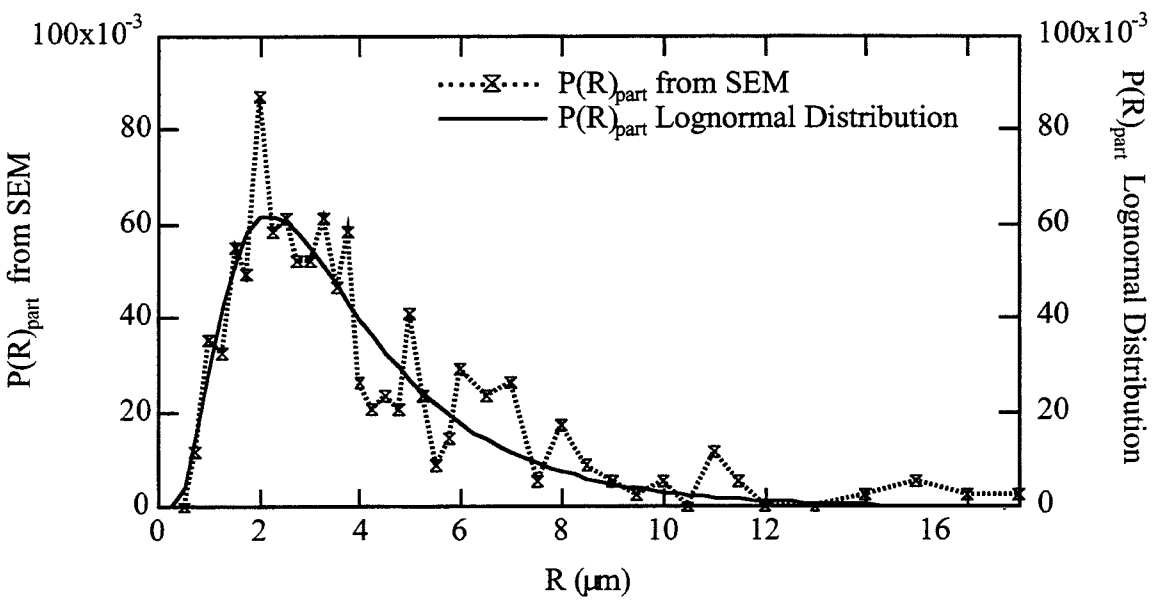

Figure 7.7. Size distribution of particles in 2:1 as-milled and 265°C annealed Ni_3Fe powder. Shown are both the size distribution evaluated from SEM images and the lognormal fit.

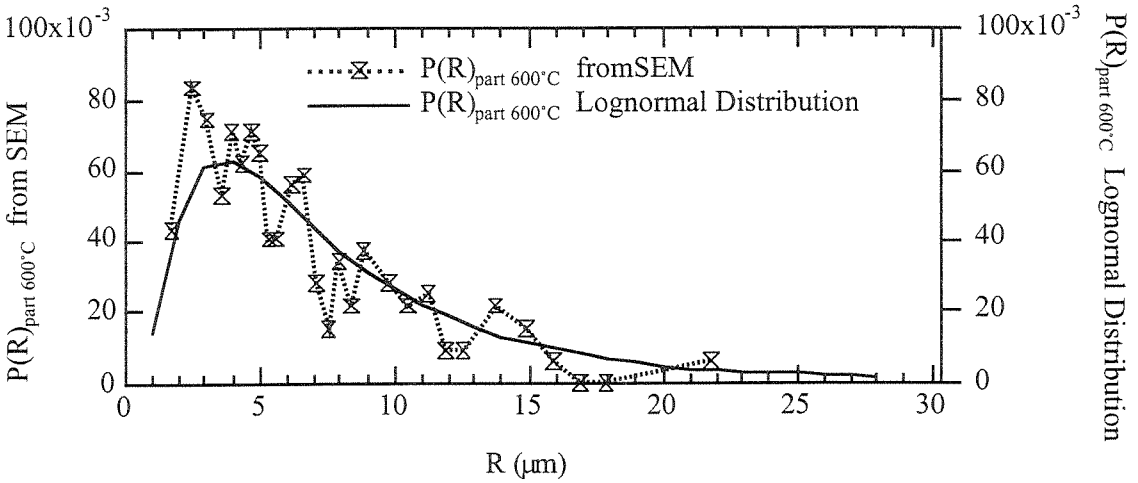

Figure 7.8. Size distribution of particles in 2:1 600°C annealed Ni_3Fe powder. Shown are both the size distribution evaluated from SEM images and the lognormal fit.

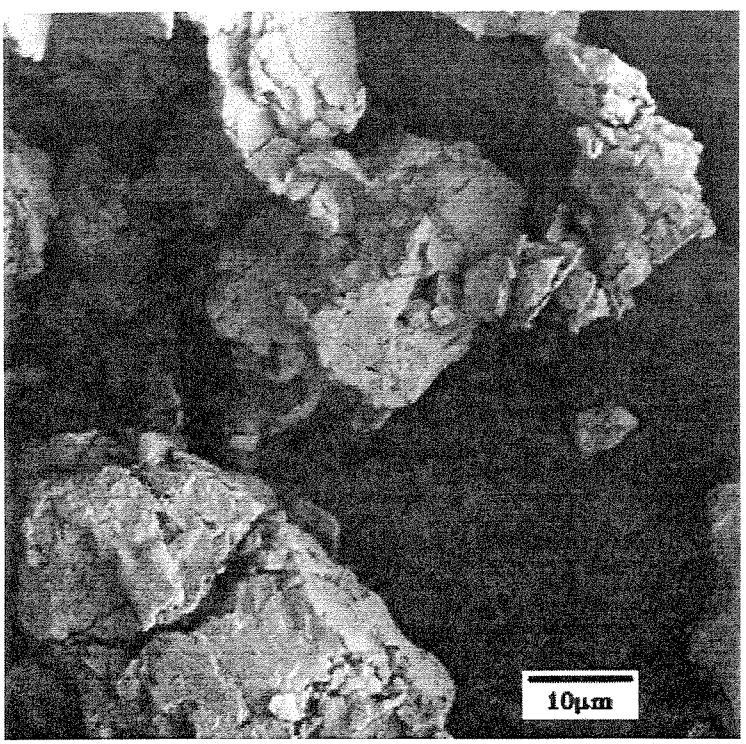

Figure 7.9. SEM image of Ni_3Fe powder particles as-milled with a 2:1 ball-to-powder weight ration 2:1, showing surface cracks and a "flaky" appearance of the particles.

7.3 Small Angle Neutron Scattering

Small angle neutron scattering intensity is affected by many characteristics of the scatterer. A key characteristic is the difference between the nuclear density or magnetic moment density of the scatterer and its surrounding matrix. For example, the surrounding matrix of the nanocrystals would be the grain boundaries which are less dense. For the large powder particles, the surrounding matrix would be a void (air). Important characteristics are also the number density, size distribution, and shape of the scatterer. These characteristics are all related to the size of the scatter with the shape of the scattering also being functionally dependent upon Q. At particular Q values, the combination of these characteristics will cause some scatterers to either be too large or too small to contribute significantly to the total scattering intensity. For example, in the Q range measured, the powder particles were too large and crystal defects were too small to contribute much to the scattering intensity.

Packing density of the scatterers also affects the scattering intensity. If the scatterers are too close to each other, there will be interference causing a reduction in the intensity profile characteristic of each scatterer. To understand the concept, consider an extreme case where the scatterers are so densely packed that they fill all space. In this scenario there is no variation in nuclear density or magnetic moment amplitude and hence the intensity profile from each scatterer would be zero. Somewhere between no scatterers and space filled with scatters there must be a maximum in intensity profile of the individual scatterer versus density of scatterers. After the density of scatters exceeds this critical point, the scatterers interfere causing the intensity to decrease.

It was not possible to model accurately the scattering because there are too many factors unknown about the nanocrystalline Ni_3Fe powders. Unknown factors include the shape distribution of all the possible scatterers, the size distribution of "crack" features in the powder particles, and the grain boundary atomic density. From TEM images it was

possible to gauge the size distributions but not the shape distributions of the crystals in the powders. SEM images showed that the powder particles had surface cracks and a "flaky" appearance. These crack features could contribute to the scattering profiles. In fact, approximate modeling of the crack features as spheres showed that if they were 100 nm in diameter, they would contribute significantly to the scattering. The most important unknown factor is the grain boundary density. The density of the grain boundaries is still in dispute with experiments estimating it from 60% to 90% of the bulk material[11,65]. If the density of grain boundaries is 60%, the scattering from the nanocrystals will be 16 times larger than if the density is 90%.

Due to all the difficulties of modeling the scattering, I do not believe it is possible to give an accurate model of scattering from the powders examined. I used differences in the scattering profiles of the powders to draw conclusions about the scattering sources and the grain boundary average magnetic moments. I then used an approximate model of the scattering profiles to estimate the grain boundary average magnetic moments.

7.4 Nuclear and Magnetic Scattering Profiles

Fig. 7.10 shows the nuclear scattering profiles from the 2:1 as-milled, 2:1 265°C annealed, and 2:1 600°C annealed Ni_3Fe powder samples. The scattering from the 2:1 as-milled and the 2:1 265°C powders are similar, and both are more intense than the scattering from the 2:1 600°C annealed sample. The 2:1 600°C powder is different from the other two in that it has larger powder particles (~10 μm) and larger crystals in the powder particles (~300 nm). All three powders have "crack" features. The powder particles in all three samples are too large to contribute significantly to the scattering. Thus, possible scatterers for the 2:1 600°C annealed powder are the "crack" features and the ~300 nm

crystals with grain boundaries. For the 2:1 as-milled and 2:1 265°C annealed, they are the "crack" features and the nanocrystals. The difference in scattering intensity must originate from the nanocrystals scattering more intensely than the large ~300 nm crystals. The similarity of the 2:1 as-milled and the 2:1 265°C annealed samples indicates that they have similar density morphologies, i.e., they have the same nanocrystalline size distributions and grain boundary volume fractions. Although x-ray diffraction results and Mössbauer spectra have shown that there is some change in the size distribution and grain boundary volume fraction upon annealing the 2:1 as-milled powder at 265°C, the changes cause only the small intensity increase observed at higher Q.

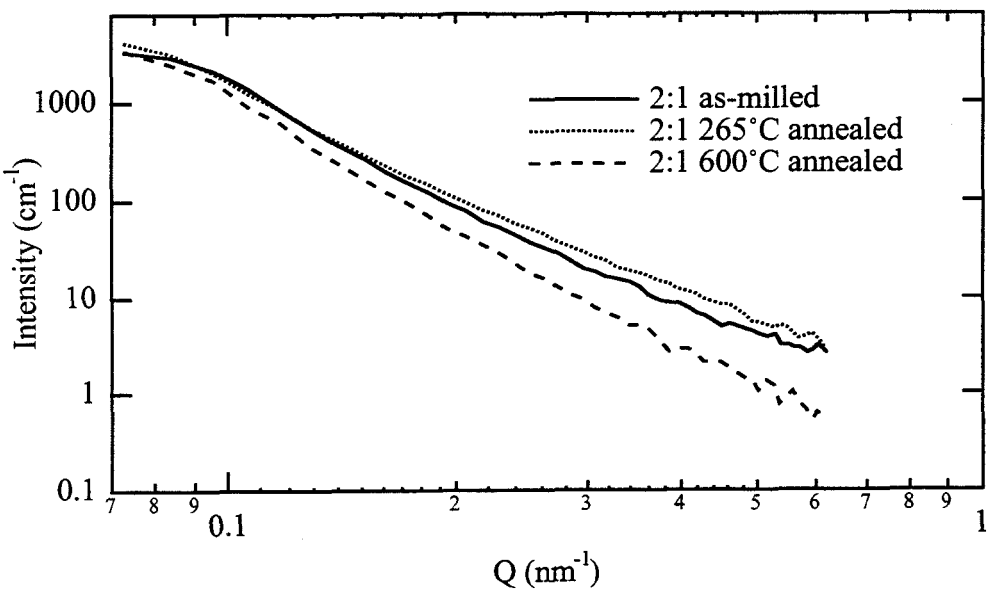

Figure 7.10. Nuclear scattering profiles for the 2:1 as-milled, 2:1 265°C annealed, and 2:1 600°C annealed Ni_3Fe powder samples.

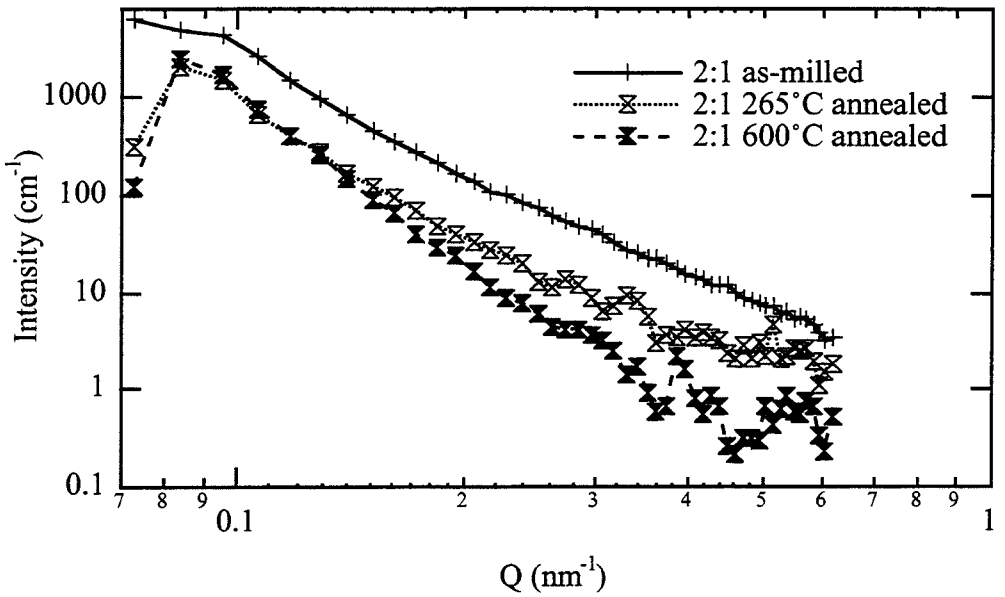

Figure 7.11. Magnetic scattering profiles for the 2:1 as-milled, 2:1 265°C annealed, and 2:1 600°C annealed Ni_3Fe powder samples.

For the magnetic scattering profiles (Fig. 7.11) the scattering intensity of the 2:1 as-milled powder is greater than that of the 2:1 265°C annealed powder, and the 2:1 600°C annealed powder has the lowest intensity. Scattering from the nanocrystals caused the nuclear scattering intensities from the 2:1 as-milled and 2:1 265°C annealed powders to be larger than the nuclear scattering from the 2:1 600°C annealed powder, and a similar trend may be expected for the magnetic scattering profiles. However, although the 2:1 as-milled and the 2:1 265°C annealed samples had similar nuclear scattering intensity profiles and similar density morphologies, the difference in their magnetic scattering profiles indicates that the powders have different magnetic morphologies associated with the nanocrystals. The size distributions and grain boundary volume fractions do not differ enough to cause this effect. It is most likely that this difference in magnetic scattering originates from the differences in average grain boundary magnetic moments of the nanocrystalline materials.

Since the scattering from the 2:1 as-milled powders is larger, it must have a larger difference in magnetic moment density between the nanocrystals and the grain boundaries. This means that the average grain boundary magnetic moment of the 2:1 as-milled powder is smaller than for the 2:1 265°C annealed powder. This could originate from changes in the local atomic order upon the low temperature annealing. Previous work has shown that the grain boundaries of nanocrystalline materials have a broad distribution of interatomic distances with low atomic coordination numbers[67] and that the severe nonequilibrium displacement of atoms in the grain boundaries results in an increased internal energy in the grain boundary[68]. It is possible that, upon annealing, the atoms in the grain boundaries make small movements into to a lower energy configurational state, creating some short range order and causing the increase in magnetic moment amplitude.

7.5 Modeling of Small Angle Neutron Scattering

The nuclear and magnetic scattering from the 2:1 as-milled and 2:1 265°C annealed powders were modeled in order to estimate the average grain boundary magnetic moments. Considered as possible scattering sources were the nanocrystals, the large powders particles, and cracks in the particles. In preliminary calculations, using the size distribution described in Section 7.2, and assuming the large powder particles were spherical, the calculated scattering from the powder particles was 3 orders of magnitude lower than the experimental scattering intensity. Scattering from the powder particles was therefore not included in the model. Preliminary calculations also showed that scattering from spherical "crack" features of 100 nm of 0.05 volume fraction had a scattering intensity of the right magnitude, so scattering from "crack" feature could be contributing to the measured scattering intensities if their volume fraction were as high as 0.05. It was not possible to evaluate the size or shape distributions of the crack features.

Only the scattering from the nanocrystals was modeled. The nanocrystals were modeled as spheres and were assumed to scatter against the contrasting grain boundary matrix. The size distributions of the scatterers were derived from TEM images (Section 7.2). The number density was derived by using the calculated size distributions, density measurements of the powder, and grain boundary volume fractions derived from Mössbauer spectra (Chapter 4). Interference from the dense packing of scatterers was not included in the model.

The scattering intensity from a collection of scatterers, with a size distribution, P(R), is defined by the relation

$$I = NP(R)\Delta\rho^2V^2F^2(QR)$$

where N is the number density of scatterers, $\Delta\rho$ is the difference in either the nuclear or magnetic scattering amplitude between the scatterer and its matrix, V is the volume of the particle, and F(QR) is the form factor of the scatterer. For a spherical scatterer,

$$F_{sphere}(QR) = \left[3\frac{\sin(QR) - QR\cos(QR)}{(QR)^3}\right]$$

The number densities associated with a scatterer were derived by dividing the volume fraction that the scatterer occupies by the average volume of the scatterer, which was calculated from the size distributions. Determined by weighing the powder in a fixed volume, the density of the powder was 50% that of bulk Ni_3Fe. Thus the volume fraction of the powder particles is 0.5. The volume fraction of the nanocrystals within the powder is (volume fraction of powder particles = 0.5) * (volume fraction of nanocrystals occurring

in the powder particles = 0.9). The rest of the volume in the powder particles is occupied by the grain boundaries. The volume fraction of nanocrystals in the powder particles was derived from Mössbauer spectroscopy (Chapter 4).

For Ni_3Fe, the nuclear scattering length density, ρ_N, is 9.2 x 10^{10} cm^{-2}. For the nanocrystals, ρ_N was assumed to be equal to that of bulk Ni_3Fe. Since the grain boundaries density is not known, I chose 80% that of bulk Ni_3Fe because it allowed the accurate modeling of the data. If interference effects had been included in the model, it would have been necessary to use a smaller grain boundary density. For scattering associated with both the grain boundaries and the nanocrystals, $\Delta\rho_N$ =1.84 x 10^{10} cm^{-2}. The measured nuclear scattering intensities along with the modeled intensity are shown in Fig. 7.12.

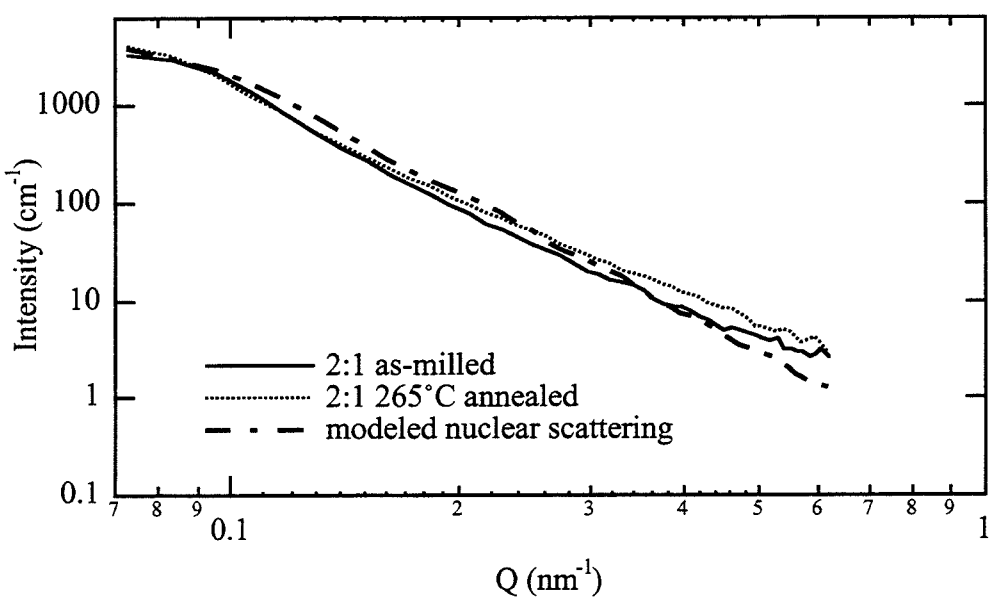

Figure 7.12. Nuclear scattering profiles and modeled scattering from 2:1 as-milled and 2:1 265°C annealed Ni_3Fe powder.

The models for the nuclear scattering were used as a template for the modeling of the magnetic scattering. The formulas used to model the magnetic scattering are the same as those used to model the nuclear scattering except that $\Delta\rho_N$, the nuclear-scattering length difference, is replaced by $\Delta\rho_M$, the magnetic scattering length difference. Thus nuclear scattering from the nanocrystals, as discussed above, merely has to be multiplied by the ratio $\Delta\rho_M/\Delta\rho_N$ to represent the magnetic scattering. The magnetic scattering length is proportional to the magnetic moment of the material. Thus the $\Delta\rho_M/\Delta\rho_N$ ratios associated with the powders are different and the average grain boundary magnetic moments for the two powders can be extracted.

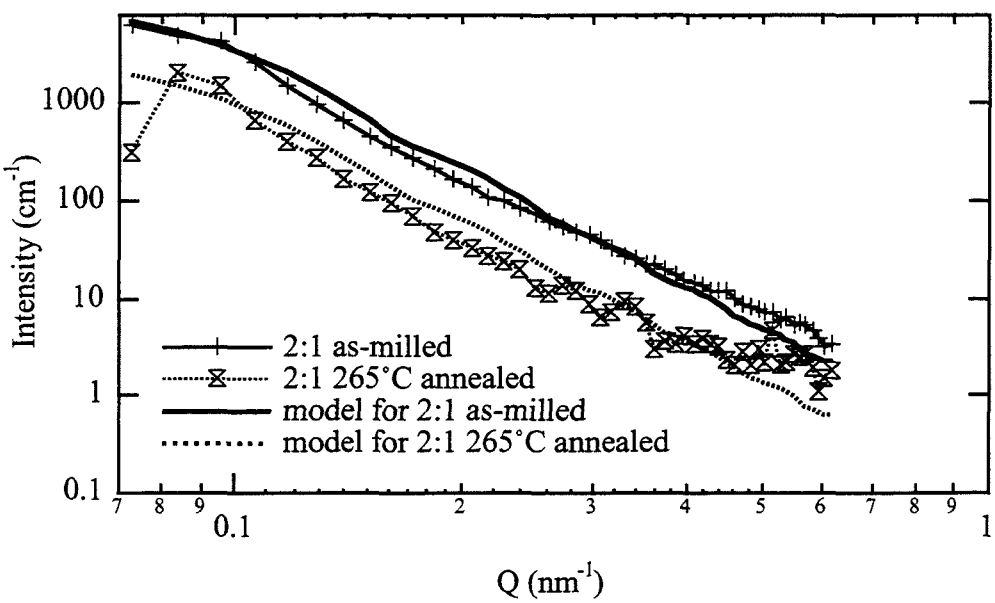

Figure 7.13. Magnetic scattering profiles and modeled scattering from 2:1 as-milled and 2:1 265°C annealed Ni_3Fe powder.

Fig. 7.13 shows the measured and modeled magnetic scattering for the 2:1 as-milled and 265°C annealed powders. To model the magnetic scattering intensity, the grain boundary magnetic moments of the 2:1 as-milled and 265°C annealed powders would have to be, respectively, 0.7 μ_B and 0.9 μ_B compared to the magnetic moment of the nanocrystal, 1.2 μ_B. Because interference effects, which would reduce the modeled intensity, were not included, it is expected that the respective grain boundary magnetic moments are actually lower than the model indicates. This seems reasonable compared to the respective magnetic moments of 0.6 μ_B and 0.8 μ_B evaluated approximately using Mössbauer spectra.

7.6 Radial Distribution Functions

The nuclear and magnetic scattering profiles were converted into radial distribution functions, RDF, by Fourier transforming the intensity profiles, I(Q):

$$\mathrm{RDF}(r) = \frac{1}{4\pi r} \int_{-\infty}^{\infty} Q \sin(Qr)\, I(Q)\, dQ$$

It was assumed that the nuclear and magnetic intensity profiles of the 2:1 600°C annealed sample represented scattering from all non-nanocrystalline scatterers. Therefore, to evaluate the RDF's associated with the nanocrystals, the RDF for the 2:1 600°C annealed samples was subtracted from the RDF's for the 2:1 as-milled and the 2:1 265°C annealed samples. The resulting RDF's are shown in Fig. 14.

The most noticeable feature of Fig. 14 is that the two RDF's associated with the nuclear scattering of the 2:1 as-milled and 2:1 265°C annealed samples are similar while their

corresponding magnetic RDF's are not. This confirms that the two samples have similar density characteristics but have different magnetic characteristics. The RDF's for the two nuclear scattering profiles and for the magnetic scattering profile of the 2:1 as-milled all go to zero at ~30 nm. Since this is approximately the largest diameter of the nanocrystals, it can be concluded that the extra scattering intensity present in the corresponding intensity profiles originates from the nanocrystals. The RDF of the 2:1 265°C magnetic scattering profile is close to zero over the entire range of r, indicating that there is little scattering originating from the nanocrystals. This supports the conclusion that the 2:1 265°C annealed sample has smaller magnetic moment density variation between the nanocrystals and grain boundaries than the 2:1 as-milled sample. The oscillations of the RDF's that occur after the first zero are end effects associated with the finite range of Q for Fourier transformation.

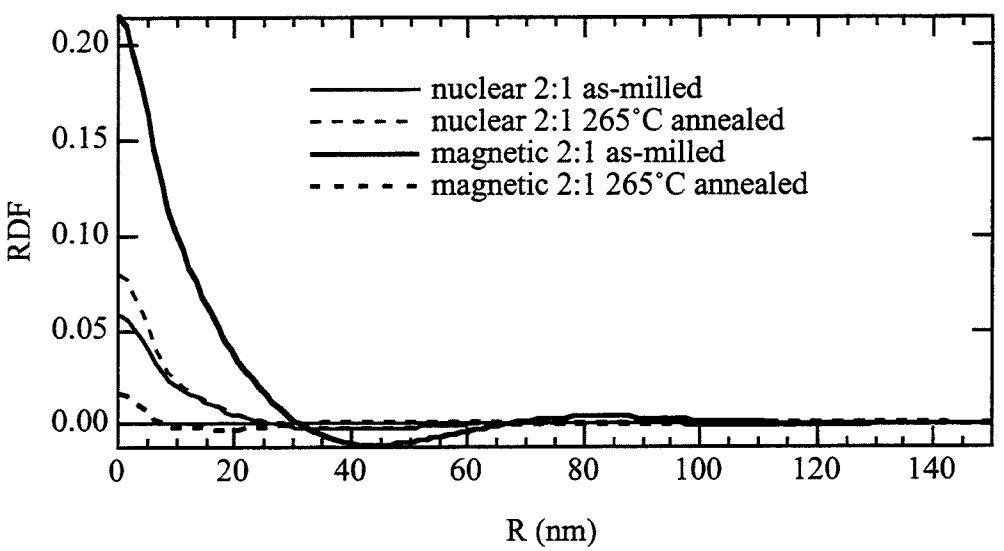

Figure 7.14. Radial distribution functions for the 2:1 as-milled and 2:1 265°C annealed minus the 2:1 600°C annealed radial distribution function.

7.7 Conclusions

By comparing the nuclear and magnetic scattering from small angle neutron scattering of 2:1 as-milled, 2:1 265°C annealed and 2:1 600°C annealed powders, it was shown that the grain boundary magnetic moment amplitudes changed upon annealing at 265°C. Over the Q range of 0.075 nm^{-1} to 0.6553 nm^{-1}, nuclear scattering in the 2:1 as-milled and 2:1 265°C annealed powders originates from the nanocrystals and possibly from "crack" features present in the large particles which are composed of the nanocrystals surrounded by grain boundaries. The magnetic scattering intensity of the 2:1 as-milled was larger than the 2:1 265°C annealed powder, indicating that the grain boundary magnetic moment amplitudes were smaller in the 2:1 as-milled than in the 2:1 265°C annealed powder. Modeling of the magnetic scattering of the 2:1 as-milled and 2:1 265°C annealed powder indicated that the grain boundary magnetic moment amplitudes were 0.7 μ_B and 0.9 μ_B, respectively. Conversion of the intensity profiles into radial distribution functions confirmed that scattering originating from nanocrystals was present in the intensity profiles of the 2:1 as-milled and 2:1 265°C annealed samples. The radial distribution functions also verified that the grain boundary magnetic moment density of the 2:1 as-milled was smaller than the 2:1 265°C powder.

Chapter 8

Conclusions and Future Work

The vibrational and magnetic properties of mechanically attrited Ni_3Fe nanocrystals were studied. Both properties differed between the bulk and nanocrystalline Ni_3Fe. In general, these differences originated from the grain boundaries in the nanocrystalline materials.

8.1 Conclusions

Vibrational phonon densities of states obtained from inelastic neutron scattering measurements showed that, at low energies, the amount of scattering scaled with the volume fraction of grain boundaries. Furthermore, the room temperature phonon DOS of the 20:1 as-milled powder, which had the highest density of grain boundaries of the powders studied, was different from the phonon DOS of the same powder after it had been exposed to 10 K. It is believed that the changes in the phonon DOS upon cryogenic exposure originate with changes in the local atomic structures of the grain boundaries.

Calculations of the vibrational frequencies of the small particles done by Tamura et al.[44-46] showed that surface modes augmented the frequency spectrum at low frequencies with smaller particles having a larger fraction of surface modes. This was an effect found in the derived nanocrystalline phonon DOS.

Evidence for atomic changes in grain boundaries was seen in Mössbauer spectra and small angle neutron scattering. The Mössbauer spectroscopy showed that, upon annealing

at 265°C, the magnetic moments of the grain boundaries increased. This is most likely due to slight rearrangements of grain boundary atoms during the low temperature annealing. Furthermore, stress relief upon annealing should affect intra-crystal grain boundary contacts and hence the magnetic properties of the material. Small angle scattering showed that the magnetic scattering intensity from 2:1 as-milled Ni_3Fe was greater than that from the 2:1 265°C annealed powder also indicating that the magnetic moments of the grain boundaries were less in the 2:1 as-milled powders than in the 2:1 265°C annealed powder.

Because the phonon DOS of the nanocrystalline Ni_3Fe was enhanced at low energies, we expected that the material would be more absorptive at GHz frequencies than the bulk material. To test this hypothesis, measurements of the magnetic permeability at 8.9 GHz were taken, using the microwave cavity perturbation method. We expected the increase in absorption to manifest itself as an increase in the imaginary component of the permeability. However, measurements showed that the volume fraction of grain boundaries had very little effect on the imaginary component of the permeability. Furthermore, the measurements of the real permeability behaved in a manner contrary to the trend found for the low frequency permeability measured from M-H magnetization curves. I believe these contradictions are an anomaly arising from measuring the permeability at the discrete frequency of 8.9 GHz, and that frequency-dependent measurements of the permeability would show that the imaginary permeability of the nanocrystalline powder was generally augmented at GHz frequencies.

8.2 Future Work

Mössbauer spectroscopy and SANS studies of samples which have been thermally treated to cause changes in the grain boundary structure would show more clearly how grain boundary structure relates to the grain boundary magnetic moments. Because

annealing reduces strain and causes grain growth, it would be better to use exposure to cryogenic temperature rather than annealing to change slightly the grain boundaries. Therefore, 20:1 as-milled Ni_3Fe, which has a high volume fraction of grain boundaries, would be exposed to liquid nitrogen and liquid helium. Mössbauer spectra would then be taken of the two cryogenic temperature exposed samples and a room temperature sample to see how the exposure affected the magnetic properties of the grain boundaries. SANS measurments would be taken to confirm observed changes in the grain boundary magnetic moments.

To gain more insight into whether the augmentation of phonon DOS affects the microwave absorption of the nanocrystalline Ni_3Fe powders, the frequency dependence of the permeability should be measured. The complex permeability and permitivity of a sample can be measured over a broad range of frequencies by using a microstrip transmission-line device loaded with the sample. A rectangular sample is placed on top of the microstrip, perpendicular to it. A microwave network analyzer is then used to make frequency-swept S-parameter measurements of the loaded microstrip line. The complex permitivity and permeability spectra are then derived from the measured S_{11} and S_{12} scattering parameters.

Further research into the effects of the structural properties of grain boundaries on the macroscopic properties of nanocrystals could lead to more applications of nanocrystalline materials. Currently there is much research and interest in "interface effects" of nanocrystalline materials however, there is little application of nanocrystalline materials exhibiting these effects. My research has shown that the grain boundaries high volume fraction of grain boundaries along with the local atomic structure of the grain boundaries affect the macroscopic vibrational and magnetic properties of nanocrystalline materials. A better understanding of the effects of grain boundary structure could lead to the engineering of nanocrystalline materials for specific applications that exploit their unique vibrational or magnetic properties.

References

1 Y. N. C. Chan, G. S. W. Craig, R. R. Schrock, and R. E. Cohen, Chemical Materials **4,** 885 (1992).

2 S. I. Stupp, S. Son, H. C. Lin, and L. S. Li, Science **259,** 59 (1993).

3 Y. Yoshizawa, S. Oguma, and K. Yamauchi, Journal of Applied Physics **64,** 6044 (1988).

4 G. Herzer, IEEE Transactions on Magnetics **26,** 1397 (1990).

5 S. Farad, R. Leon, D. Leonard, and J. L. Merz, Physical Review B **52,** 5752 (1995).

6 S. Schuppler, S. L. Friedman, M. A. Marcus, D. L. Adler, Y. H. Yie, F. M. Ross, T. D. Harris, W. L. Brown, Y. J. Chabal, and et al., Physical Review Letters **72,** 2648 (1994).

7 J. Eastman and R. W. Siegel, Research and Development, January 1989, 57.

8 T. Haubold, T. Birringer, B. Lengeler, and H. Cleiter, Physics Letters A **135,** 461 (1989).

9 G. J. Thomas, R. W. Siegel, and J. A. Eastman, Scripta Metallurgica et Materialia **24,** 201 (1990).

10 E. A. Stern, R. W. Siegel, M. Newville, P. G. Sanders, and D. Haskel, Physical Review Letters **75,** 3874 (1995).

11 H. Gleiter, *Progress in Materials Science*, Vol. 33 (1989).

12 R. W. Siegel, Physics Today **46,** 64 (1993).

13 H. J. Fecht, Physical Review Letters **65,** 610 (1990).

14 M. Wagner, Acta Metallurgica et Materialia **40,** 957 (1992).

15 Y. R. Abe, J. C. Holzer, and W. L. Johnson, *Structure and Properties of Interfaces in Materials* (Materials Research Society, Pittsburgh, 1992).

16 J. Weissmüller, Journal of Materials Research **9,** 4 (1994).

17 Z. Q. Gao and B. Fultz, Nanostructured Materials **4,** 939 (1994).

18 C. Bansal, Z. Q. Gao, and B. Fultz, Nanostructured Materials **5,** 327 (1995).

19 C. D. Terwilliger and Y.-M. Chiang, Acta Metallurgica et Materialia **43** (1995).

20 C. E. Krill, H. Ehrhardt, and R. Birringer, *Chemistry and Physics of Nanostructures and Related Non-Equilibrium Materials* (TMS, Warrendale, PA, 1997).

21 A. Tschöpe and R. Birringer, Acta Metallurgica et Materialia **41,** 2791 (1993).

22 G. V. Eynatten, J. Horst, K. Dransfeld, and H. E. Bömmel, Hyperfine Interactions **29,** 1311 (1986).

23 H. Kuwano, H. Ouyang, and B. Fultz, Nanostructured Materials **1,** 143 (1992).

24 H. A. Eastman and M. R. Fitzsimmons, Journal of Applied Physics **77,** 522 (1995).

25 M. Hayashi, E. Gerkema, E. M. v. d. Kraan, and I. Tamura, Physical Review B **42,** 9771 (1990).

26 L. B. Hong, C. C. Ahn, and B. Fultz, Journal of Materials Research **10,** 2408 (1995).

27 K. Suzuki and K. Sumiyama, Materials Transactions JIM **36,** 188 (1995).

28 B. Fultz, L. Anthony, L. J. Nagel, R. M. Nicklow, and S. Spooner, Physical Review B **52,** 3315 (1995).

29 J. Trampenau, K. Bauszuz, W. Petry, and U. Herr, Nanostructured Materials **6,** 551 (1995).

30 B. Fultz, J. L. Robertson, T. A. Stephens, L. J. Nagel, and S. Spooner, Journal of Applied Physics **79,** 8318 (1996).

31 H. N. Frase, L. J. Nagel, J. L. Robertson, and B. Fultz, Philosophical Magazine B **75,** 335 (1997).

32 R. Alben, J. J. Becker, and M. C. Chi, Journal of Applied Physics **49,** 1653 (1978).

33 C.-W. Chen, *Magnetism and Metallurgy of Soft Magnetic Materials* (Dover, New York, 1986).

34 H. P. Klug and L. E. Alexander, *X-Ray Diffraction Procedures* (Wiley-Interscience, New York, 1974).

35 J. Eckert, J. C. Holzer, C. E. Krill III, and W. L. Johnson, Journal of Materials Research **7,** 1751 (1992).

36 J. Eckert, J. C. Holzer, C. E. Krill III, and W. L. Johnson, Journal of Applied Physics **73,** 2794 (1993).

37 E. D. Hallman and B. Brockhouse, Canadian Journal of Physics **47,** 1117 (1969).

38 G. Venkataraman, L. A. Feldkamp, and V. C. Sahni, *Dynamics of Perfect Crystals* (MIT Press, Cambridge, 1975).

39 G. Kostorz and S. W. Lowesey, *Treatise on Materials Science and Technology, Vol. 15, Neutron Scattering* (Academic, New York, 1979).

40 V. F. Sears, Physical Review A **7,** 340 (1973).

41 G. L. Squires, *Introduction to the Theory of Thermal Neutron Scattering* (Cambridge University Press, Cambridge, 1979).

42 V. F. Sears, E. C. Svensson, and B. M. Powell, Canadian Journal of Physics **73,** 726 (1995).

43 B. Fultz, C. C. Ahn, E. E. Alp, W. Sturhahn, and T. S. Toellner, Physical Review Letters **79,** 937 (1997).

44 A. Tamura, K. Higeta, and T. Ichinokawa, Journal of Physics C **15,** 1585 (1983).

45 A. Tamura, K. Higeta, and T. Ichinokawa, Journal of Physics C **16,** 4975 (1983).

46 A. Tamura and T. Ichinokawa, Journal of Physics C **16** (1983).

47 M. F. Thorpe, Journal of Non-Crystalline Solids **57,** 355 (1983).

48 T. Pang, Physical Review B **45,** 2490 (1992).

49 M. I. Klinger, Physics Letters A **170,** 222 (1992).

50 D. Caprion, P. Jund, and R. Jullien, Physical Review Letters **77,** 675 (1996).

51 A. P. French, *Vibrations and Waves* (Norton, New York, 1971).

52 D. Wolf, J. Wang, S. R. Phillpot, and H. Gleiter, Physical Review Letters **74,** 4686 (1995).

53 G. L. Caër and J. M. Dubois, Journal of Physics E: Scientific Instruments **12,** 1083 (1979).

54 S. H. Bell, M. P. Weir, D. R. E. Dickson, J. F. Gibson, G. A. Sharp, and T. J. Peters, Biochimica et Biophysica Acta **787,** 227 (1984).

55 B. Fultz, H. Kuwano, and H. Ouyang, Journal of Applied Physics **77,** 3458 (1995).

56 J. Y. Ping, D. G. Rancourt, and R. A. Dunlap, Journal of Magnetism and Magnetic Materials **103,** 285 (1992).

57 R. M. Bozorth, *Ferromagnetism* (D. Van Nostrand Company, Inc., New York, 1951).

58 B. D. Cullity, *Introduction to Magnetic Materials* (Addison-Wesley Publishiing Company, Reading, Massachusetts, 1972).

59 H. A. Bethe and J. Schwinger, N.R.D.C. Report D1-117, Cornell University **March** (1943).

60 R. A. Waldron, Institution of Electrical Engineers **373,** 272 (1960).

61 J. P. Kinzer and I. G. Wilson, Bell Systems Technology Journal **26,** 410 (1947).

62 R. A. Waldron, *Theory of Guided Electromagnetic Waves* (Van Nostrand Reinhold Company, London, 1970).

63 P. G. Sanders, C. J. Youngdahl, and J. R. Weertman, Materials Science and Engineering A **234,** 77 (1997).

64 E. Scheil, Z. Metallk. **27,** 199 (1935).

65 H. E. Schaefer, R. Würschum, R. Birringer, and H. Gleiter, Journal of Less-Common Metals **140,** 161 (1988).

66 H. J. Fecht, E. Hellstern, Z. Fu, and W. L. Johnson, Metallurgical Transactions A **21,** 2333 (1990).

Appendix

Tables of Values

Sample	crystal size (nm) (Section 2.2)	RMS strain (%) (Section 2.2)	Volume Fraction Fe Impurity	Low Energy Inelastic Scattering Slope (meV^2) (Section 3.4.1)
20:1 as-milled	6	0.01	0.04	110
5:1 as-milled	12	0.45	0.05	70
5:1 265°C annealed	16	0.31	0.02	60
5:1 425°C annealed	27	0.26	0	50
5:1 600°C annealed	~100	0.06	0	40
2:1 as-milled	15	0.78	0.05	
2:1 265°C annealed	20	0.45	0.04	
2:1 600°C annealed	~100	~0	0	

Table A.1. Reference table of values discussed in thesis.

Sample	Grain Boundary Volume Fraction (Mössbaer)	Grain Boundary Volume Fraction $V_f = \frac{3dr}{2R}$	$\mu_{grain\ boundary}$ (μ_B) (Mössbauer)	$\mu_{grain\ boundary}$ (μ_B) (SANS)
20:1 as-milled	0.28	0.25	0.6	
5:1 as-milled				
5:1 265°C annealed				
5:1 425°C annealed				
5:1 600°C annealed				
2:1 as-milled	0.08	0.1	0.6	0.7
2:1 265°C annealed	0.08	0.08	0.8	0.9
2:1 600°C annealed				

Table A.2. Reference table of values discussed in thesis.

Sample	Resistivity (Ω cm) x10^4	μ_{max} (M-H curve)	H_C (M-H curve)	M_S (M-H curve)	μ' (Cavity)	μ'' (Cavity)
20:1 as-milled	11.29	96	29	920	43	7
5:1 as-milled	6.44	68	20	810	15	89
5:1 265°C annealed	4.81	62	20	820	12	10
5:1 425°C annealed	2.14	51	14	850		
5:1 600°C annealed	1.73	70	22	890	11	11
2:1 as-milled						
2:1 265°C annealed						
2:1 600°C annealed						

Table A.3. Reference table of values discussed in thesis.